



THE UNIVERSITY *of* EDINBURGH

This thesis has been submitted in fulfilment of the requirements for a postgraduate degree (e.g. PhD, MPhil, DClinPsychol) at the University of Edinburgh. Please note the following terms and conditions of use:

This work is protected by copyright and other intellectual property rights, which are retained by the thesis author, unless otherwise stated.

A copy can be downloaded for personal non-commercial research or study, without prior permission or charge.

This thesis cannot be reproduced or quoted extensively from without first obtaining permission in writing from the author.

The content must not be changed in any way or sold commercially in any format or medium without the formal permission of the author.

When referring to this work, full bibliographic details including the author, title, awarding institution and date of the thesis must be given.

Wearable Devices for Microwave Head Diagnostic Systems



Mohd Saiful Riza Bashri

A thesis submitted for the
Degree of Doctor of Philosophy
The University of Edinburgh
2018

DECLARATION OF ORIGINALITY

I hereby declare that this thesis has been composed by myself and that except where stated, the work contained is my own. I also declare that the work contained in this thesis has not been submitted for any other degree or professional qualification except as specified.

Mohd Saiful Riza Bashri

March 2018

Edinburgh, UK

ACKNOWLEDGEMENTS

I would like to express my greatest gratitude to my supervisor, Prof. Tughrul Arslan for his invaluable support, guidance and expertise throughout this study.

To the members of the E-wireless research Group (E-wireless), I owe sincere and earnest thankfulness for the unforgettable and unique experience of my life.

I would like to acknowledge my sponsors, International Islamic University Malaysia (IIUM) and Ministry of Higher Education Malaysia (MoHE), for funding my studies.

I am extremely grateful to my family, my wife, Amalina and my daughter, Salsabila for their understanding, patience and support during the study and preparation of this thesis.

ABSTRACT

Although current head imaging technologies such as magnetic resonance imaging (MRI) and computed tomography (CT) are capable of providing accurate diagnosis of brain injuries such as stroke and brain tumour, they have several limitations including high cost, long scanning time, bulky and mostly stationary. On the other hand, radar-based microwave imaging technology can offer a low cost, non-invasive and non-ionisation method to complement these existing imaging techniques. Moreover, a compact and wearable device for microwave head imaging is required to facilitate frequent or real-time monitoring of a patient by providing more comfort to the patient. Therefore, a wearable head imaging device would be a significant advantage compared to the existing wideband microwave head sensing devices which typically utilise rigid antenna structure. Furthermore, the wearable device can be integrated into different microwave imaging setups such as real-time wearable head imaging systems, portable systems and conventional stationary imaging tools for use in hospitals and clinics. This thesis presents the design and development of wearable devices utilising flexible antenna arrays and compact radio frequency (RF) switching circuits for wideband microwave head imaging applications.

The design and characterisation of sensing antennas using flexible materials for the wearable head imaging device are presented in the first stage of this study. There are two main variations of monopole antennas that have been developed in this research, namely trapezoidal and elliptical configurations. The antennas have been fabricated using different flexible substrate materials such as flexible FR-4, polyethylene terephthalate (PET) and textile. Wideband performances of the antennas have been achieved by optimising their co-planar waveguide feeding line structures. Importantly, the efficiencies of the fabricated antennas have been tested using a realistic human head phantom by evaluating their impedance matching performances when operating in close proximity to the head phantom.

The second stage of the study presents the development of wearable antenna arrays using the proposed flexible antennas. The first prototype has been built using an array of 12 flexible antennas and a conformal absorbing material backed with a

conductive sheet to suppress the back lobe radiation of the monopole antennas. Additionally, the absorber also acts as a mounting base to hold the antennas where the wearable device can be comfortably worn like a hat during the measurement and monitoring processes. The effect of mutual coupling between adjacent antennas in the array has been investigated and optimised. However, the use of the absorbing material makes the device slightly rigid where it can only be fitted on a specific head size. Thus, a second prototype has been developed by using a head band to realise a stretchable configuration that can be mounted on different sizes of human heads. Furthermore, due to the stretchable characteristic of the prototype, the antennas can be firmly held in their positions when measurements are made. In addition, fully textile based sensing antennas are employed in this prototype making it perfectly suitable for monitoring purposes.

Low cost and compact switching circuits to provide switching mechanism for the wearable antenna array are presented in the third stage of this study. The switching circuit is integrated with the antenna array to form a novel wearable microwave head imaging device eliminating the use of external bulky switching network. The switching circuit has been built using off-the-shelf components where it can be controlled wirelessly over Bluetooth connection. Then, a new integrated switching circuit prototype has been fabricated using 6-layer printed circuit board (PCB) technology. For the purpose of impedance matching for the radio-frequency (RF) routing lines on the circuit, a wideband Microstrip-to-Microstrip transition is utilised.

The final stage of this study investigates the efficacy and sensitivity of the proposed wearable devices by performing experiments on developed realistic human head phantoms. Initially, a human head phantom has been fabricated using food-based ingredients such as tap water, sugar, salt, and agar. Subsequently, lamb's brains have been used to improve the head phantom employed in the experiments to better mimic the heterogeneous human brain. In terms of imaging process, an interpolation technique developed using experimental data has been proposed to assist the localisation of a haemorrhage stroke location using the confocal delay-and-sum algorithm. This new technique is able to provide sensible accuracy of the location of the blood clot inside the brain.

The wearable antenna arrays using flexible antennas and their integrations with compact and low cost switching circuits reported in this thesis make valuable contribution to microwave head imaging field. It is expected that a low-cost, compact and wearable radar-based microwave head imaging can be fully realised in the future for wide range of applications including static scanning setup in hospitals, portable equipment in ambulances and as a standalone wearable head monitoring system for remote and real-time monitoring purposes.

TABLE OF CONTENTS

DECLARATION OF ORIGINALITY	II
ACKNOWLEDGEMENTS.....	III
ABSTRACT	VI
LIST OF FIGURES	XI
LIST OF TABLES	XIX
LIST OF ACRONYMS AND ABBREVIATIONS	XX
CHAPTER 1: INTRODUCTION.....	1
1.1 Research Motivation.....	1
1.2 Research Investigations	4
1.2.1 Design Challenges	5
1.2.1.1 Antenna Design.....	5
1.2.1.2 Compact RF Switching Circuit.....	5
1.2.1.3 Performance Evaluation of the Developed Prototype on Realistic Head Phantom	6
1.2.1.4 Development of the Imaging Algorithm based on Confocal Delay-and-Sum Technique	6
1.2.2 Research Objectives	7
1.3 Original Contributions of the Thesis	7
1.4 Overview of the Thesis.....	8
1.5 Publications Arising from This Research.....	10
CHAPTER 2: OVERVIEW OF MICROWAVE SYSTEMS FOR BIOMEDICAL IMAGING APPLICATIONS.....	12
2.1 Microwave Breast Imaging Systems	12
2.2 Microwave Head Imaging and Sensing System.....	18
2.2.1 Microwave Head Tomography System	19
2.2.2 Microwave Head Sensing System	22
2.2.3 Wideband Radar-based System.....	24
2.3 Overview of Proposed Wearable Microwave Head Imaging/ Sensing for Stroke Detection.....	28
2.4 Summary	31
CHAPTER 3: FLEXIBLE ANTENNA DESIGN FOR WEARABLE MICROWAVE HEAD IMAGING DEVICE	32
3.1 Requirement of a Wearable Antenna for Head Imaging Systems.....	32
3.2 Development of Wideband Planar Monopole Antenna Design using Flexible Substrates	36
3.2.1 Introduction	36
3.2.2 Antenna Design Procedure	37
3.2.2.1 Inverted Trapezoidal Monopole Antenna on FR-4 substrate.....	39

3.2.2.1.1	Simulated Radiation Pattern of the Trapezoidal Monopole Antenna	44
3.2.2.1.2	Time-domain Characterisation of the Trapezoidal shaped Monopole Antenna.....	46
3.2.2.2	Inverted Trapezoidal Shaped Monopole Antenna on PET substrate	48
3.2.2.3	Elliptical Shaped Monopole Antenna using Textile Materials	50
3.2.2.3.1	Simulated Radiation Pattern of the Elliptical shaped Monopole Antenna.....	54
3.2.2.3.2	Time-domain Characterisation of the Elliptical shaped Monopole Antenna.....	54
3.2.3	Performance Evaluation of the proposed Antennas in-close Proximity to a Human Head Phantom.....	56
3.2.3.1	Inverted Trapezoidal shaped Monopole Antenna.....	57
3.2.3.2	Elliptical shaped Monopole Antenna.....	61
3.2.4	Fabrication and Measurement results	62
3.2.4.1	Trapezoidal shaped Monopole Antenna on 0.2mm thick FR-4 substrate.....	63
3.2.4.2	Trapezoidal Monopole Antenna on PET Substrate	64
3.2.4.3	Elliptical Monopole Antenna on Felt Substrate using Conductive Textile.....	65
3.3	Summary	66
CHAPTER 4: WEARABLE PROTOTYPES FOR MICROWAVE HEAD IMAGING.....		68
4.1	Antenna Array with Flexible Metal Backed Lossy Dielectric Absorber	69
4.1.1	Development of 12 Elements Antenna Array on Conductive Sheet backed Flexible Absorber.....	75
4.1.2	Reflection Coefficients of the PET-based Trapezoidal Monopole Antenna Array with Conductive Sheet backed Flexible Dielectric Absorber	77
4.1.3	Mutual-Coupling between Adjacent Antennas for Trapezoidal Shaped Monopole Antenna on PET Substrate.....	79
4.2	Head Strap Antenna Array using 12 Antenna Elements	80
4.2.1	Reflection Coefficients of the Textile-based Elliptical Monopole Antenna Array	81
4.2.2	Investigation on the Mutual-coupling between Adjacent Antennas for Elliptical Monopole Antenna Array	82
4.3	Specific Absorption Rate and Maximum Allowed Transmitted Power	83
4.4	Summary	86
CHAPTER 5: NOVEL COMPACT RF SWITCH CIRCUIT FOR WEARABLE HEAD IMAGING SYSTEMS.....		88
5.1	Introduction	88

5.2	Descriptions of the Main Components of the proposed Compact RF Switch Circuit.....	90
5.2.1	Micro-controller Atmega328P	90
5.2.2	GaAs MMIC SP4T Non-Reflective Switch	91
5.2.3	GaAs MMIC SP8T Non-Reflective Switch	92
5.2.4	USB to UART Interface FT232RL	93
5.2.5	Bluetooth Module for Wireless Control	93
5.3	Characterisations of the RF Switches on Evaluation Boards using Vector Network Analyser	94
5.4	Development and Implementation of the RF Switching Circuit	97
5.4.1	RF Switching Configuration	97
5.4.1.1	Mono-static Switching Configuration	97
5.4.1.2	Multi-static Switching Configuration	98
5.4.2	PCB implementation of the RF Switching Circuit	99
5.4.2.1	Circuit Diagram	99
5.4.2.2	Evaluation of the circuit via Breadboard Testing	100
5.4.2.3	Fabrication of the design on PCB	102
5.4.2.3.1	Optimisation of the Microstrip RF Transmission Lines on 6 layer PCB Board	103
5.4.2.4	Evaluation of the PCB Design	107
5.5	Summary	110
CHAPTER 6: EXPERIMENTAL MEASUREMENT ON ARTIFICIAL HEAD PHANTOMS.....		112
6.1	Introduction	112
6.2	Investigation on the Sensitivity and the Detection Capability of the Proposed Antenna	113
6.3	Measurement Setup for the Wearable Prototype Testing.....	120
6.3.1	Realistically Shaped Human Head Phantom using Low Cost Materials	121
6.3.2	Artificial Human Head Phantom using Lamb's Brains.....	123
6.4	Measurements Results and Analysis	125
6.4.1	Reflection Coefficient Measurements	125
6.4.2	Transmission Coefficient Measurements	128
6.5	Summary	131
CHAPTER 7: MICROWAVE IMAGING RESULTS FOR STROKE DETECTION.....		132
7.1	Introduction	132
7.2	Confocal Delay and Sum (CDAS) Imaging Algorithm	133
7.3	Differential Signals Method	134
7.4	Image Reconstruction of a Head Phantom with Haemorrhagic Stroke in Simulation Environment	135

7.5	Image Reconstruction of Head Phantom with Haemorrhagic Stroke using Measurement Results	139
7.6	Summary	146
CHAPTER 8: CONCLUSION AND FUTURE WORK		147
8.1	Chapter Summary and Conclusion.....	147
8.2	Summary of Contributions	151
8.2.1	Compact and Flexible Antenna Design.....	151
8.2.2	Prototypes of Wearable Antenna Array	151
8.2.3	Low cost and Compact RF Switching Circuit for Microwave Head Imaging	152
8.2.4	Performance verification of the wearable prototypes on a realistic head phantom	152
8.2.5	Development of a Modified Confocal Algorithm using Experimental Data.....	153
8.3	Suggestions for Future Work	153
8.3.1	Antenna Design	153
8.3.2	Antenna Array	154
8.3.3	RF Switching System	154
8.3.4	Imaging and Sensing Algorithms	155
8.4	Final Comments	155
REFERENCE		156

LIST OF FIGURES

Figure 1.1: Conventional medical imaging method.....	1
Figure 2.1: FDTD time-domain waveforms after time-shifting and summing of backscattered responses [1].....	13
Figure 2.2: Tumour location inside the breast is indicated by the maximum peak [2].....	14
Figure 2.3: Experimental setup for initial verification of confocal imaging for breast cancer detection [3].....	15
Figure 2.4: Image of the 1.2 diameter wood dowel mimicking tumour inside a PVC pipe [3].....	15
Figure 2.5: Prototype of the antenna array system for early breast cancer detection using time-domain approach [4].....	16
Figure 2.6: Reconstructed image of a realistic breast with tumour indicating the estimate location of the cancer [4].....	16
Figure 2.7: MARIA4/5 and the bed system developed by University of Bristol [5]..	17
Figure 2.8: 3-D image of a breast produced by MARIA from a clinical trial [5].....	18
Figure 2.9: Simulated 2-D head model inside the MWT imaging chamber [6].....	19
Figure 2.10: Reconstructed MWT image using multi-frequency at 0.5GHz and 1GHz [6].....	20
Figure 2.11: EMTensor Brain Imaging System Generation 1 [7].....	21
Figure 2.12: Images of a patient's head with stroke probe at 0.95GHz. (a) MRI image and (b) EMT image [8].....	22
Figure 2.13: (a) First prototype with 10 patch antennas and (b) second prototype with 12 patch antennas [9].....	23
Figure 2.14: The Strokefinder MD100 by Medfield Diagnostics AB [115].....	24
Figure 2.15: 2-D view of the simulated head model for stroke detection [10].....	25
Figure 2.16: Reconstructed image of the head model using DAS-CF imaging algorithm [10].....	25
Figure 2.17: Radar-based microwave head imaging system [11].....	26
Figure 2.18: Resulting images of two different locations of a haemorrhagic stroke [11].....	27

Figure 2.19: Microwave head imaging system for on-site rapid diagnosis of intracranial hematoma [12].....	28
Figure 2.20: Pulmonary edema monitoring sensor with body area network [13].....	29
Figure 2.21: Wearable Sensing and Detection Applicator for Head Diagnostics.....	30
Figure 2.22 Overview of stroke detection Body Area Network (BAN) system.....	31
Figure 3.1: Vivaldi antenna in its basic form [14].....	33
Figure 3.2: 3-D compact folded dipole antenna for microwave head imaging [15]...	34
Figure 3.3: 16 flexible antenna array for breast cancer detection [16].....	35
Figure 3.4: Wideband textile antenna for microwave medical imaging [17].....	36
Figure 3.5: Various shapes of planar monopole antenna [18].....	37
Figure 3.6: Head phantom model with the proposed monopole antennas.....	38
Figure 3.7: Co-planar waveguide structure.....	40
Figure 3.8: Initial design of inverted trapezoidal monopole antenna.....	41
Figure 3.9: Simulated reflection coefficient for inverted triangular antenna shown in Figure 3.8.....	41
Figure 3.10: Optimisation process of the impedance bandwidth of the antenna by varying parameter g_l . (a) $g_l = 24\text{mm}$ (b) $g_l = 34\text{mm}$ (c) $g_l = 44\text{mm}$ and (d) $g_l = 54\text{mm}$	42
Figure 3.11: Reflection coefficients for parameter sweep for g_l from 24mm to 54mm.....	42
Figure 3.12: Geometry of the proposed UWB antenna (a) Top view (b) Bottom view.....	43
Figure 3.13: Induced current on the antenna at (a) 1.5 GHz, (b) 2.5 GHz and (c) 3.0 GHz.....	44
Figure 3.14: Simulated E-(XZ) and H-(XY) plane 2-D far-field radiation patterns at 1.5GHz.....	45
Figure 3.15: Simulated 3-D radiation patterns of the antenna at (a) 1.5GHz (b) 2GHz (c) 2.5GHz and (d) 3GHz.....	46
Figure 3.16: Simulated gain at the boresight direction ($\theta = 0^\circ$, $\phi = 0^\circ$).....	46
Figure 3.17: Simulated received near-field time-domain pulses radiated by the antenna at different angles without head phantom in H-plane.....	47

Figure 3.18: Simulated reflection coefficient of the trapezoidal monopole antenna on PET substrate.....	49
Figure 3.19: Simulated E-(XZ) and H-(XY) plane 2-D far-field radiation patterns at 1.5GHz for the trapezoidal monopole antenna on PET substrate.....	49
Figure 3.20: Initial design of elliptical monopole antenna.....	50
Figure 3.21: Simulated reflection coefficient of elliptical monopole antenna.....	51
Figure 3.22: Optimisation process of the impedance bandwidth of the antenna by varying parameter g_s . (a) $g_s = 15\text{mm}$ (b) $g_s = 25\text{mm}$ (c) $g_s = 35\text{mm}$ and (d) $g_s = 55\text{mm}$	51
Figure 3.23: Reflection coefficients for parameter sweep for g_s from 15mm to 45mm.....	52
Figure 3.24: Geometry of the wideband elliptical monopole antenna (a) Top view (b) Bottom view.....	53
Figure 3.25: Simulated E-(XZ) and H-(XY) plane 2-D far-field radiation patterns at 1.5GHz for the elliptical monopole antenna on felt substrate.....	54
Figure 3.26: Simulated 3-D radiation patterns of the elliptical monopole antenna at (a) 1.5GHz (b) 2GHz (c) 2.5GHz and (d) 3GHz.....	55
Figure 3.27: Simulated gain of the elliptical shaped monopole antenna.....	55
Figure 3.28: Simulated received near-field time-domain pulses radiated by the antenna in different angles without head phantom in H-plane.....	56
Figure 3.29: Antenna placement on the SAM head phantom in the simulation.....	58
Figure 3.30: Simulated reflection coefficient of the trapezoidal monopole antenna on free space and with the presence of head phantom.....	58
Figure 3.31: Placement of the field probe inside the head phantom.....	60
Figure 3.32: Simulated received near-field time-domain pulses radiated by the trapezoidal shaped antenna at 0° (a) without the head phantom and (b) with the head phantom in H-plane.....	60
Figure 3.33: Simulated received near-field time-domain pulses radiated by the elliptical shaped antenna at 0° (a) without head phantom and (b) with the head phantom in H-plane.....	61

Figure 3.34: Fabricated flexible antenna elements (a) Trapezoidal monopole antenna on FR-4 (b) Trapezoidal monopole antenna on PET and (c) Textile based elliptical monopole antenna.....	62
Figure 3.35: Photograph of the single prototype antenna (inset picture) covered with felt material.....	64
Figure 3.36: Reflection coefficients of the trapezoidal monopole antenna on FR-4.....	64
Figure 3.37: Reflection coefficients of trapezoidal monopole antenna on PET substrate.....	65
Figure 3.38: Reflection coefficients of textile elliptical antenna on free space and artificial head phantom.....	66
Figure 4.1: Simulated E-field distribution inside the head phantom at 1.5GHz.....	70
Figure 4.2: Position of the reflector to suppress the back lobe radiation for improved antenna directivity.....	71
Figure 4.3: Refection coefficients of the antenna for various distance separations between the antenna and the reflector.....	72
Figure 4.4: Simulated E-field distribution inside the head with the use of reflector....	72
Figure 4.5: Flexible absorber shaped as a base for the flexible antennas.....	73
Figure 4.6: Prototype of the antenna array for trapezoidal monopole antenna on FR-4 covered with felt on the top and bottom of the antennas.....	74
Figure 4.7: E-field strength of the transmitted Gaussian pulse with the use of flexible absorber without head phantom.....	75
Figure 4.8: Figure 38 E-field strength of the transmitted Gaussian pulse with the use of flexible absorber with head phantom.....	75
Figure 4.9: Simulated power density inside the head phantom for each antenna element in the array. (a) Antenna 1, Antenna 2 and Antenna 3. (b) Antenna 4, Antenna 5 and Antenna 6. (c) Antenna 7, Antenna 8 and Antenna 9. (d) Antenna 10, Antenna 11 and Antenna 12.....	76
Figure 4.10: Prototype of the wearable head imaging device for medical imaging applications.....	77
Figure 4.11: Measured S11 responses for Ant 1 to Ant 6 in the antenna array.....	78
Figure 4.12: Measured S11 responses for Ant 7 to Ant 12 in the antenna array.....	78

Figure 4.13: Mutual coupling between Ant1 and Ant2 in the PET based array.....	79
Figure 4.14: Flexible antennas integrated with a head band strapped on a head phantom.....	80
Figure 4.15: Measured S11 data for Ant 1 to Ant 6 in the textile based antenna array.....	81
Figure 4.16: Measured S11 data for Ant 7 to Ant 12 in the textile based antenna array.....	82
Figure 4.17: Measured mutual coupling between Ant 1 and Ant 2 in the textile based antenna array.....	82
Figure 4.18: The simulated maximum SAR values over the operating frequency of the antenna.....	84
Figure 4.19: Simulated SAR distribution inside an artificial human head at 1.5GHz for (a) 1mW, (b) 10mW and (c) 100mW.....	85
Figure 4.20: Simulated SAR distribution inside an artificial human head at (a) 1.5GHz, (b) 2GHz, (c) 2.5GHz and (d) 3GHz.....	86
Figure 5.1: Diagram of the proposed RF switching system for wearable application.....	88
Figure 5.2: ATmega328AU PIN diagram [19].....	90
Figure 5.3: HMC241ALP3E SP4T non-reflective switch [20].....	91
Figure 5.4: HMC321LP4E SP8T non-reflective switch [21].....	92
Figure 5.5: FT232RL pin configuration [22].....	93
Figure 5.6: HC-06 Bluetooth module [23].....	94
Figure 5.7: Diagram of the measurement setup for the RF switches.....	95
Figure 5.8: Measured insertion loss of single-pole-four-throw (1P4T) RF switch.....	95
Figure 5.9: Measured insertion loss of single-pole-eight-throw (1P8T) RF switch....	96
Figure 5.10: Measured reflection coefficient of the single-pole-four-throw (1P4T) RF switch.....	96
Figure 5.11: Measured reflection coefficient of the single-pole-eight-throw (1P8T) RF switch.....	97
Figure 5.12: Photograph of the first prototype of the switching circuit.....	97
Figure 5.13: Graphical user interface on an android smartphone for the RF switch....	98
Figure 5.14: Schematic of RF switching circuit diagram.....	100

Figure 5.15: TQFP-32 adaptor for Atmega328P-AU.....	101
Figure 5.16: Breadboard to test the control circuit for the switch.....	102
Figure 5.17: 6 layer PCB stack up.....	102
Figure 5.18: Detailed microstrip-to-microstrip line transition structure.....	104
Figure 5.19: One of the RF traces on the PCB simulated in EM solver.....	105
Figure 5.20: Simulated electric field lines at the cross section of the microstrip-to-microstrip transition.....	105
Figure 5.21: Measured reflection coefficient of the single-pole-four-throw (1P4T) RF switch.....	106
Figure 5.22: Measured reflection coefficient of the single-pole-four-throw (1P4T) RF switch.....	106
Figure 5.23: PCB layout of the circuit design (a) Layer 1 (b) Layer 2 (c) Layer 3 (d) Layer 4 (e) Layer 5 and (f) Layer 6.....	107
Figure 5.24: Fabricated PCB design (a) Top view (b) Bottom view.....	107
Figure 5.25: Measurement setup for the PCB design.....	108
Figure 5.26: Measured reflection coefficient of the single-pole-four-throw (1P4T) RF switch.....	108
Figure 5.27: Measured reflection coefficient of the single-pole-eight-throw (1P8T) RF switch.....	109
Figure 5.28: Measured insertion loss of single-pole-four-throw (1P4T) RF switch.....	109
Figure 5.29: Measured insertion loss of single-pole-eight-throw (1P8T) RF switch.....	110
Figure 6.1: Dielectric measurement setup.....	114
Figure 6.2: Calibration standard for the dielectric probe (a) air (b) shorting probe (c) water.....	114
Figure 6.3: Relative permittivity of the fabricated phantom.....	114
Figure 6.4: Conductivity of the fabricated phantom.....	115
Figure 6.5: Measurement setup for antenna sensitivity test.....	116
Figure 6.6: Artificial stroke targets with various size.....	117
Figure 6.7: Variation of S11 magnitude for different target size.....	118

Figure 6.8: Variation of S11 magnitudes by varying the distance of the blood clot (25mm × 25mm × 25mm) from the antenna.....	119
Figure 6.9: Prototype with a dielectric absorber with switching circuit.....	120
Figure 6.10: Strap based prototype without the use of an absorber.....	120
Figure 6.11: Measurement setup for stroke detection using artificial head phantom.....	121
Figure 6.12: Fabricated artificial head phantom.....	122
Figure 6.13: Measurement the electrical properties of lamb brain.....	123
Figure 6.14: Measured dielectric constant of lamb brain.....	124
Figure 6.15: Measured conductivity of lamb brain.....	124
Figure 6.16: Artificial head phantom filled with lamb brain.....	125
Figure 6.17: Location of the antennas and the switching system (top view).....	126
Figure 6.18: Location of the blood clot inside the head phantom.....	126
Figure 6.19: Measured reflection coefficient of the antennas with the presence of healthy head phantom.....	127
Figure 6.20: Measured reflection coefficient of the antennas with the presence of unhealthy head phantom.....	127
Figure 6.21: Measured reflection coefficient of the antennas with healthy and unhealthy head (a) Ant1 (b) Ant2 (c) Ant3.....	128
Figure 6.22: Measured transmission coefficients between antenna 2 and the receiving antennas for healthy head phantom.....	129
Figure 6.23: Measured transmission coefficients between antenna 2 and the receiving antennas for unhealthy head phantom.....	130
Figure 6.24: Measured transmission coefficients of the antennas with healthy and unhealthy head for antenna 2-antenna 1 and antenna 2-antenna 3.....	130
Figure 7.1: Imaging domain of the cross sectional of the head.....	133
Figure 7.2: Placement of antenna array on the artificial head phantom in the simulation.....	135
Figure 7.3: Time domain response for Ant1. (a) Reflection from the stroke (b) Close up signal.....	136

Figure 7.4: (a) Location of the stroke inside the head phantom, (b) reconstructed image of the head model with a blood clot indicated by the dashed black rectangle shape.....	137
Figure 7.5: Time domain response for Ant3. (a) Reflection from the stroke (b) Close up signal.....	138
Figure 7.6: Reconstructed image of the head model with a blood clot indicated by the dashed black rectangle shape.....	139
Figure 7.7: Simulated reflection coefficient of the antenna for various stroke depths.....	140
Figure 7.8: Average reflection magnitude over stroke depth.....	140
Figure 7.9: Imaging process using measured S_{11} data.....	141
Figure 7.10: The reconstructed image using the first prototype on an artificial head phantom. (a) Healthy head and (b) Head with a stroke (indicated by the black circle).....	142
Figure 7.11: Imaging results for (a) stroke location 1, (b) stroke location 2 and (c) healthy brain scenario using the strap based prototype on lamb brain phantom.....	143
Figure 7.12: Imaging results for (a) trapezoidal monopole antenna prototype, (b) textile based prototype and (c) on lamb brain phantom.....	143

LIST OF TABLES

Table 3.1: GEOMETRIC PARAMETERS OF THE TRAPEZOIDAL ANTENNA ON FR-4 SUBSTRATE.....	44
Table 3.2: FIDELITY FACTORS OF THE TRAPEZOIDAL ANTENNA.....	47
Table 3.3: GEOMETRIC PARAMETERS OF THE TRAPEZOIDAL ANTENNA ON PET SUBSTRATE.....	48
Table 3.4: GEOMETRIC PARAMETERS OF THE ELLIPTICAL MONOPOLE ANTENNA.....	53
Table 3.5: FIDELITY FACTORS OF THE ELLIPTICAL MONOPOLE ANTENNA	56
Table 6.1: RECIPES FOR WHITE MATTER AND BLOOD PHANTOMS (VOLUME PERCENT).....	113
Table 7.1: THE PERFORMANCE OF THE HEAD IMAGING SYSTEMS ARE COMPARED IN TERMS OF ITS ADVANTAGES AND LIMITATIONS.....	145

LIST OF ACRONYMS AND ABBREVIATIONS

1P4T	=	One Pole Four Throw
1P8T	=	One Pole Eight Throw
1P12T	=	One Pole Twelve Throw
2-D	=	Two-Dimensional
3-D	=	Three-Dimensional
ADC	=	Analog to Digital Converter
AMC	=	Artificial Magnetic Conductor
BAN	=	Body Area Network
CDAS	=	Confocal Delay-and-Sum
COTS	=	Component of the Shelf
CPW	=	Co-planar Waveguide
CT	=	Computed-Tomography
DAS-CF	=	Delay-and-Sum Coherence Factor
E	=	Electric Field
EM	=	Electromagnetic
EMI	=	Electromagnetic Interference
GaAs	=	Gallium Arsenide
GUI	=	Graphical User Interface
GPR	=	Ground Penetrating Radar
H	=	Magnetic Field
IDFT	=	Inverse Discrete Fourier Transform
IFFT	=	Inverse Fast Fourier Transform
IDE	=	Integrated Development Environment
I/O	=	Input and Output
MMIC	=	Monolithic Microwave Integrated Circuit
MRI	=	Magnetic Resonance Imaging
MWT	=	Microwave Tomography
NHS	=	National Health Service
PCB	=	Printed Circuit Board
PET	=	Polyethylene Terephthalate

PVC	=	Polyvinyl Chloride
QFN	=	Quad Flat No Leads
RF	=	Radio-Frequency
RFID	=	Radio-Frequency Identification
SAM	=	Specific Anthropomorphic Mannequin
SAR	=	Specific Absorption Rate
SoC	=	System on a Chip
SPI	=	Serial Peripheral Interface
SSOP	=	Shrink Small Outline Package
TBI	=	Traumatic Brain Injuries
UART	=	Universal Asynchronous Receiver-Transmitter
VNA	=	Vector Network Analyser
WBAN	=	Wireless Body Area Network

Chapter 1: Introduction

The background and motivation of this research for wearable biomedical imaging applications specifically for stroke detection are presented in this chapter.

1.1 Research Motivation

Medical imaging plays a vital role in helping medical practitioners to provide the right treatment to patients by producing valuable images inside the human body. These images are typically reconstructed using several methods such as X-ray mammography (X-ray), computed tomography (CT) scan, magnetic resonance imaging (MRI), and ultrasound as illustrated in Figure 1.1. All these modalities have their own advantages and disadvantages depending on the types of diseases or injuries. In general, the main aims of medical imaging are to provide accurate, fast, safe, and cost effective imaging tools to patients.

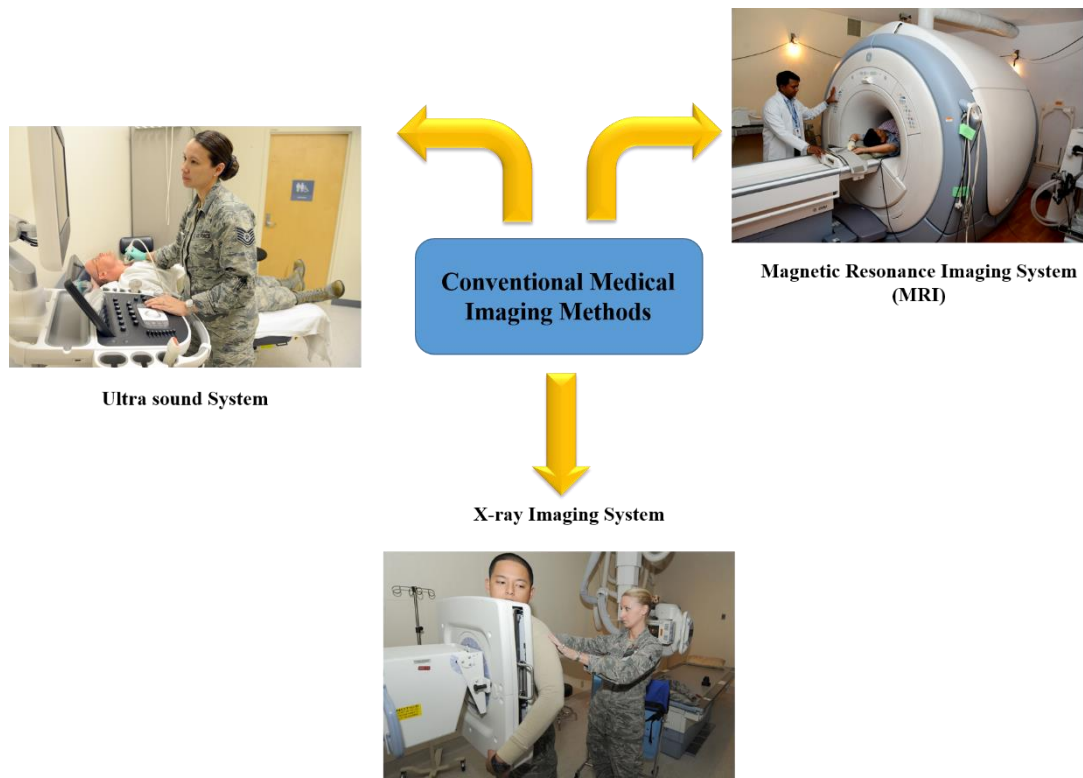


Figure 1.1: Conventional medical imaging methods

Microwave imaging for medical applications is a novel method which has been undergone extensive research by way of computer simulations as well as experimental work. This new method was first introduced back in 1973 to detect lung diseases [24], [25]. Since then, microwave technology for medical applications has been extensively studied and applied to different types of diseases including breast and lung cancers, traumatic brain injuries and stroke [5], [6], [26]–[33]. Microwave medical imaging can be classified into two major groups; microwave tomography and radar-based technique. Microwave tomography aims to reconstruct the actual dielectric profile of a human body while radar-based imaging system operates by transmitting short pulses to detect the main electromagnetic (EM) signal scatterers inside the body. Both techniques rely on the scientific study that shows the malignant tissue (i.e. cancerous tissue) or haemorrhagic stroke (the blood clot formed inside the brain due to ruptured vein) has different dielectric constant value than the surrounding healthy tissues [34], [35]. The scattered waves are then collected and analysed to produce a valuable image which would determine the location of the cancer or the stroke inside the imaged body part.

Based on the statistics released by the National Health Service (NHS), stroke is the fourth most common cause of death in United Kingdom [36]. Stroke can be classified into two categories which are haemorrhagic (blood vessel burst) and ischemic (blood clot within arteries thus preventing oxygen supply to the brain). Both scenarios require different types of treatments which would need an accurate diagnosis as to not endanger the patients' lives. Initial research on stroke detection were done based on tomography method by computer simulations [6], [37], [38]. The reconstruction of the dielectric profile of the human head was done by solving the back projection scattering signals collected by the receiving antenna. The frequency band used was around 700MHz and thus could be classified as narrow-band. The reconstructed dielectric profile of the head was able to show the location of the stroke. However, due to the need to solve the ill-posed inverse scattering equations due to the sparsity of the measured data [39], the calculation would require significant computational resources as well as time-consuming.

A stroke detection system called “Stroke Finder” was initially developed by researchers from Chalmers University using ten microstrip antennas arranged in a helmet [40]. The study was based on the finding that there are differences in the reflection and transmission coefficients between a healthy head and a head with stroke condition [9], [41]. A classifier algorithm that could differentiate the types of stroke had been developed in order to help medical practitioners to provide the right treatment for stroke patients. The system was further improved to make it more practical as a portable device that could be used in an ambulance. The system is currently being tested on several hospitals around the world [30].

Radar-based microwave imaging technique was initially applied for stroke detection in [11], [42]. The main advantage of using radar-based system compared to tomography technique is that it requires less computational power which can reduce the time for the detection process hence paving the way for a fast or even real-time monitoring system. In comparison to microwave tomography system which reconstructs the dielectric profile of the imaged body, the main objective of radar-based technique is to create an image of the main scatterers inside the human body which is normally attributed to the existence of tumour or stroke. In [11], 16 Vivaldi antennas were used to scan a realistic head phantom. The operating frequency range of the antenna is from 1GHz to 4GHz. The selection of the frequency band was made to ensure sufficient penetration depth is achieved to scan the lossy multi-layer human head as well as to provide high resolution image. Subsequently, portable microwave systems using compact directional antennas for traumatic brain injuries (TBI) were proposed in [28], [43]. A compact transceiver was used for the signal generation and acquisition. A successful detection of a bleeding inside a realistic head phantom was reported.

Rapid development in the field of electronics has driven a renovation in the health sectors where a lot of focus have been given to implement a remote health monitoring system [44]. The monitoring devices must be designed to be comfortable, easy to use and low cost. One of the main advantages of wearable devices for medical applications is that they can be comfortably worn and used by patients with intermediate risk at home instead of being hospitalised. To alert medical professionals

in case of emergency, an alerting system that directly connects the patients to rapid response teams can be established over wireless communication [44]. An example of remote monitoring systems in the literature is pulmonary edema monitoring sensor as presented in [13]. The system was proposed to provide real-time monitoring of internal organs for patients that require supervised recovery from a surgical procedure.

In this research, a wearable device utilising flexible antenna array integrated with a compact radio frequency (RF) switching circuit is developed and tested for haemorrhagic stroke detection. Studies on stroke have suggested that early detection of stroke is vital to provide necessary treatments to save lives. Thus, there is a pressing need to provide constant monitoring and frequent checking for patients-at-risk. In addition, all the imaging methods that are currently available, none of them could offer constant monitoring due to their large size and high cost. Since flexible antennas are used as sensors in the proposed microwave imaging system, the concept of wearable device for head imaging specifically for stroke detection is possible for real-time monitoring applications. Furthermore, the proposed wearable interface can also be utilised for monitoring other types of head diseases such as traumatic brain injuries where it can be used by professional personnel involve in high risk environment where probability for an unintentional impact to the head is high.

1.2 Research Investigations

The main challenges of the proposed wearable head device include the design of suitable wideband antennas using several flexible antenna substrates, the development of compact radio frequency switching circuits to realise an integrated wearable head sensing device when combined with flexible antenna arrays, performance evaluation of the wearable prototypes using realistic head phantoms to mimic the occurrence of haemorrhagic stroke and the development of confocal imaging algorithm to create a useful image that can indicate the location of the stroke if exists.

1.2.1 Design Challenges

1.2.1.1 Antenna Design

For radar-based microwave biomedical imaging, a wideband antenna is required in order to adapt a confocal imaging algorithm such as confocal delay-and-sum technique to reconstruct an image of the main scatterers inside the human body. The scattered signals are due to the difference in dielectric constants of the tumours or strokes (blood clots) from their healthy surrounding tissues. To apply the microwave technology for head imaging, a proper antenna design is crucial to ensure that the sensing antenna is able to detect the existence of a blood clot caused by stroke or any other abnormalities inside the brain. The antenna design process is made even more challenging considering that the human head is consisted of several layers of lossy biological tissues in addition to a low dielectric contrast between the blood and the brain.

This research investigates several wideband antenna designs with the aim to operate at the optimal frequency band for microwave head imaging applications. In addition, a novel flexible antenna array configuration for radar-based head imaging is investigated, developed and optimised for wearable applications. The use of flexible antennas instead of typical rigid antennas utilised in the existing wideband microwave head imaging systems provides many advantages such as it can be directly mounted on the head, light weight, low cost and able to provide better comfort to the wearer. Although the area of wearable antennas is well researched, their applications for health monitoring particularly for head imaging are still in its infancy stage and more research has to be done before they can be put for practical use.

1.2.1.2 Compact RF Switching Circuit

To develop a wearable device for head imaging applications, an investigation of using a compact RF switching system where it can be integrated with the proposed flexible antennas is carried out. One of the main challenges to develop a wearable head imaging system is to integrate all the required components such as the antennas and the switching circuit in a compact configuration. As a comparison, the existing microwave head diagnostics in the literature either utilise bulky external switching

systems for array configurations or use rotating platforms with only single antenna in the systems [9], [11], [28], [43]. Although the use of external switching systems is acceptable for their intended application as a portable imaging system, it is not suitable for wearable applications. Moreover, the proposed wearable interface exhibits compact structure which would make the existing microwave head imaging systems become more portable. Therefore, a compact RF switching circuit is proposed where it is integrated with flexible antennas to form a unified wearable device.

1.2.1.3 Performance Evaluation of the Developed Prototype on Realistic Head Phantom

After the prototype of the wearable device is developed, the performance of the device is tested to verify its capability to detect haemorrhagic stroke using realistic head phantoms. To achieve this, a realistic head phantom that resembles real human head with similar electrical properties must be developed. Therefore, a head phantom is initially fabricated using low cost and widely available materials such as tap water, agar, sugar and salt based on a procedure in the literature [29]. The electrical properties of the fabricated phantom are measured to confirm with the data obtained from real human head reported in [45]. Different sizes of artificial blood clots are used to investigate the detection capability of the proposed antennas. Considering that the electromagnetic wave interaction within the human head is different from that of free space, no far-field measurements of the antennas are conducted. Moreover, the wearable system is also tested on another artificial head phantom fabricated using lamb's brains to further validate its performance. The use of actual brain samples in the experiments reflects the heterogeneity of actual human brain where this can give more valuable information regarding the sensing capability of the proposed wearable device.

1.2.1.4 Development of the Imaging Algorithm based on Confocal Delay-and-Sum Technique

Another challenge that needs to be addressed is to transform the measured data from the wearable device to an image that can show the existence of the haemorrhagic stroke inside the brain. This research investigates the adoption of the classical confocal

delay-and-sum (CDAS) technique by using the collected reflected signals from the antennas to create a 2-D image of the cross section of the head phantom in both simulation and experimental works. Since the signals acquisition is carried out in frequency domain in the experiments, an inverse discrete Fourier transform (IDFT) is used to convert the data to the time domain signals. Moreover, a new method based on interpolation technique is proposed to estimate the depth of the stroke according to the measured reflected signals in the confocal algorithm. Finally, the reconstructed image should be able to indicate the location of a stroke inside the brain with sensible accuracy.

1.2.2 Research Objectives

The main objectives of this research are:

1. To investigate the use of a compact and flexible antenna for wearable head imaging applications.
2. To implement and evaluate a compact array of flexible antennas for mono-static radar-based imaging systems.
3. To develop and characterise a compact radio frequency (RF) switching circuit to be integrated with the proposed flexible antenna array.
4. To produce a realistic head phantom to mimic the occurrence of haemorrhagic stroke to test the detection capability of the proposed wearable antennas.
5. To propose and develop an imaging algorithm to detect and locate the haemorrhagic stroke location in order to evaluate the performance of the wearable devices.

1.3 Original Contributions of the Thesis

The research undertaken has contributed to the following key contributions:

1. Compact and flexible wideband antennas for wearable head imaging applications.

2. Wearable prototypes employing the proposed flexible antennas in an array configuration including the use of conductive sheet backed dielectric absorber to suppress the antennas' back lobe radiation.
3. Novel compact RF switching circuits for integration with the antenna array enabling both mono-static and multi-static data acquisitions.
4. Wideband microstrip-to-microstrip transition for 6 layer PCB design.
5. Determination of the smallest artificial blood volume that can be detected by the proposed flexible antenna.
6. Performance verification of the proposed radar-based wearable interface on realistic artificial human heads.
7. An improved confocal imaging algorithm using confocal, delay and sum method assisted by experimental data for estimation of stroke location.

1.4 Overview of the Thesis

The thesis is organised into eight chapters as follows:

Chapter 1 presents the background and motivation to carry out the research. A brief introduction of the microwave technology for biomedical sensing and imaging is provided by comparing several approaches notably microwave sensing using classifier, microwave tomography and radar-based microwave systems.

Chapter 2 presents the literature review on the microwave biomedical sensing and imaging. In this chapter, a comprehensive review on microwave biomedical imaging is given where two of its main applications which are microwave breast cancer detection and microwave head sensing and imaging are thoroughly described. A wearable microwave head imaging concept is presented where the proposed wearable antennas are integrated with a compact RF switching system developed in this thesis will be the key component of the wearable head imaging system.

Chapter 3 discusses the design and development of flexible antennas for wearable microwave head imaging applications. Three different antenna substrates are utilised in the antenna designs which are FR-4, polyethylene terephthalate (PET) and textile materials. Several aspects of the antennas are investigated to verify its

suitability as sensing elements in the wideband wearable head imaging system. Parametric optimisations have been carried out on the antenna structure especially the feeding element of the antennas to improve their impedance bandwidth. Beside the optimisations of the antennas on free-space, extensive computer simulations have been carried out to investigate the performance of the antennas when operating in close proximity to human head to emulate the actual working environment for the antennas.

Chapter 4 proposes a wearable prototype employing 12-flexible antenna array with combination of an absorbing material covered with a flexible conductive sheet. The use of the absorber is to absorb the back lobe radiation of the monopole antennas that exhibit bi-directional pattern to suppress unwanted radiations from the surroundings. In addition, a strap based configuration employing the same number of antennas is also explored. Measurements are made to analyse the reflection coefficients and the mutual coupling performance of the antenna array. In addition, electromagnetic simulations have been carried out for the antenna array to investigate the spatial electrical field distribution inside the human head. This study is to verify that the number of antenna elements used in the array is sufficient to detect the formation of a stroke in the brain.

Chapter 5 discusses the evolution of the proposed compact RF switching system from stacked configuration made from evaluation boards of the RF switches to the final integrated configuration in a single PCB. The initial prototype of the switching system is built using off-the-shelf components where some of the components are on their evaluation boards such as the RF switches. These components are connected together using jumper wires on a small bread board to form a very compact switching device. The performance of the initial prototype is validated in terms of its impedance matching and insertion loss. Next, a new prototype is developed on a single board by using the same components used in the initial design. The impedance matching and the insertion loss of the circuit are measured and analysed. Finally, the compact integrated switch circuit is connected to the proposed flexible array to form a compact wearable interface for microwave stroke detection systems.

Chapter 6 presents the experiments conducted using the proposed wearable interfaces on two realistic head phantoms. Several size of stroke targets are fabricated

to mimic the haemorrhagic stroke. The basic detection capability of the antenna is first conducted by varying the size of the strokes in a simple experiment using liquid based phantom with similar electrical properties to that of human head. In addition, the locations of the stroke are varied in the experiments to verify the performance of the wearable systems. The measured signals are collected and stored in a laptop for post-processing to reconstruct the image of the head phantom.

Chapter 7 describes the development of the radar-based microwave algorithm using confocal algorithm which is confocal delay-and-sum technique. The differential signals method is adapted in this research which also serves as a calibration method for the imaging algorithm. Since the measurements are made in the frequency domain, an inverse Fourier transform (IFT) is applied to the data to convert it to time-domain signals for adaption of the confocal algorithm.

Chapter 8 concludes the research investigations in this thesis. In addition, the contributions of this thesis are re-highlighted and further research based on the developed wearable head imaging devices are suggested.

1.5 Publications Arising from This Research

In the course of this research, the following journals and conference papers have been published and submitted:

Conference papers:

1. **M. S. R. Bashri**, T. Arslan and W. Zhou, "Flexible antenna array for wearable head imaging system," *2017 11th European Conference on Antennas and Propagation (EUCAP)*, Paris, 2017, pp. 172-176.
2. **M. S. R. Bashri**, T. Arslan, W. Zhou and N. Haridas, "Wearable device for microwave head imaging," *2016 46th European Microwave Conference (EuMC)*, London, 2016, pp. 671-674.
3. **M. S. R. Bashri**, T. Arslan, W. Zhou and N. Haridas, "A compact RF switching system for wearable microwave imaging," *2016 Loughborough Antennas & Propagation Conference (LAPC)*, Loughborough, 2016, pp. 1-4.
4. **M. S. R. Bashri**, T. Arslan and W. Zhou, "A dual-band linear phased array antenna for WiFi and LTE mobile applications," *2015 Loughborough Antennas & Propagation Conference (LAPC)*, Loughborough, 2015, pp. 1-5.

Journal papers:

1. **M. S. R. Bashri** and T. Arslan, "Low-cost and compact RF switching system for wearable microwave head microwave head imaging with performance verification on artificial head phantom," *IET Microwaves, Antenna & Propagation*, 2017.
2. **M. S. R. Bashri** and T. Arslan, "Fully textile antenna array for wearable microwave head diagnostic systems," *IEEE Transactions on Antennas and Propagation*. (Journal Submitted, Under Review)

Chapter 2: Overview of Microwave Systems for Biomedical Imaging Applications

In this chapter, a comprehensive review on the use of microwave technology for biomedical applications is presented. Currently, medical imaging systems used in clinics or hospitals are X-ray, magnetic resonance imaging (MRI), ultrasound and positron emission tomography (PET). These techniques have provided medical practitioners with images of internal organs to assist them to diagnose potential diseases a patient could have. The data provided by these methods vary in terms of resolution, operating procedure and implementation cost. In addition, some of them rely on ionising radiation which can have adverse effects on the patient if used frequently.

Microwave technique offers many advantages compared to above methods such as low cost, non-ionising and ease of use. This technique has been applied to detect tumours, stroke, internal bleeding, bone generation, congestive heart failure and tissue healing [5], [11], [25], [27], [31], [46]. The fundamental working principle of the microwave technology is based on the difference of the electrical properties particularly the permittivity and the conductivity between the healthy and unhealthy tissues in the human body. When illuminated with electromagnetic (EM) wave, these tissues will scatter the signal differently where the collected reflected signal can be used to diagnose any potential diseases inside the human body. Two main applications of microwave medical imaging systems are presented which are microwave breast cancer detection and microwave head imaging or sensing systems.

2.1 Microwave Breast Imaging Systems

A brief review on the research carried out on breast imaging over the past 20 years is first presented. This is due to the fact that most of the pioneering studies using wideband microwave techniques for biomedical applications were implemented on detecting a tumour inside the breast. Moreover, the fundamental principle of detecting

breast cancers due to dielectric contrast between the healthy breast and cancerous tissues is also being applied to the head imaging where there exists detectable dielectric contrast between the blood and brain tissues in the case of haemorrhagic stroke or other head diseases such as subdural hematoma and brain tumour.

Initial feasibility studies on detecting tumour inside the breast were done in the simulation environment [1], [47]. A short pulse was used to illuminate a breast model embedded with a small tumour. Based on the acquired scattering signals in the time domain, a confocal imaging technique called delay and sum method adopted from ground penetrating radar (GPR) technology was applied to detect the location of the tumour. The simulation results show that there was detectable tumour response based on the computed time domain waveforms as shown in Figure 2.1. In this study, the

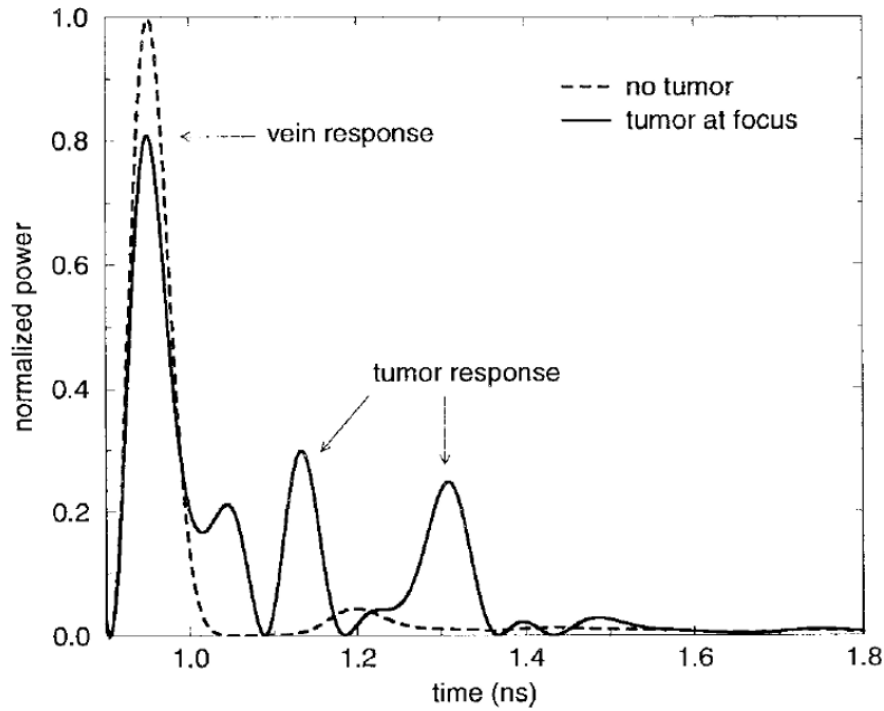


Figure 2.1: FDTD time-domain waveforms after time-shifting and summing of backscattered responses [1]

permittivity of the breast tissue and the tumour at 6GHz were assumed to be 9 and 50 respectively. The values for the tissues were taken from the measurements carried out on actual human tissues as reported in [48]. For the conductivity, the values used in the simulation were 0.4S/m and 7S/m. Another numerical study has been reported in

[2] by applying the ultra-wideband radar technique and confocal imaging to provide a preliminary numerical evaluation of the breast cancer detection. The main aim of the research was to develop a numerical model that is more amenable to practical experiments. Figure 2.2 demonstrates the effectiveness of the tumour detection

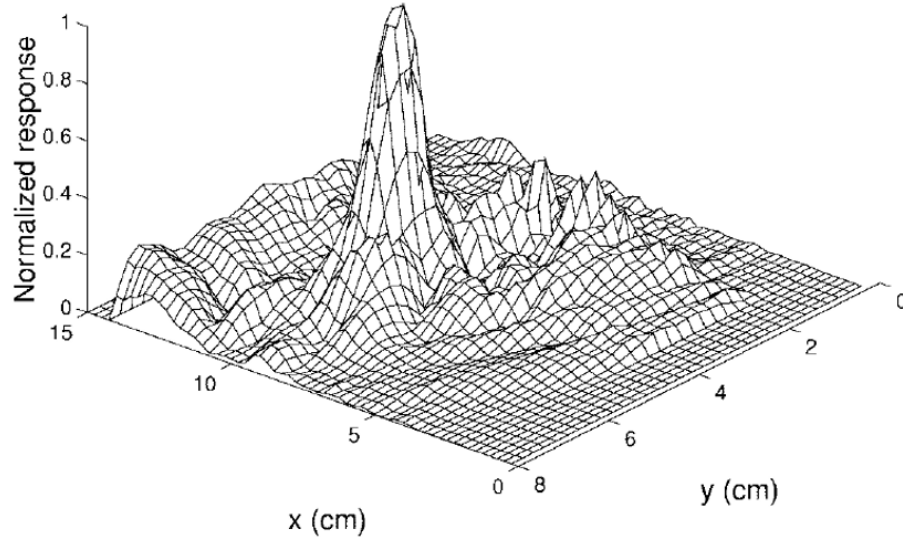


Figure 2.2: Tumour location inside the breast is indicated by the maximum peak [2]

algorithm where the location of the tumour could be identified in the image.

Based on these numerical studies, a simple experiment was then conducted to verify the basic concepts the proposed method as reported in [3]. Various target objects such as metal, wood and water were used to create several dielectric contrasts with their surroundings which was air. The setups of the experiment are shown in Figure 2.3 using two different antenna types. These are horn and monopole antennas. The data generations and acquisitions were carried out in the frequency domain by using a vector network analyser (VNA). In this case, only reflection coefficient (S_{11}) data were collected since the same antenna was used to transmit and receive the signals. To apply the CDAS imaging technique on the frequency domain data, an inverse fast Fourier transform (IFFT) was utilised in the post-processing to convert the data from the frequency domain to the time domain. The reconstructed image of the target is shown in Figure 2.4. It is reported that by reducing the dielectric contrast between the air and the target, the strength of the scattering signals is weakened hence increasing the difficulty in detecting and localising the target. Nevertheless, it has been verified

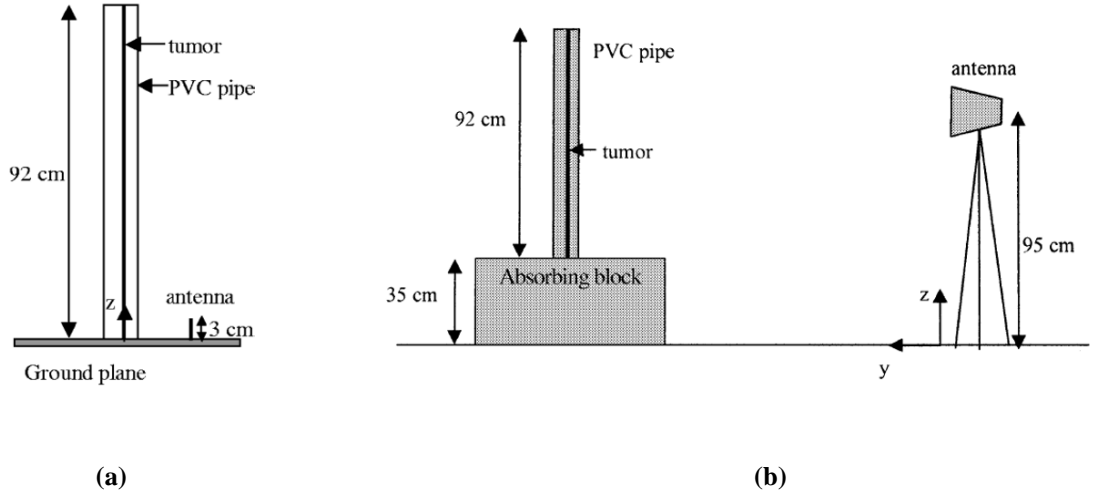


Figure 2.3: Experimental setup for initial verification of confocal imaging for breast cancer detection [3]

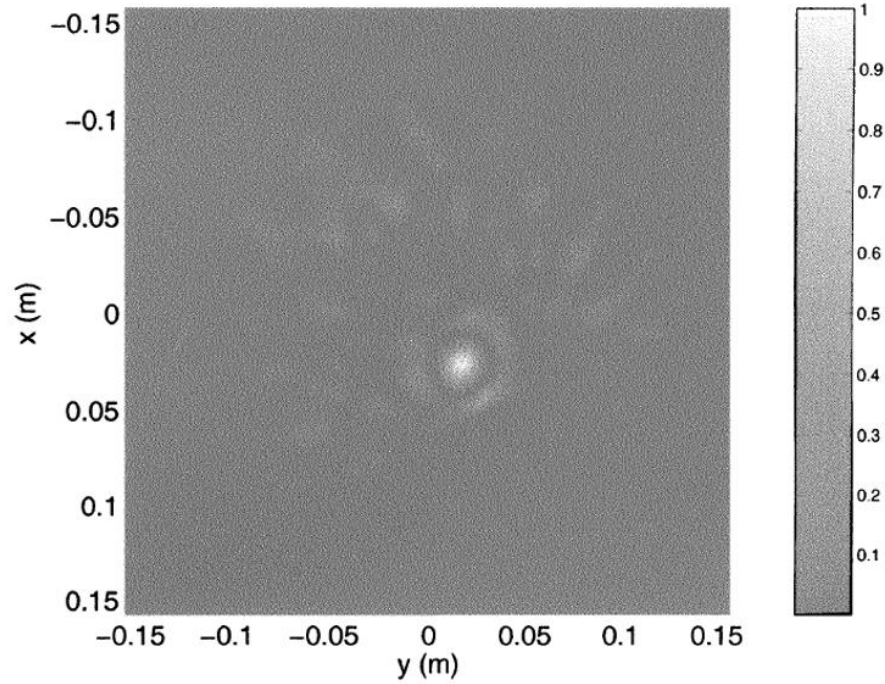


Figure 2.4: Image of the 1.2 diameter wood dowel mimicking tumour inside a PVC pipe [3]

experimentally that the radar-based microwave imaging can be used for tumour detection inside the breast.

On the other hand, an experimental work on time-domain microwave breast cancer detection system was presented in [4], [49], [50]. The advantages of the time-

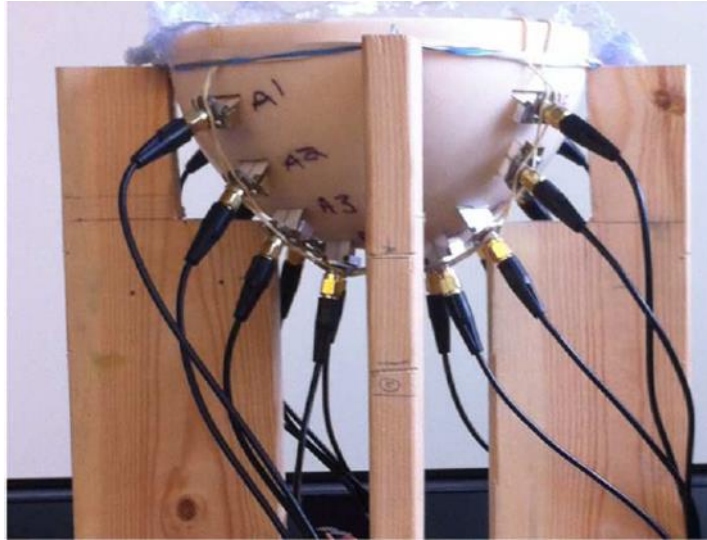


Figure 2.5: Prototype of the antenna array system for early breast cancer detection using time-domain approach [4]

domain approaches over the widely utilised frequency-domain methods are simplified signal processing steps, higher scan speeds and low cost. However, the main limitation of such systems is lower signal-to-noise ratio compared to frequency-domain systems. The developed breast cancer detection system with 16-element antenna array is illustrated in Figure 2.5. The imaging system was aimed to detect cancerous tumours

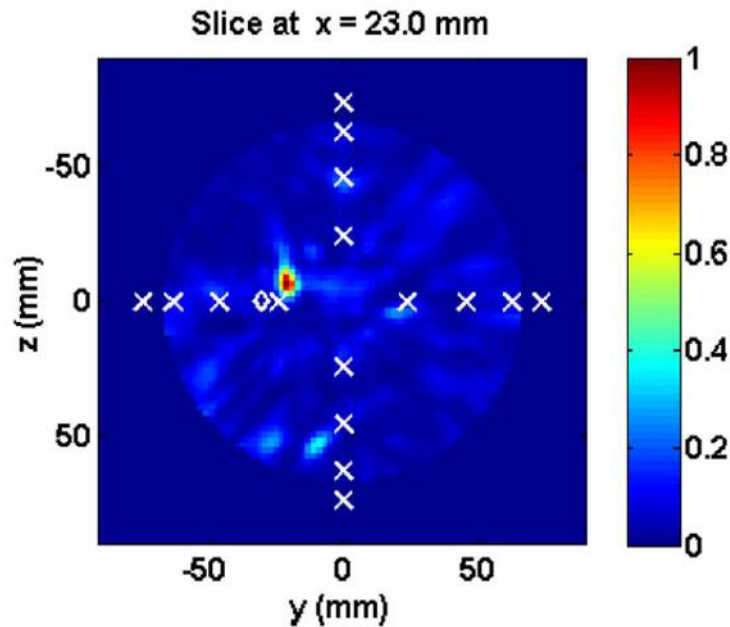


Figure 2.6: Reconstructed image of a realistic breast with tumour indicating the estimate location of the cancer [4]

at their early stage by frequent monitoring of the breast tissue. An image of a realistic breast phantom with tumour was generated by applying the confocal imaging algorithm as depicted in Figure 2.6. The location of the cancerous tumour was successfully detected.

A research group from University of Bristol has carried out clinical evaluation of their developed ultra-wideband radar scanner for breast cancer detection [5]. The latest prototype as illustrated in Figure 2.7 is the results of their previous studies where optimisations on the sensing antennas and the imaging algorithms have been done as reported in [51]–[55]. A detection rate of 74% in 86 breast scans has been reported. Based on the feedbacks of the patients undergoing the breast scans, the procedure was acceptable where it took only two minutes to perform full scan. Moreover, the lack of the breast compression is also one of the main advantages of the proposed ultra-wideband microwave imaging system. The 3-D scan of a breast generated from the prototype is illustrated in Figure 2.8. It can be seen that the system was able to detect the location of the tumour with high accuracy. Apart from the systems mentioned above, there are other research that have been carried out to improve the performance of microwave breast cancer detection systems on various aspects of the imaging

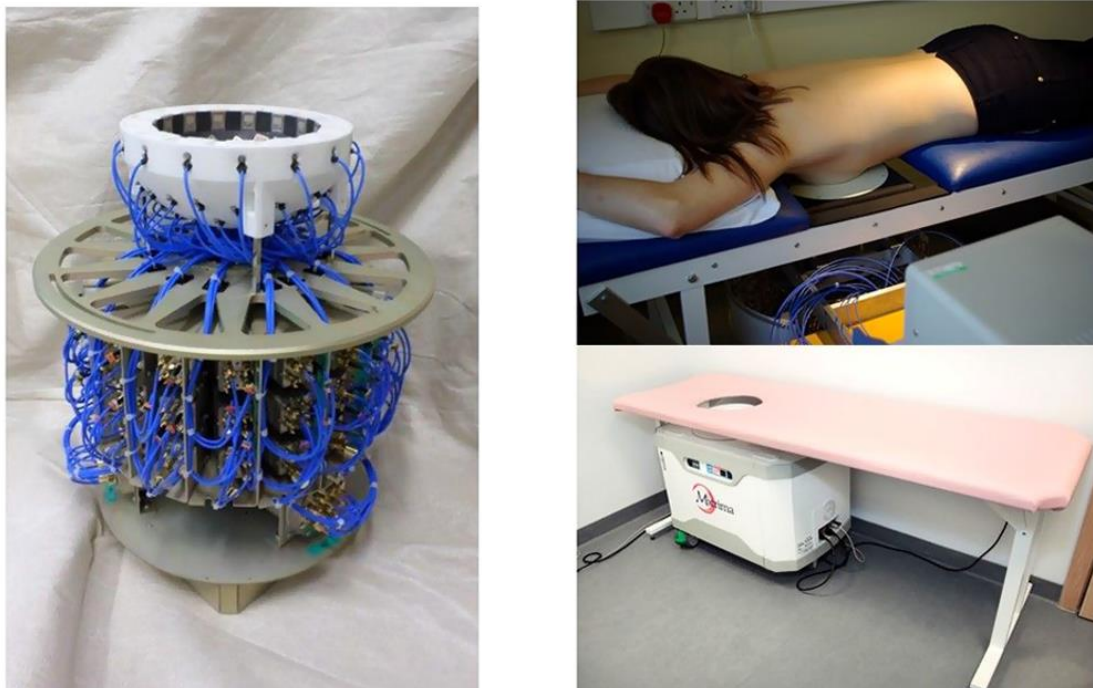


Figure 2.7: MARIA4/5 and the bed system developed by University of Bristol [5]

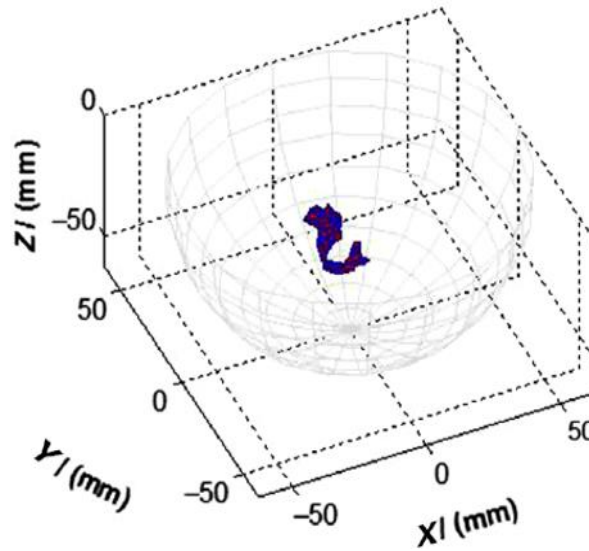


Figure 2.8: 3-D image of a breast produced by MARIA from a clinical trial [5]

systems such as the designs of the acquisition apparatus, signal generation and acquisition hardware and post-processing techniques [56]–[61].

2.2 Microwave Head Imaging and Sensing System

Compared to breast, human head consists of more tissue layers with high losses which makes the imaging process using radar-based microwave system becomes more challenging. However, based on the initial studies reported in [6], [37], microwave system for head imaging is feasible. The main finding is that in order to provide better signal penetration inside the head, low frequency electromagnetic wave is required. Moreover, even with the existence of skull, its low water content compared to other tissues such as brain resulting in higher penetration depth will permit the microwave signal to propagate through it without much attenuation [62]. Therefore, it is expected that the skull would not pose any significant challenge for the microwave signal to probe the brain. There are two main techniques used in microwave technology to image the human head. There are microwave tomography (MWT) and radar-based wideband systems. Both of these methods have their own advantages and limitations. The main differences between them are based on the frequency characteristic utilised on both systems and the final reconstructed image. Microwave tomography tries to

estimate the dielectric properties of the human body while radar-based approach attempts to find the location of the main scatterers inside it.

2.2.1 Microwave Head Tomography System

In microwave head tomography, narrowband or multi-band antennas are typically utilised to reconstruct the dielectric properties of the human head [7]. The antennas are positioned around the head and a matching medium is normally used to reduce the air-skin reflections hence increasing the transmitted signal inside the head. A feasibility study on using microwave tomography to image the human head was

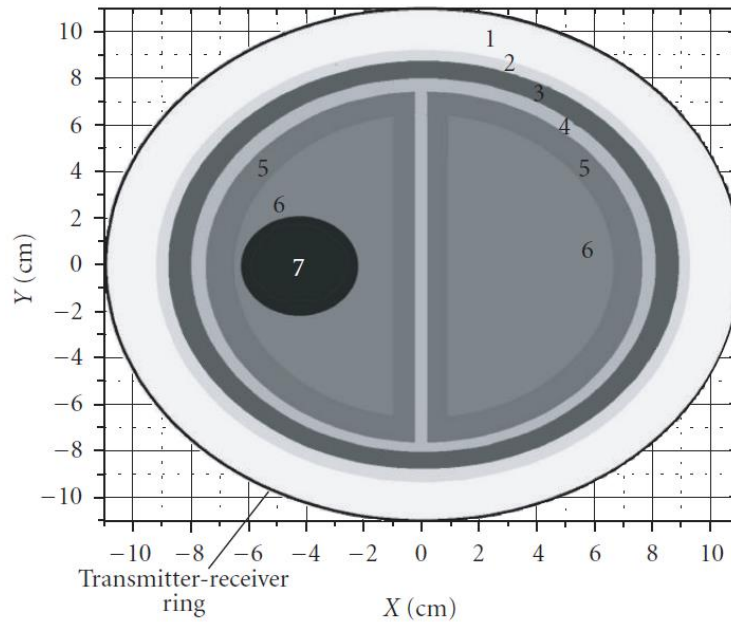


Figure 2.9: Simulated 2-D head model inside the MWT imaging chamber [6]

presented in [6] using numerical method for stroke detection. The study used a 2-D head model as shown in Figure 2.9. Realistic electrical properties of the head tissues were input into the simulator where different sizes of stroke were used.

Two different numbers of transmitters and receivers were used in the setup which are 32×32 and 64×64 . The transmitters and receivers were placed around the working chamber of radius 11cm. Both single and multi-frequency schemes were carried out across the frequency range of 0.5GHz up to 2GHz. Although the use of higher

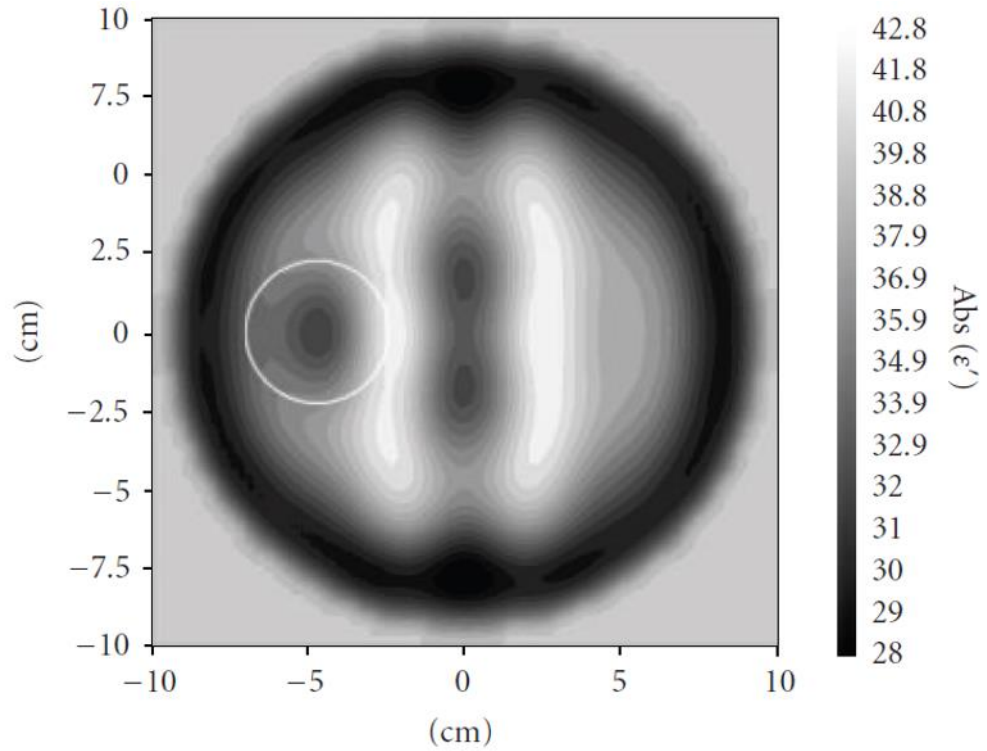


Figure 2.10: Reconstructed MWT image using multi-frequency at 0.5GHz and 1GHz [6]

frequency at 2GHz is desirable for good spatial resolution, the stroke injury area failed to be reconstructed compared to using lower frequencies at 0.5GHz and 1GHz for the single frequency approach. This is due to the higher attenuation of the EM signal as the frequency increases. However, multi-frequency technique permits the use of higher frequency for improved detection capability as shown in Figure 2.10. In a nutshell, the proposed tomography systems has shown that a 2cm diameter acute stroke could be detected.

Chapter 2: Overview of Microwave Systems for Biomedical Imaging Applications

Based on the numerical study presented above, the group developed a novel EMT imaging scanner for human brain imaging [7], [8]. The scanner as shown in Figure 2.11 was used in initial clinical studies for stroke detection. The 3D EMT system consists of 160 antennas operating at frequency range of 0.9GHz to 1.1GHz. The type of the antennas is ceramic loaded waveguide. During the imaging procedure, a matching liquid made up of glycerol and saline was used to fill the imaging chamber. A special membrane was then used to separate the matching solution from the head where it was shaped to fit the outer shape of human head. Both amplitude and phase of the electromagnetic field were measured. To reconstruct the image of the head, an iterative solver based on gradient inversion method was implemented. The imaging result of the system on a patient with ischemic stroke is illustrated in Figure 2.12. As comparison, an image from MRI scan was also obtained. The capability of the system to detect stroke was verified since the area of the stroke shown using the EMT system agrees well with the MRI image. Since the objective of the MWT systems is to

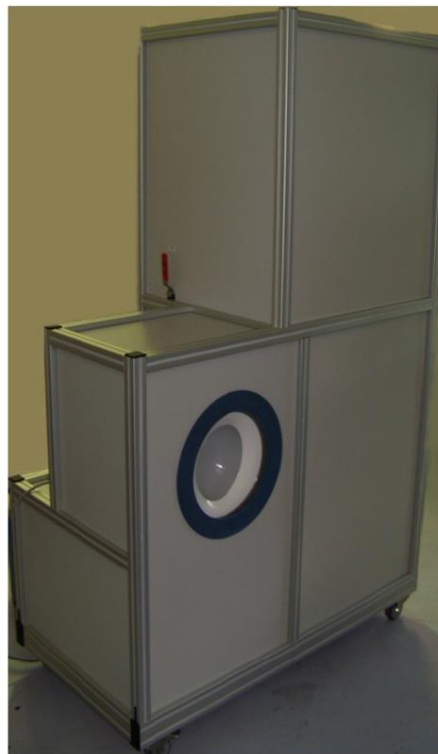


Figure 2.11: EMTensor Brain Imaging System Generation 1 [7]

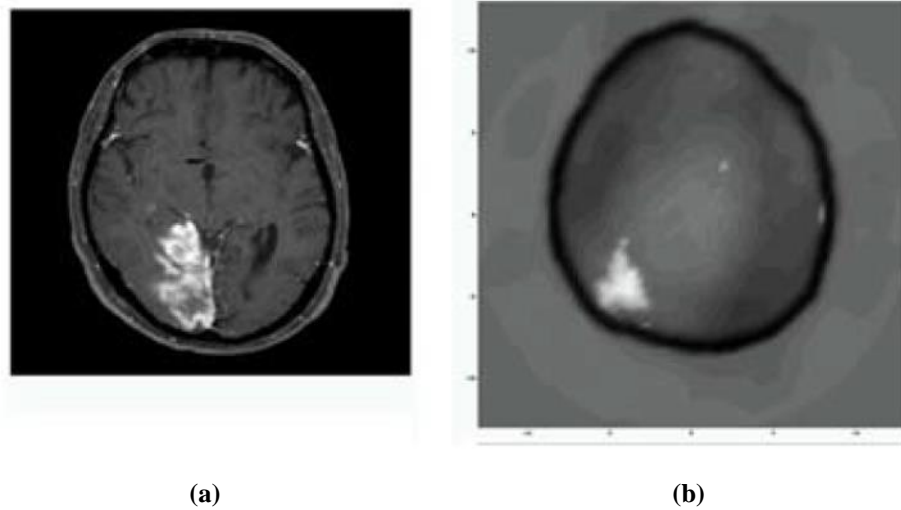


Figure 2.12: Images of a patient's head with stroke probe at 0.95GHz. (a) MRI image and (b) EMT image [8]

reconstruct the dielectric map of the head, the required computational resources are higher than those wideband radar-based microwave systems.

2.2.2 Microwave Head Sensing System

Instead of producing an image inside the head, a sensing system based on microwave technique was proposed in [9], [40]. The main objective of the system was to help doctors to differentiate types of stroke a patient might have so that a correct treatment could be given. This is due to the fact that thrombolytic therapy if given to patients with haemorrhagic stroke will worsen their condition where sometimes it could lead to death. The frequency used in the system is 0.3 to 3 GHz. Two different prototypes with ten and twelve antennas arranged around the head are shown in Figure 2.13. Measurements were made to acquire the scattered data of the different transmission channels for patients with known conditions. A supervised-machine learning algorithm based on a subspace classifier method used the collected data to train the system. It was reported that the system was able to differentiate stroke patients from healthy volunteers as well as to classify the type of stroke. A newer prototype has been reported in [30] for detection of other head diseases such as subdural hematoma as shown in Figure 2.14. It was reported that based on the clinical trial conducted, the sensitivity of the system was 100% while its specificity was 75%. The

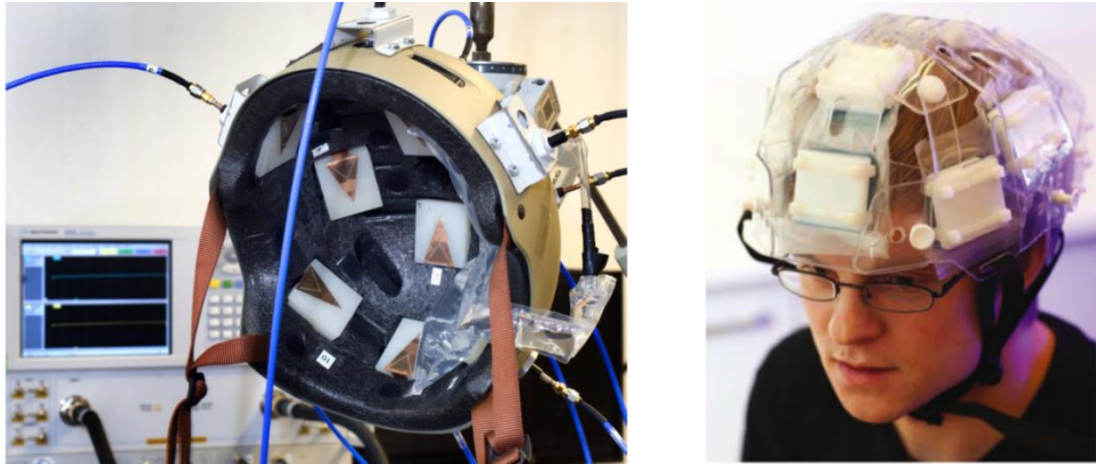


Figure 2.13: (a) First prototype with 10 patch antennas and (b) second prototype with 12 patch antennas [9]

sensitivity of a clinical trial shows the ability of the test to correctly identify patients with the disease. On the other hand, the specificity refers to the ability of the test to correctly identify patients without the disease [63]. The prototype is portable and a full measurement takes about 45 seconds to complete. One of the limitation of the proposed sensing devices is the lack of image produced to determine the position and the size of the brain injury. This additional information might be valuable to medical practitioners before performing any surgery to a patient.



Figure 2.14: The Strokefinder MD100 by Medfield Diagnostics AB [123]

2.2.3 Wideband Radar-based System

Wideband radar-based system for head imaging offers several advantages over the tomography and sensing based systems. In radar-based head imaging system, the main objective is to locate the main scatterers inside the head which eventually will lead to detection of stroke or any other abnormalities. Compared to microwave sensing systems, an estimated location of the stroke can be obtained which will provide useful information to doctors. In terms of the complexity in solving the inverse scattering electromagnetic problem faced in tomography method, the use of wideband method is able to simplify data processing and reduce the computation resources and time to reconstruct the image inside the head. As such, for a portable and standalone wearable device for head imaging which require fast detection or even real-time monitoring, a wideband radar-based system has more potential over the tomography method.

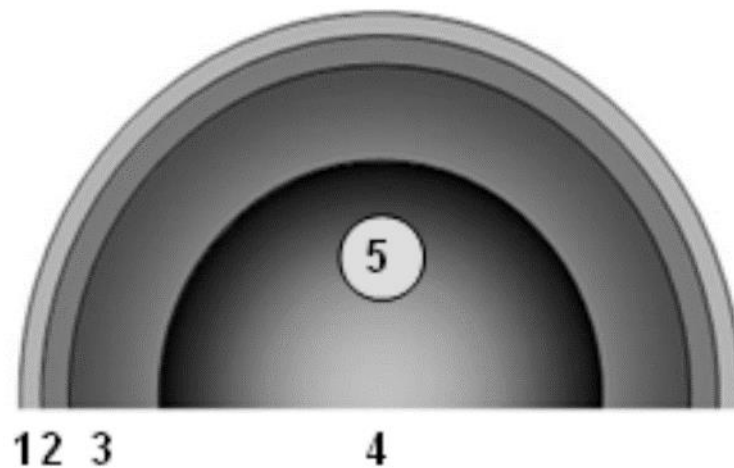


Figure 2.15: 2-D view of the simulated head model for stroke detection [10]

Wideband radar system for head imaging is mainly utilised in three different approaches which are mono-static, bi-static and multi-static configurations. All these configurations have their own advantages and limitations. Feasibility study using radar-based technique for head imaging have been reported in [10] using numerical simulations. Vivaldi antenna was adopted in the simulations due to its directional radiation beam and high gain. A 3-D spherical head model consists of several biological tissue layers namely skin, skull, grey matter and white matter as shown in

Figure 2.15 was used in the simulation where a 3cm in diameter haemorrhagic stroke with electrical properties similar to blood was embedded inside the model. By using a bi-static approach, one antenna was used to transmit the EM signal while the other antenna received the back-scattered signal. The operating frequency of the antenna was 1.5GHz to 5GHz. The distance between the antennas was kept at 20mm. The process of transmitting and receiving the signal was then repeated for different pre-defined positions to sweep the whole aperture of the head model. An improved version of delay-and-sum (DAS) algorithm called DAS Coherence Factor (DAS-CF) was applied to create an image of the head model as shown in Figure 2.16. This study shows promising result in using radar-based technique for stroke detection. Another numerical simulation was carried out in [64] using similar method albeit with antenna with higher operating frequency which is from 5GHz to 10GHz for brain cancer detection. It has been shown that higher frequency range will not be able to penetrate deep inside the human head. Only tumours which were closed to the surface of the head model showed differences in the scattered signals.

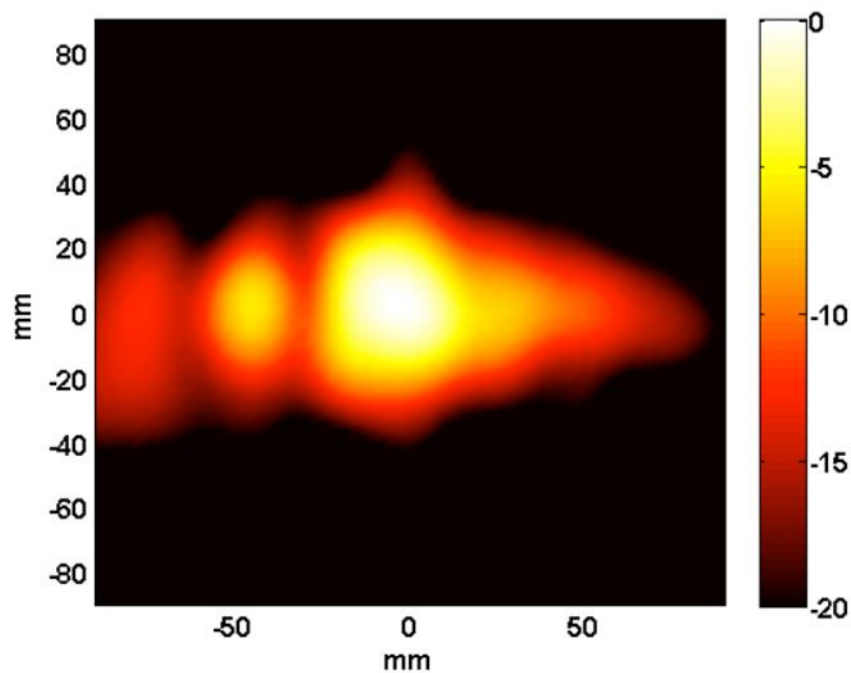


Figure 2.16: Reconstructed image of the head model using DAS-CF imaging algorithm [10]

Considering that most of the signal generations and acquisitions for microwave medical imaging systems are carried out using vector network analyser (VNA), where the collected signals are in frequency domain, an investigation of the effects of stroke toward the collected S-parameters for both the reflection and transmission coefficients is required. In [41], a numerical simulation is carried out to detect haemorrhagic stroke by comparing the difference of the S_{11} signals between healthy and unhealthy heads. It was reported that across the frequency range from 2GHz to 3.5GHz, the reflection coefficient of the probing antenna is higher when the antenna is facing a section of the head phantom with haemorrhagic stroke compared to a healthy head model. Based on this finding, a complete microwave head imaging based on radar-based technique was proposed in [11]. 16 Vivaldi antennas were utilised in the setup as shown in Figure

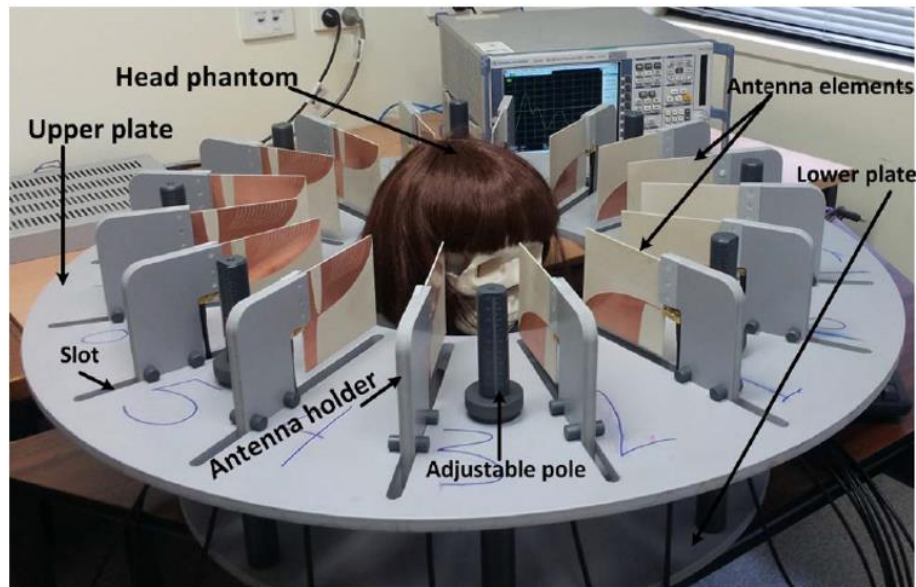


Figure 2.17: Radar-based microwave head imaging system [11]

2.17. The operating frequency range of the antennas is from 1GHz to 4GHz. The antennas operated in mono-static configuration where the same antennas act as transmitter and receiver. To adapt the confocal imaging algorithm, an inverse Fast Fourier transform was applied to the measured S_{11} data to convert it to time-domain signals. A realistic artificial human head phantom was fabricated for testing purposes. No matching medium was used in the system to reduce the complexity of the system.

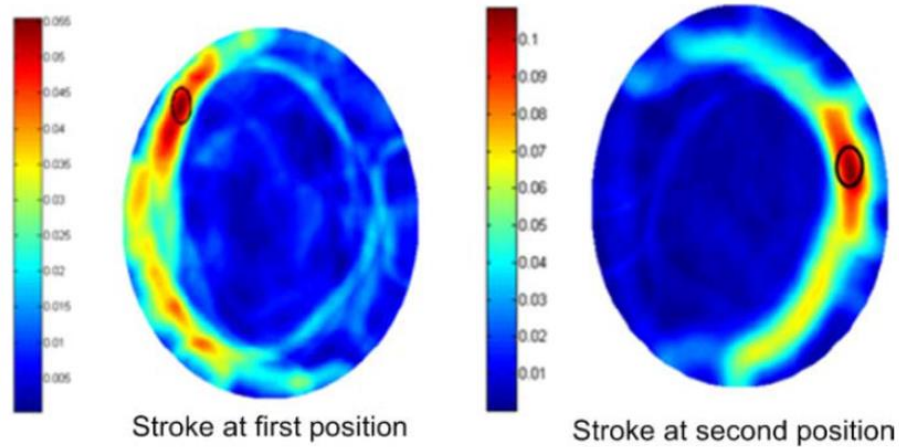


Figure 2.18: Resulting images of two different locations of a haemorrhagic stroke [11]

The distance between the antennas and the head model was kept at 5mm during the measurements. Two haemorrhagic stroke locations were detected successfully as shown in Figure 2.18.

An improvement on the antenna design proposed in the previous work has been carried out by the same research group by utilising a 3-D folded dipole antenna structure for portable microwave imaging system for traumatic brain injuries detection. To make the imaging system portable, a custom-made compact transceiver system was utilised in the measurement setup for signal transmission and data acquisition. Several variations of the antennas have been reported in [15], [28], [42], [65]. A realistic human head phantom was fabricated using 3-D printing technology to validate the detection capability of the systems [66]. An improved prototype has been developed for future clinical trial as illustrated in Figure 2.19 utilising 16 of the 3-D folded compact antennas [12]. The portable microwave system for head imaging was aimed for on-site rapid diagnostic of traumatic brain injuries which could occur in vehicular accidents, sports or other causalities.

Compared to other applications of microwave radar-based systems, such as breast cancer detection, only few research have been reported for head imaging. Furthermore, none of them has been proposed for wearable applications. Thus, there is a pressing need for wearable device for wideband microwave head imaging where it can be used for frequent measurements or even as real-time monitoring device. This

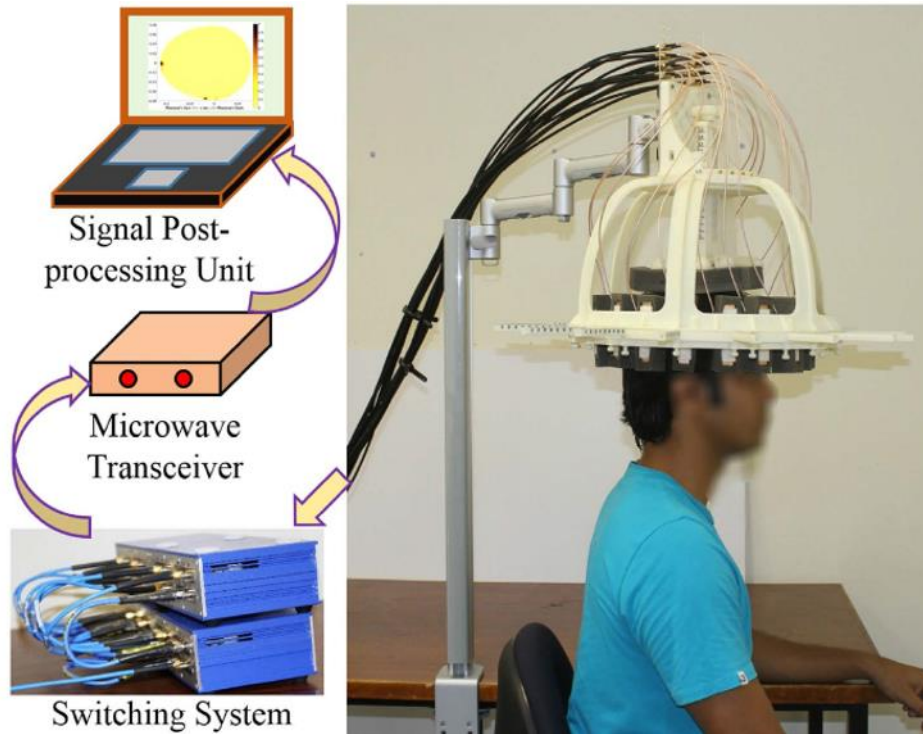


Figure 2.19: Microwave head imaging system for on-site rapid diagnosis of intracranial hematoma [12]

requires different kind of antennas where flexibility and comfort will be the main priorities for the proposed wearable head imaging systems whereas at the same time able to provide comparable performances as the typical rigid antenna designs implemented using printed circuit board (PCB) substrate such as FR-4.

2.3 Overview of Proposed Wearable Microwave Head Imaging/Sensing for Stroke Detection

Recently, there have been an emerging trend of using wearable devices to monitor a person's health in real-time [67]–[71]. The main objective of this wearable system is that the need for patients to visit a doctor can be minimised where the monitoring is done wirelessly over the internet. In addition, by providing a real-time detection, rapid response can be delivered to the patient using an alerting system. This can potentially prevent the patient from suffering a permanent health damage or in extreme cases from dying such as in a situation where a person is suffering from stroke. An example of the wearable systems for health monitoring is a wearable pulmonary edema monitoring sensor presented in [13]. The sensor was made of 17 electrodes with

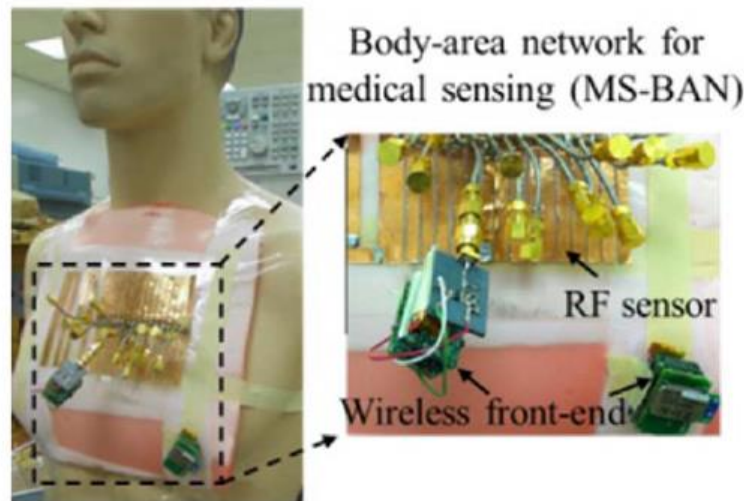


Figure 2.20: Pulmonary edema monitoring sensor with body area network [13]

16 ports in-between where it was placed on the human chest as shown in Figure 2.20. The system was built to detect lung irregularities by measuring the lung's average permittivity in a non-invasive way. The system was integrated with body-area network (BAN) to provide remote data transfer.

In this section, the concept of wearable microwave head imaging system specifically for stroke detection using flexible antenna array is described. The wearable microwave head imaging is very attractive for medical applications such as for real-time bedside monitoring systems or as body worn devices [72]. The previous research on microwave head imaging systems mostly employed high profile antenna structure thus could only be used for static screening applications [11]. Although several low profile antennas have been proposed in the literature [28], [32], their rigid structures are still unsuitable for wearable applications. Thus, flexible antennas are seen as the best candidate for this purpose. Instead of rigid antenna substrate, the use of flexible and thin substrate in addition to flexible dielectric absorber proves to be decisive for the realisation of a conformal antenna array [16]. In addition, the use of textile material for the implementation of the sensing antennas in the system allows for the sensors to be embedded in clothing items for long-term monitoring of patients at low cost [44]. Moreover, the wearable devices can be easily configured based on each individual's need. Another potential application of the wearable head detection system is for the monitoring of professional workers involved in extreme working conditions where

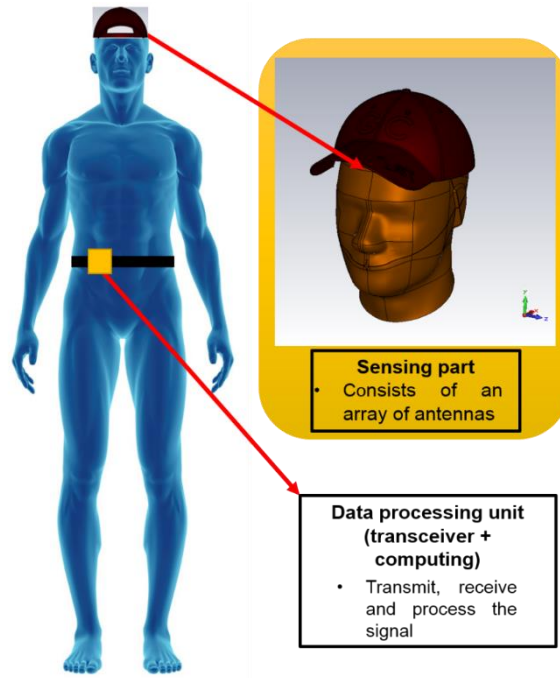


Figure 2.21: Wearable Sensing and Detection Applicator for Head Diagnostics

there is high risk of accidents. An external force to the head could potentially cause a bleeding inside the brain without any visible damage to the head. This extremely harmful condition is normally goes unnoticed and most of the time leads to death. An example of the proposed wearable system is shown in Figure 2.21.

Portable microwave imaging systems proposed in [28], [32] used a compact custom made vector network analyser (VNA) for the signal generation and acquisition. In order to move towards wearable applications, a stroke detection – body area network (BAN) system as shown in Figure 2.22 is proposed. The system consists of a sensor device, an UWB RF circuit and a wireless communication system for remote data transfer. However, the main work presented in this thesis focuses on the design of the flexible antenna array and its integration with a compact RF switching system to form a wearable interface (highlighted in dotted box in Figure 2.22) and not on the UWB RF circuit and wireless communication system. For the validation of the detection capability of the proposed wearable antenna system, the signal generation and acquisition are carried out using a VNA as opposed to UWB RF circuit as mentioned in Figure 2.22. However, it is planned that in future work, an integration with a

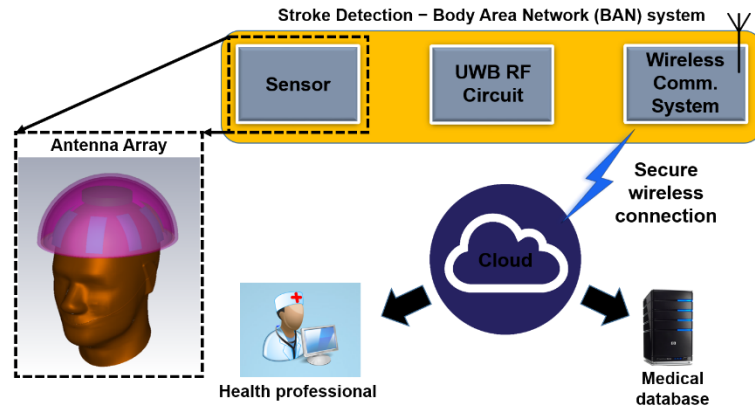


Figure 2.22 Overview of stroke detection Body Area Network (BAN) system

compact and wearable UWB RF transceiver circuit replacing the VNA will produce a standalone stroke detection and monitoring BAN systems.

2.4 Summary

This chapter starts with descriptions of wideband microwave imaging systems for breast cancer detection in the literature. Next, microwave-based head imaging systems are discussed by emphasizing their advantages and limitations. It has been found that research on microwave head imaging systems are only recently starting to gain traction compared to breast cancer detection systems. This is driven by the finding that by utilising low frequency EM signal, the detection of anomalies inside the brain such as haemorrhagic stroke is feasible where several experiments on realistic artificial head phantom have been reported in the literature with promising results. Finally, an overview of the wearable head imaging system is described by employing flexible and wearable antenna structure. It is hoped that the proposed wearable system is able to be used for medical diagnosis equipment in the hospitals and as real-time wearable monitoring systems.

Chapter 3: Flexible Antenna Design for Wearable Microwave Head Imaging Device

The performance and detection capability of a microwave head imaging system heavily depend on the efficiency of the probing antennas. For a mono-static head imaging system, the same antennas will act as the transmitters and receivers. There are several aspects of the antenna design that need careful consideration to ensure an efficient antenna for wearable head imaging is realised. These aspects are sufficient penetration of EM signal inside the human head, compactness of the antenna, flexibility and good impedance matching performance considering that the antenna need to operate at close proximity or in contact with the head. This chapter will describe the requirements of designing a wearable antenna and subsequently present the development of flexible antennas for wearable medical applications.

3.1 Requirement of a Wearable Antenna for Head Imaging Systems

There are several distinctive requirements of wearable antennas for biomedical imaging applications compared to standard rigid antennas. These are flexibility, lightweight and comfort to the wearer especially if the imaging systems are designed for monitoring applications such as bedside monitoring for stroke patients. Thus, rigid antennas made from PCB technology are no longer suitable for these wearable applications. Furthermore, a low-profile antenna is vital to ensure that the antenna can be comfortably worn by patients. As a result, high profile antennas such as Vivaldi antennas, although capable of providing high gain and directional radiation beam pattern, are not suitable for wearable applications.

In this section, several antenna designs used for radar-based microwave head imaging are first presented. One of the most commonly adopted antennas is travelling wave antennas such as Vivaldi antenna. The selection of Vivaldi antenna is mainly driven by its directional radiation pattern and high gain. Vivaldi antennas have been proposed in [10], [11], [64] for head imaging in both numerical and experimental

Chapter 3: Flexible Antenna Design for Wearable Microwave Head Imaging Device studies. A typical structure of Vivaldi antenna is shown in Figure 3.1. Due to its inherently large structure, a number of methods have been proposed to miniaturise its dimension such as cutting slots on the radiating elements of the antenna or using high permittivity substrate. Nevertheless, due to its high profile structure along the direction of propagation, Vivaldi antenna is unsuitable for wearable applications.

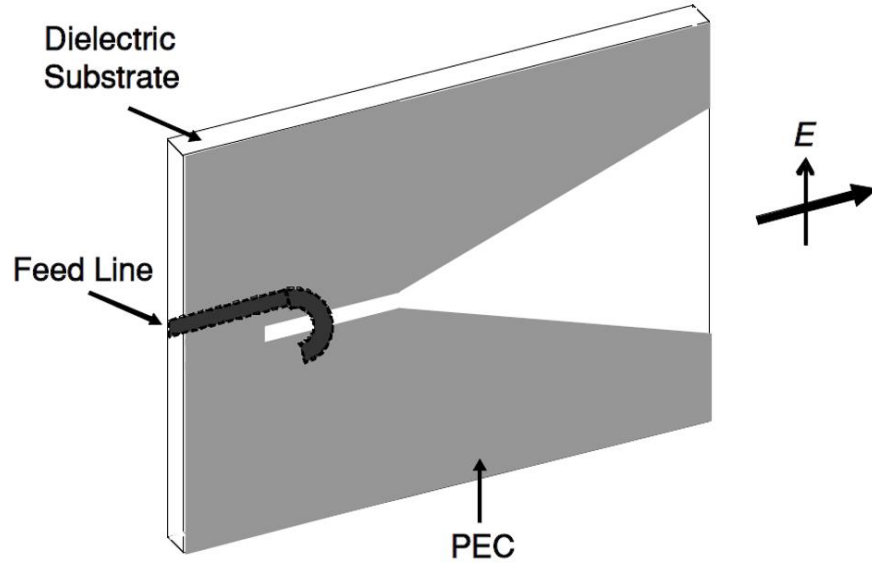


Figure 3.1: Vivaldi antenna in its basic form [14]

More compact antenna designs have been proposed in [12], [15], [28], [32] by utilising 3-D folded dipole antenna where the profile of the antennas were reduced significantly. Moreover, due to the back metal ground of the antennas, the directivity of the antenna is increased compared to typical dipole configuration. One of the design variation of the antennas is shown in Figure 3.2. The total dimension of the proposed antenna is $20\text{mm} \times 80\text{mm} \times 10\text{mm}$. The compact antenna structure have paved the way for portable microwave imaging application. However, the rigidity of the compact antennas still makes it incompatible for wearable sensing device.

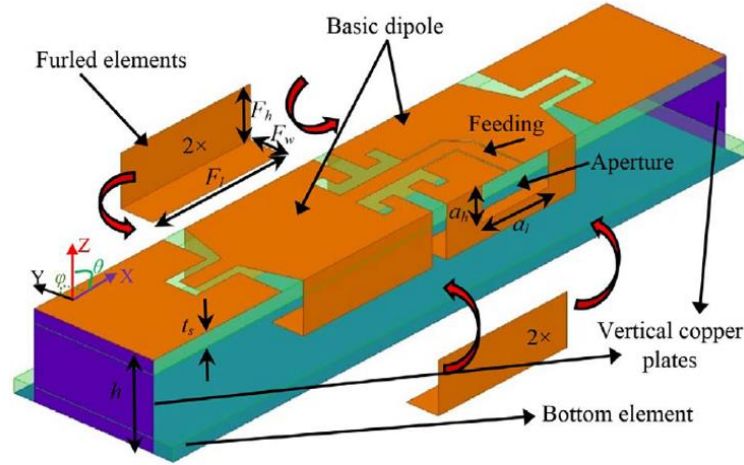


Figure 3.2: 3-D compact folded dipole antenna for microwave head imaging [15]

In this thesis, the wideband microwave head imaging system is further advanced by utilising flexible materials for wearable applications. The main objectives of having wearable devices are that the detection and monitoring process can be made portable or as real-time monitoring system as well as providing more comfort to the patients. There are numerous research that have been done on flexible and wearable antennas mainly for wireless body area network (WBAN) [73]–[77]. Wearable antennas are meant to be part of daily clothing for communications purposes such as navigation and tracking and mobile computing. The introduction of inkjet printing technology to the antenna community has opened up a new way of fabricating antennas. The use of inkjet printing method makes it possible to print an antenna on any thin and flexible substrate. The most commonly used substrate for flexible antennas is polymer based material such as Kapton polyimide and PET [78], [79]. In addition, conductive textiles have been widely employed for the construction of wearable antenna to facilitate seamless integration with garments. The EM signals transmitted by these antennas are not intended to probe the human body but instead they are used to communicate between wireless devices located inside, on or around the human body.

For microwave medical imaging, a 16 flexible monopole antenna array has been reported in [16] for wearable breast cancer detection as shown in Figure 3.3. The

radiating element of the antennas was made out of silver using inkjet printing method on Kapton polyimide substrate. The antennas has been optimised to operate in-contact with the breast where the operating frequency range is 2GHz to 4GHz. On the other hand, a wideband textile monopole antenna for microwave head imaging was proposed in [17], [80]. The reported work investigated the specific absorption rate (SAR) of the antenna to validate its safety for use for microwave imaging system. The size of the antenna is $80\text{mm} \times 77.5\text{mm} \times 0.7\text{mm}$. The material used for the antenna substrate is denim jean while the radiating part of the antenna is made of super conductive textile. No detection or imaging work has been reported.

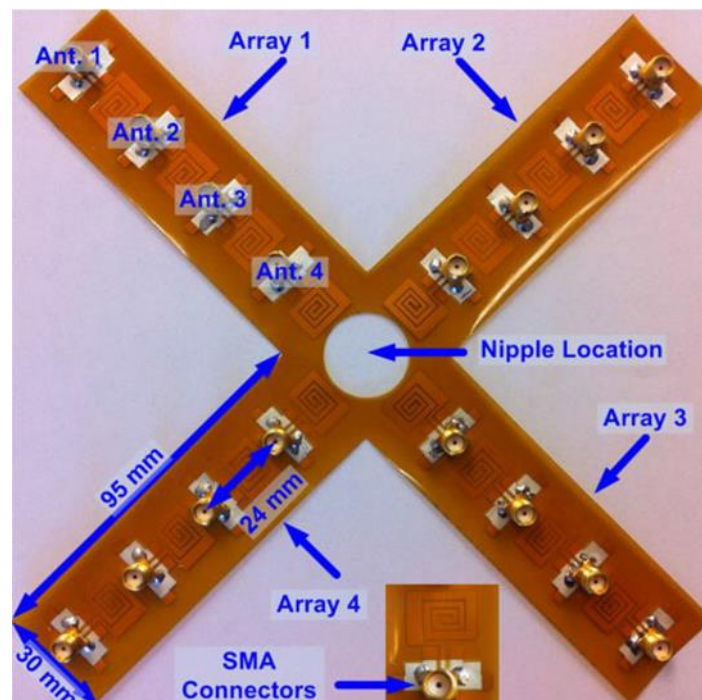


Figure 3.3: 16 flexible antenna array for breast cancer detection [16]

Based on the literature, it have been found that flexible antennas for practical wearable head imaging applications have not been properly explored and investigated. Therefore, the purpose of this thesis is to design flexible antenna for wearable head imaging applications and to verify its performance specifically for detection of haemorrhagic stroke inside the head.

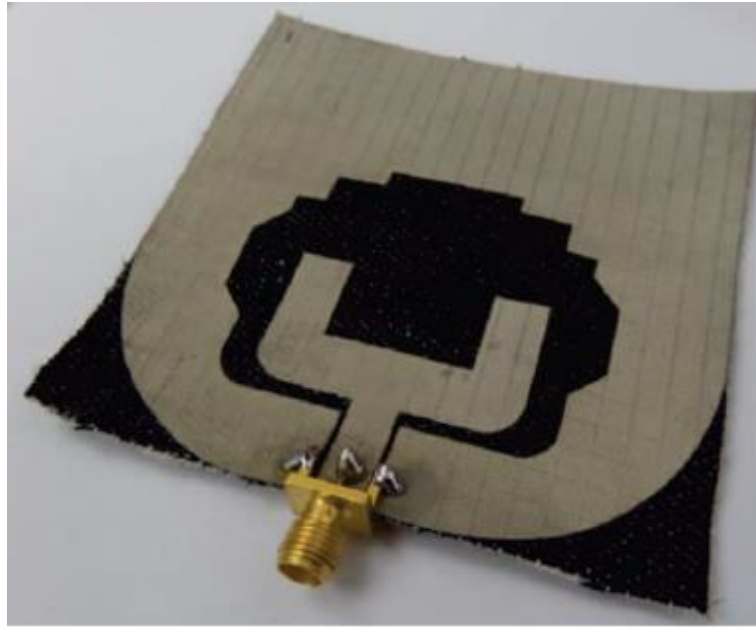


Figure 3.4: Wideband textile antenna for microwave medical imaging [17]

3.2 Development of Wideband Planar Monopole Antenna Design using Flexible Substrates

3.2.1 Introduction

Based on the requirements of the sensing antennas discussed above, planar monopole antenna has been carefully chosen due to its numerous advantages over other antenna types including wideband, low-profile, compact, and its capability to transmit and receive wideband signals without significant distortions. Many variations of planar monopole antennas have been investigated and reported in the literature employing various shapes and slots for the radiating elements of the antennas including squares, rectangles, circles, ellipses and trapezoids [81]–[86].

Additionally, there are numerous research that have been reported in the literature on flexible antennas for various applications ranging from radio frequency identification (RFID) to WBAN applications. On the other hand, only few research have been carried on flexible or wearable antennas for biomedical imaging applications. The first work on flexible antenna for radar-based imaging system was reported in [16] for breast cancer detection where 16 monopole antenna elements were

used to form an array that was shaped to a human breast. The advantages of the proposed flexible array are light weight, low cost, ease of fabrication and able to provide comfortable screening procedure.

In this section, several variations of planar monopole antennas were investigated and optimised for wearable sensing antenna for microwave head imaging device. In addition, the impedance bandwidths of the antennas were optimised to cover the operating frequency range from 1.5GHz up to 3GHz which allow enough penetration depth of the EM signal inside the human head and to provide good resolution. The optimisation of the bandwidth of the planar monopole antennas mainly depends on two main aspects of the antenna structure which are the shape and dimension of the radiating part and the feeding line [18]. Full-wave simulations were carried out using CST Microwave Studio which adopts finite-difference time-domain method. Finally, the simulations results were compared to the measured results for validation.

3.2.2 Antenna Design Procedure

Planar monopole antennas have various radiating patch shapes which include square, rectangle, circular, elliptical and trapezoidal shape as illustrated in Figure 3.5 [18][14]. These radiating patches are mainly fed using two types of transmission lines which are microstrip line or co-planar waveguide. The lowest operating frequency of

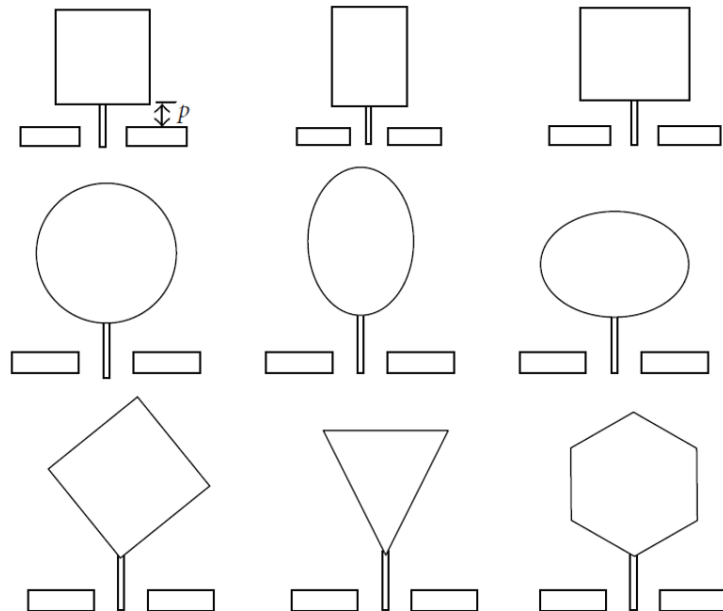


Figure 3.5: Various shapes of planar monopole antenna [18]

the monopole antennas mainly depends on the maximum length of the radiating patch and the permittivity of the substrate used whereas the bandwidth of the antennas depends on the impedance matching of the 50Ω feeding line to the various modes excited by the antennas. To estimate the lowest band edge of the monopole antennas, the standard equation derived for cylindrical monopole antenna can be used with appropriate modification [18]. The formula given in Equation (3.1) was adopted for planar cylindrical configuration by taking the height of the patch of the planar monopole, L in cm as that of an equivalent cylindrical monopole antenna and r in cm is the effective radius of the equivalent cylindrical monopole antenna which is determined by equating the area of the planar and cylindrical monopoles.

$$f_L = \frac{c}{\lambda} = \frac{7.2}{(L + r + p)} \quad (3.1)$$

Further modification on the Equation (3.1) is done to take into account the utilisation of dielectric layers used on one side of the printed monopole antenna. Hence, the more accurate equation for estimation of the lowest operating band edge of the printed monopole antenna is given by

$$f_L = \frac{c}{\lambda} = \frac{7.2}{\{(L + r + p) \times k\}} \quad (3.2)$$

where k can be calculated as $\sqrt{\epsilon_r}$. ϵ_r is the dielectric constant of the dielectric layer used in the antenna which is FR-4, PET or textile. Based on Equation (3.2), it can be

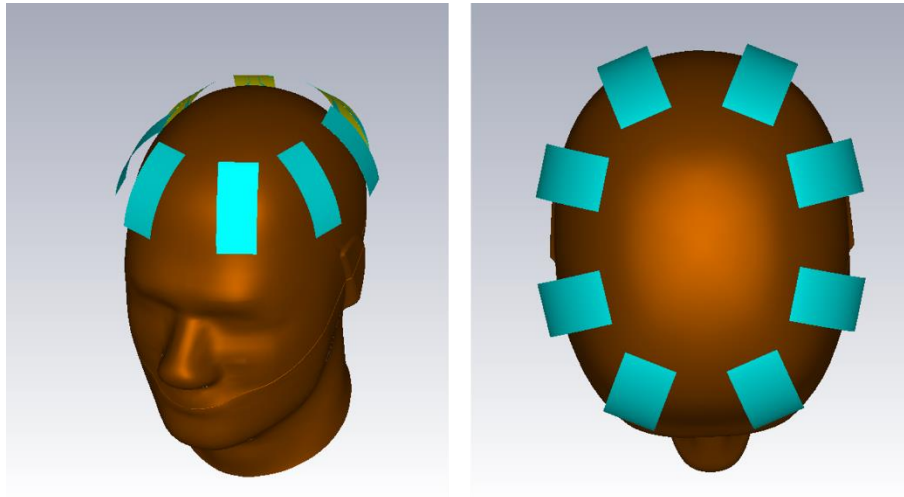


Figure 3.6: Head phantom model with the proposed monopole antennas

seen that the lowest operating band edge of the monopole antenna can be reduced by increasing the length of the antenna. As for the bandwidth, appropriate feeding line must be designed to match with the excited modes of the antenna. This is normally achieved by implementing various feeding line structures with the help of EM simulators by carrying out parametric optimisations on the structures.

An initial geometry of the proposed antenna was first selected by considering the shape of the human head and in view of making an array from the antennas. Thus, by using a head phantom model in the CST Microwave Studio software as depicted in Figure 3.6 as a reference, a rectangular shape monopole antenna where its length is longer than its width was considered. By choosing this shape as the starting point of the antenna design, an array of up to 12 antenna elements can be developed where they are arranged in elliptical configuration around the head as will be presented later in Chapter 4. Two radiating shapes have been investigated for the sensing antennas to find the optimal design which will be able to fulfil the requirements as mentioned previously. Since the antenna will be bent to follow the contour of the head, its effect on the impedance matching of the antennas will also be investigated.

3.2.2.1 Inverted Trapezoidal Monopole Antenna on FR-4 substrate

The first variation of the planar monopole antenna in this research is trapezoidal monopole antenna fed by CPW transmission line. Planar trapezoidal monopole antenna has been chosen due to its geometry where its length can be made much longer than its width as shown in Figure 3.6. To reduce the complexity of the fabrication process, a co-planar waveguide transmission line is used where it resides on the same plane of the radiating patch. For the trapezoidal monopole, the side length, T is used to calculate the values of L and r as in Equation (3.3) and Equation (3.4).

$$L = \frac{\sqrt{3}T}{2} \quad (3.3)$$

$$r = \frac{T}{4\pi} \quad (3.4)$$

The lowest frequency band edge is then calculated using Equation 3.2. The calculated lower frequency edge is 1.48GHz. The impedance of the CPW feeding line as shown

in Figure 3.7 should be matched to 50Ω and can be derived using the analytical formulas given below [87]

$$Z_0 = \frac{30\pi}{\sqrt{\epsilon_{eff}}} \frac{K(k')}{K(k)} \quad (3.5)$$

$$\epsilon_{eff} = 1 + \frac{\epsilon_r - 1}{2} \frac{K(k')K(k_1)}{K(k)K(k'_1)} \quad (3.6)$$

where

$$k = \frac{a}{b}$$

$$k_1 = \sinh(\pi a/2h) / \sinh(\pi b/2h)$$

K is the complete elliptic integral of the first kind while $k' = \sqrt{1 - k^2}$

The initial design of the antenna as shown in Figure 3.8 was then simulated in the EM solver to validate its performance against the theoretical calculation. In this section, the main aim is to find the optimal lower frequency edge that the antenna can operate to ensure sufficient penetration depth is achieved for microwave head imaging applications. It have been found that the lowest simulated frequency band edge is 1.34GHz as exhibited in Figure 3.9.

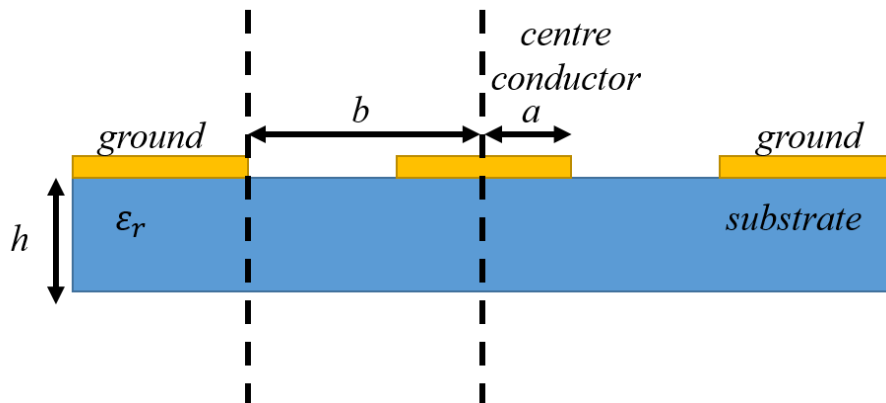


Figure 3.7: Co-planar waveguide structure

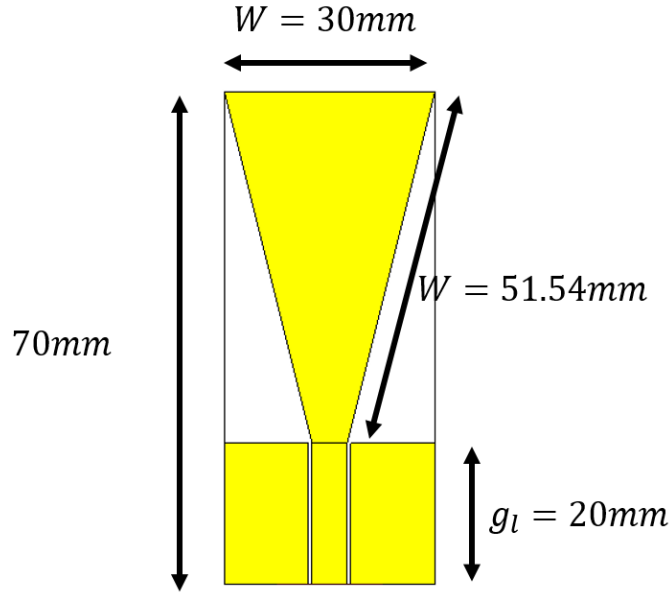


Figure 3.8: Initial design of inverted trapezoidal monopole antenna

However, the required bandwidth of the antenna has not been achieved. Therefore, optimisations on the shape of the radiating patch and the feeding line were carried out. There are several approaches that have been used to improve the bandwidth of monopole antennas [88]–[90]. One of the methods is by modifying the structure of the feeding line. It has been reported in [82] that the ground of the CPW feeding line has

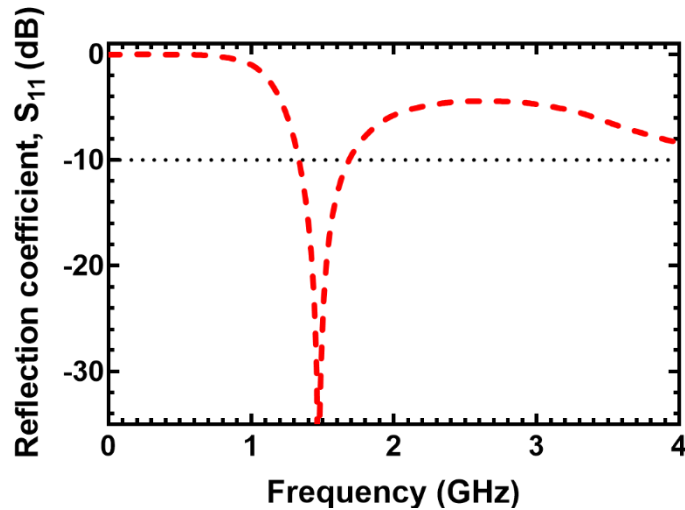


Figure 3.9: Simulated reflection coefficient for inverted triangular antenna shown in Figure 3.8

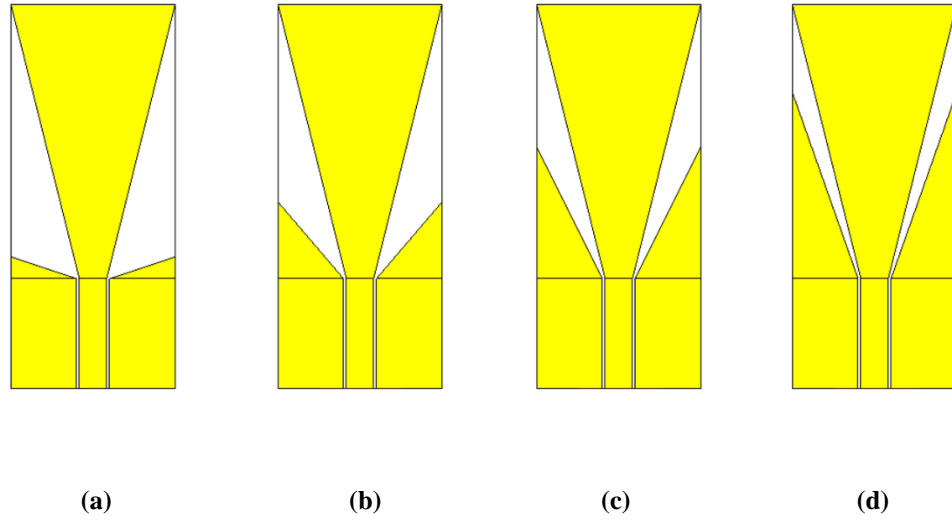


Figure 3.10: Optimisation process of the impedance bandwidth of the antenna by varying parameter g_l . (a) $g_l = 24\text{mm}$ (b) $g_l = 34\text{mm}$ (c) $g_l = 44\text{mm}$ and (d) $g_l = 54\text{mm}$

been modified by using oblique tapered slots structure which resulted in ultra-wideband antenna capable of operating from 3.1GHz to 18GHz.

For the proposed antenna, the focus was given on improving the CPW transmission line to obtain the optimal bandwidth. The ground of the CPW feeding line has been linearly tapered to provide a smooth transition for the antenna impedance

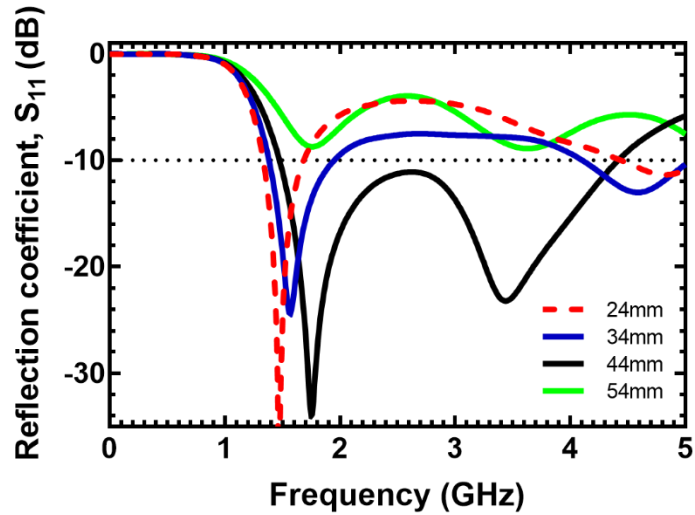


Figure 3.11: Reflection coefficients for parameter sweep for g_l from 24mm to 54mm

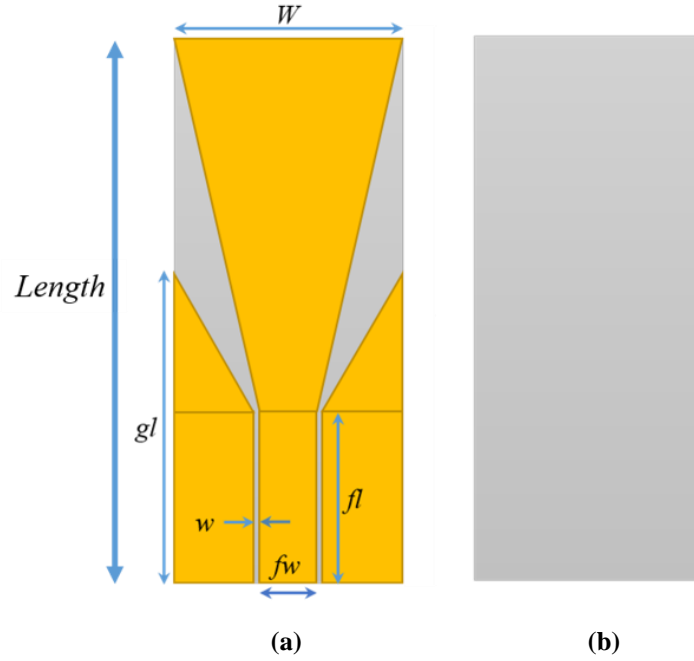


Figure 3.12: Geometry of the proposed UWB antenna (a) Top view (b) Bottom view

from the feeding line to the radiating element as illustrated in Figure 3.10. Parametric optimisations on g_l were carried out as shown in Figure 3.11. The widest bandwidth was achieved when g_l is 44mm. This leads to improved reflection coefficient of the antenna which is able to cover a frequency bandwidth of around 3GHz from 1.48GHz to 4.4GHz.

Finally, the optimised design of triangular monopole antenna is shown in Figure 3.12. Table 3.1 lists the finalised values of the antenna parameters. To investigate the polarisation of the antenna, the surface current at several operating frequencies over the antenna bandwidth were simulated as shown in Figure 3.13. It can be seen that the induced surface current distributions are aligned in the same Y -direction for all frequencies. These Y -directed currents contribute to high co-polarisation of the antenna across the antenna bandwidth which is the main polarisation the antenna is intended to operate. This will ensure the antenna is able to capture the scattered waves during measurements more efficiently.

Table 3.1

GEOMETRIC PARAMETERS OF THE TRAPEZOIDAL ANTENNA ON FR-4 SUBSTRATE

Antenna Dimensional Parameters	Symbol	Value (mm)
Antenna length	L	70
Antenna width	W	30
Thickness of the substrate	h_s	0.2
CPW gap	w	0.5
CPW feed-line width	f_w	5
CPW feed-line length	f_l	20
CPW ground length	g_l	44

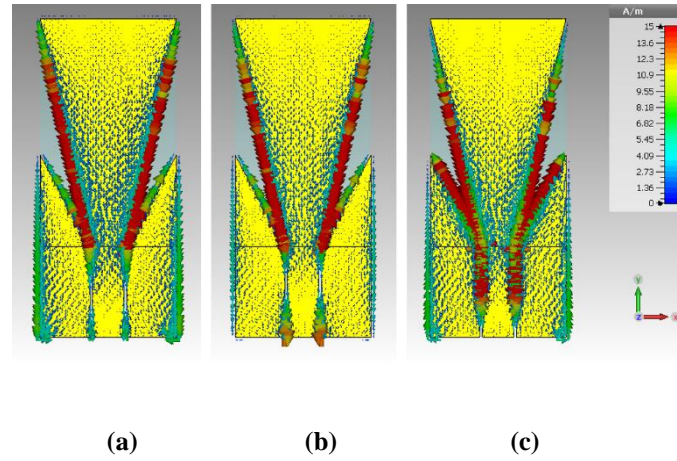


Figure 3.13: Induced current on the antenna at (a) 1.5 GHz, (b) 2.5 GHz and (c) 3.0 GHz.

3.2.2.1.1 Simulated Radiation Pattern of the Trapezoidal Monopole Antenna

Figure 3.14 shows the simulated 2-D radiation patterns of the trapezoidal monopole antenna at 1.5GHz. It can be observed that the radiation patterns are nearly omni-directional in the H-plane whereas for the E-plane, the antenna exhibits bi-directional pattern. 3-D radiation patterns of the antenna are illustrated in Figure 3.15.

It can be seen that as the frequency increases from 1.5GHz to 3GHz, the direction of the main lobe slightly diverts from the boresight direction by 30° . The maximum simulated gain of the antenna varies from 1.8dBi to 4.11dBi from 1.5GHz to 3GHz.

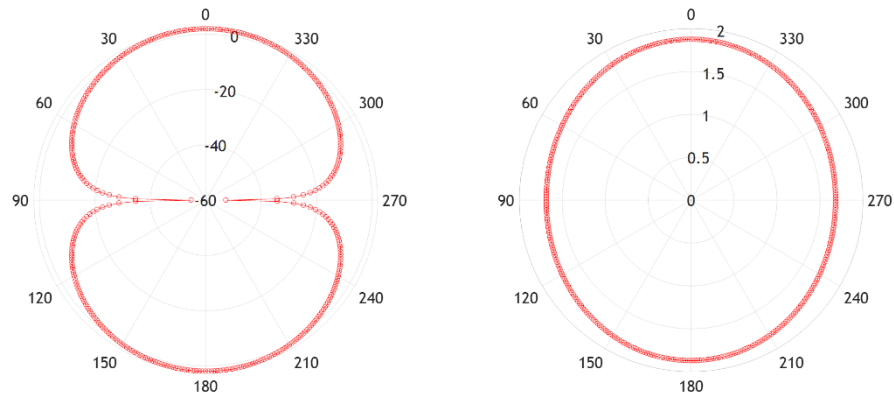


Figure 3.14: Simulated E-(XZ) and H-(XY) plane 2-D far-field radiation patterns at 1.5GHz

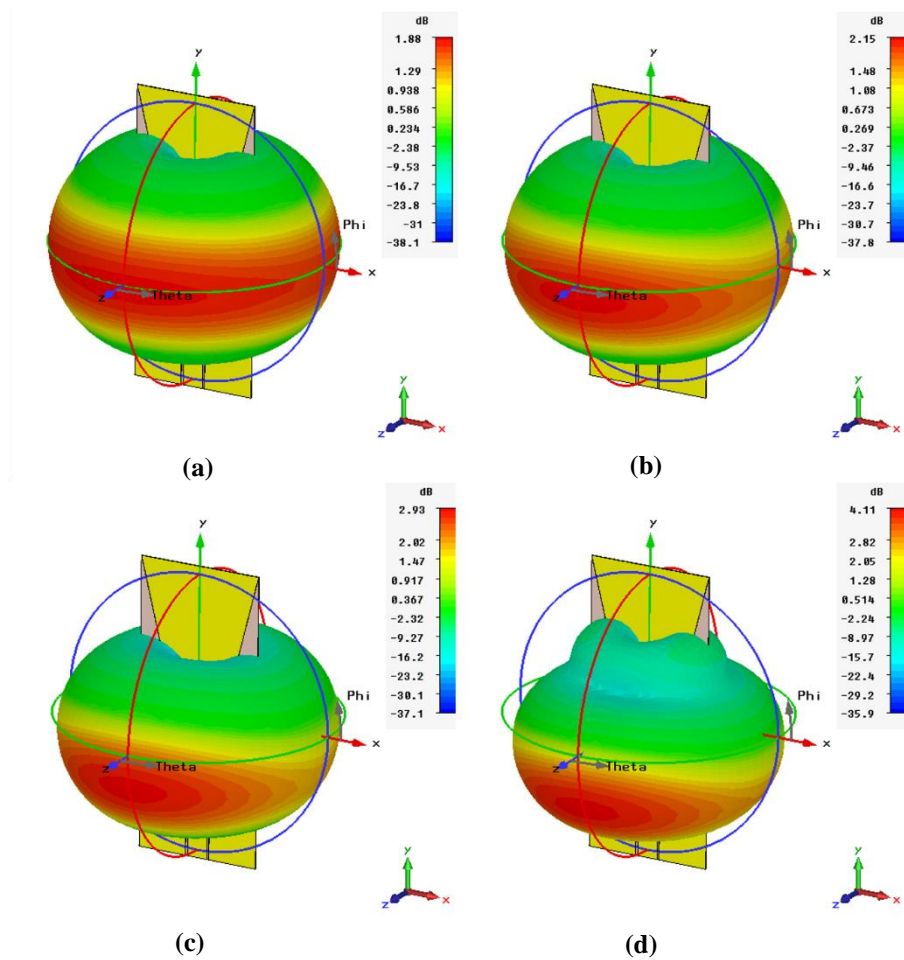


Figure 3.15: Simulated 3-D radiation patterns of the antenna at (a) 1.5GHz (b) 2GHz (c) 2.5GHz and (d) 3GHz

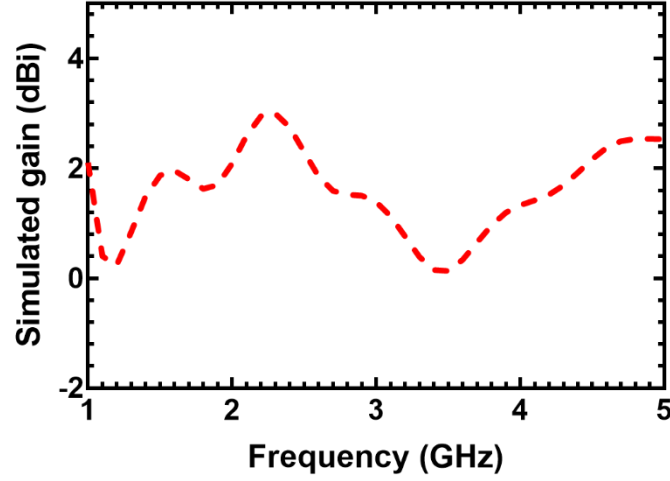


Figure 3.16: Simulated gain at the boresight direction ($\theta = 0^\circ$, $\phi = 0^\circ$)

3.2.2.1.2 Time-domain Characterisation of the Trapezoidal Shaped Monopole Antenna

Since the probing antenna operates mainly in the near-field, its performance should also be investigated in time-domain. To characterise the time-domain performance of the antenna, the Gaussian pulse in the CST Microwave Studio was utilised. The frequency bandwidth of the pulse was set from 1.5GHz to 4GHz based on the operating bandwidth of the proposed antenna.

In order to examine the performance of the antenna in the time domain, the fidelity factor and time domain amplitude responses around the antenna were calculated using the EM simulator. The fidelity factor shows the level of distortions of the radiated pulses in various directions. The value of fidelity factor varies between 0 and 1, with 1 representing the minimum and 0 representing maximum distortion of the pulses. For excitation pulse, $f(t)$ taken as the template waveform and the received pulse at any direction from the antenna, $g(t)$, the fidelity factor can be calculated by [16]

$$F = \max \int_{-\infty}^{\infty} f(t) \times g(t + \tau) dt \quad (3.7)$$

In the electromagnetic solver, co-polarized electric field (E_y) probes were positioned at a distance of 40mm from the centre of the antenna and at angular differences of 90° apart from each other. The computed time-domain responses received by the probes surrounding the antenna are shown in Figure 3.17. High fidelity factors of more than 0.92 were observed at H-plane as listed in Table 2 at all angles. This indicates a stable transmitted pulse performance which is crucial for the proposed head imaging system where the proposed antenna is able to transmit and receive a pulse with minimal distortion.

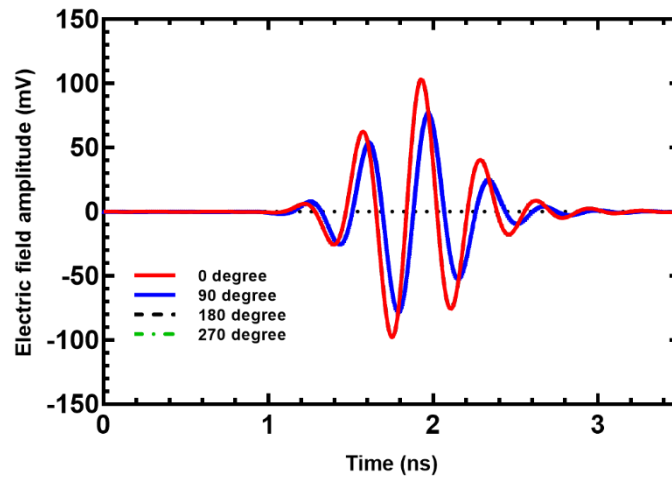


Figure 3.17: Simulated received near-field time-domain pulses radiated by the antenna at different angles without head phantom in H-plane

Table 3.2

FIDELITY FACTORS OF THE TRAPEZOIDAL ANTENNA

Angle (degree)	Fidelity Factor
0°	0.92
90°	0.94
180°	0.92
270°	0.94

3.2.2.2 Inverted Trapezoidal Shaped Monopole Antenna on PET substrate

To incorporate flexibility into the antenna design, different substrate material which is polyethylene terephthalate (PET) was utilised to replace the FR-4 substrate used in the previous design. The permittivity, ϵ_r , loss tangent, δ and thickness, h_s of the substrate are 2.4, 0.003 and 100 μ m respectively. Due to different permittivity value of the new substrate, the antenna parameters such as the CPW feeding line were optimised to achieve similar performance to that of previous design on FR-4 substrate. The final optimised parameters of the PET based antenna are given in Table 3.3. The reflection coefficient of the antenna is shown in Figure 3.18. The operating bandwidth of the antenna is from 1.3GHz to 3.5GHz with frequency bandwidth of 2.2GHz. The impedance bandwidth of the antenna decreases from 4GHz to 2.2GHz which can be attributed to impedance mismatch between the redesigned CPW feed line to the antenna's resonance modes. However, it is to be noted that frequency range above 3GHz would not be useful for head imaging applications due to its low penetration depth.

Table 3.3

GEOMETRIC PARAMETERS OF THE TRAPEZOIDAL ANTENNA ON PET SUBSTRATE

Antenna Dimensional Parameters	Symbol	Value (mm)
Antenna length	L	70
Antenna width	W	30
Thickness of the substrate	h_s	0.2
CPW gap	w	0.5
CPW feed-line width	f_w	7
CPW feed-line length	f_l	20
CPW ground length	g_l	40

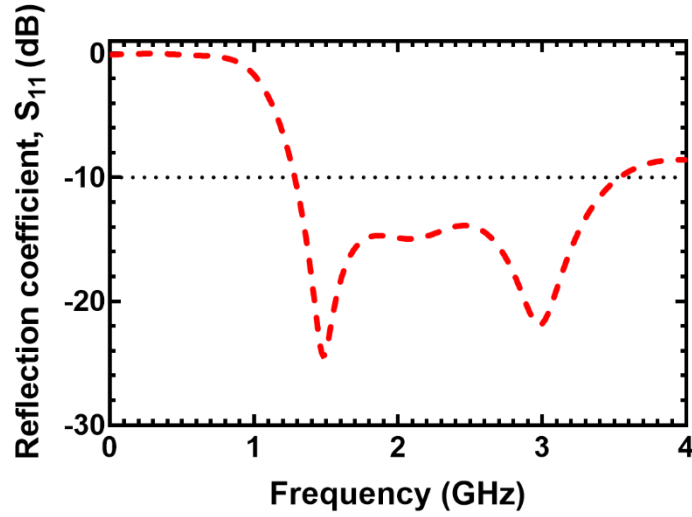


Figure 3.18: Simulated reflection coefficient of the trapezoidal monopole antenna on PET substrate

Due to almost similar antenna configuration to the previous antenna design, the radiation patterns of the antenna show similar performance as the earlier design as shown in Figure 3.19. It can be seen that the antenna with PET substrate exhibits bi-directional pattern in E-plane whereas for H-plane, nearly omni-directional pattern is observed.

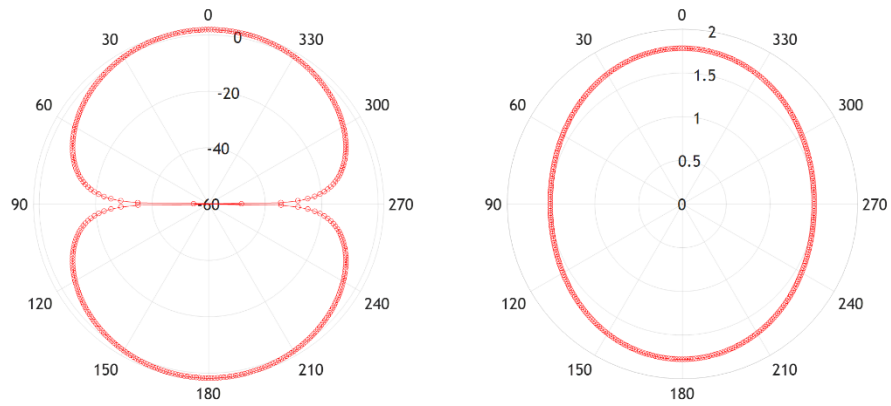


Figure 3.19: Simulated E-(XZ) and H-(XY) plane 2-D far-field radiation patterns at 1.5GHz for the trapezoidal monopole antenna on PET substrate

3.2.2.3 Elliptical Shaped Monopole Antenna using Textile Materials

The second variation of the proposed monopole antenna is a co-planar waveguide (CPW) fed elliptical monopole made from fully textile materials. The values of L and r of the antenna can be calculated using the semi-major axis, A and semi-minor axis, B of an ellipse as given in the equations below

$$L = 2A \quad (3.8)$$

$$r = \frac{4}{B} \quad (3.9)$$

By setting A and B as 32mm and 10mm respectively, the lower frequency edge of the antenna is calculated to be 1.1GHz. The substrate of this antenna is 6mm thick felt with dielectric constant of 1.2. The antenna is fed using CPW transmission line with the aim to reduce the fabrication complexity where the conducting part resides only at one side of the antenna. The elliptical monopole antenna structure as depicted in Figure 3.20 was first simulated to find the lower band edge frequency. In the initial design process, no optimisation has been made on the CPW feed line. Based on Figure 3.21,

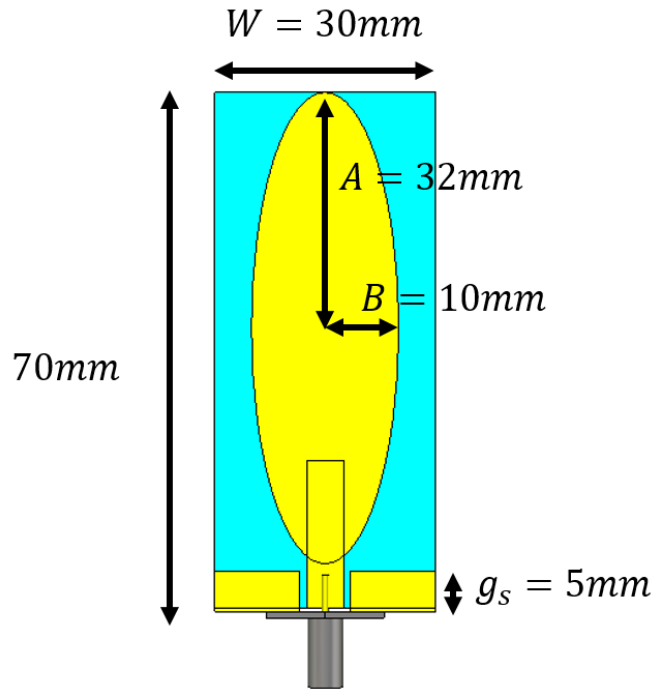


Figure 3.20: Initial design of elliptical monopole antenna

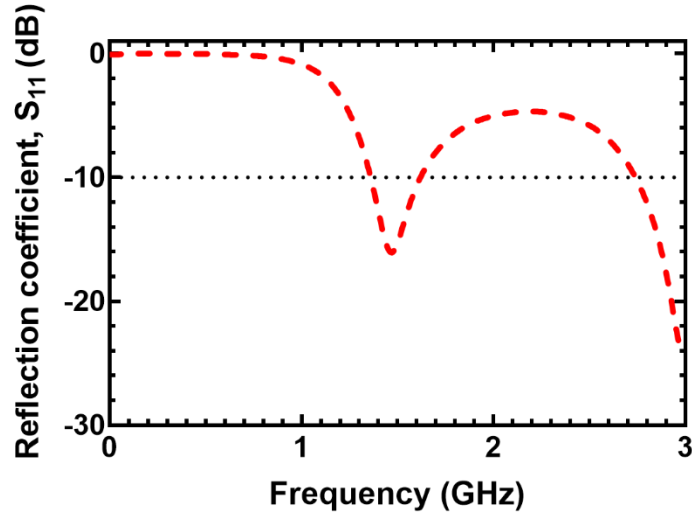


Figure 3.21: Simulated reflection coefficient of elliptical monopole antenna

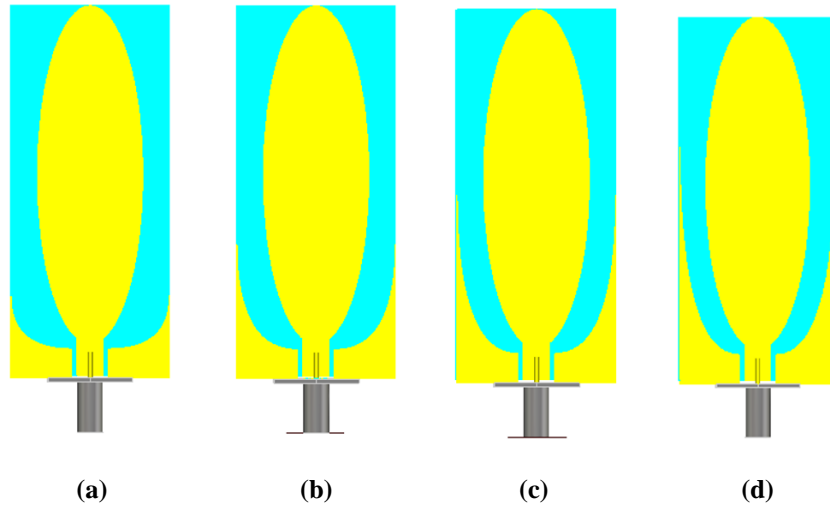


Figure 3.22: Optimisation process of the impedance bandwidth of the antenna by varying parameter g_s . (a) $g_s = 15\text{mm}$ (b) $g_s = 25\text{mm}$ (c) $g_s = 35\text{mm}$ and (d) $g_s = 55\text{mm}$

the simulated lower frequency edge is found out to be 1.36 GHz compared to 1.1GHz calculated using the closed form equation.

Next, optimisations on the CPW feeding line were carried out to improve the bandwidth of the antenna. For this purpose, an elliptically tapered CPW feed was used to provide smooth transition of the impedance of the antenna between the feeding line and the radiating patch as shown in Figure 3.22. The parameter g_s was varied to investigate its effect on the bandwidth of the antenna. It can be seen that the widest bandwidth was achieved when g_s is 35mm. The simulated optimal operating frequency of the final elliptical monopole antenna as shown in Figure 3.23 is 1.36GHz to 2.31GHz which gives a total bandwidth of 0.95GHz. The optimised frequency range is within the recommended operating frequency range for microwave head imaging systems. The final design of the elliptical monopole antenna is illustrated in Figure 3.24. Table 3.4 shows the final antenna parameters for the elliptical monopole antenna.

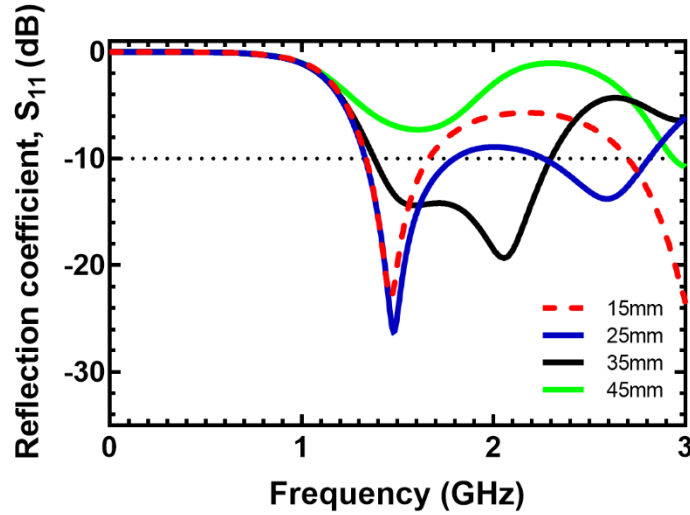
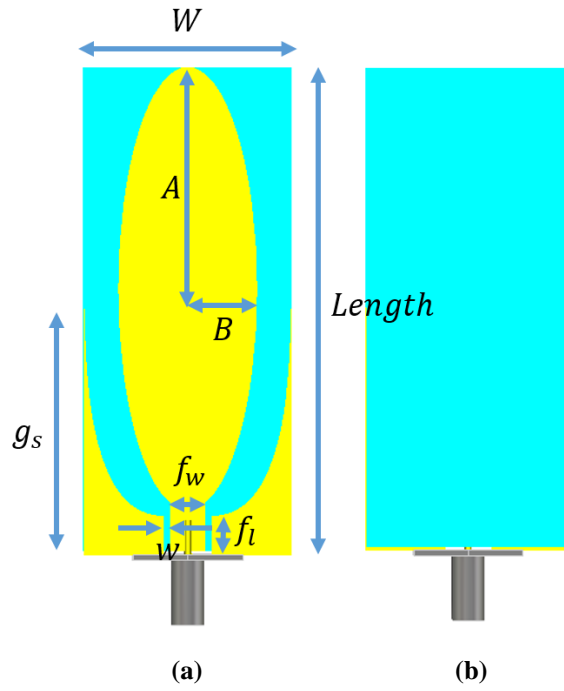


Figure 3.23: Reflection coefficients for parameter sweep for g_s from 15mm to 45mm



**Figure 3.24: Geometry of the wideband elliptical monopole antenna (a) Top view
(b) Bottom view**

Table 3.4

GEOMETRIC PARAMETERS OF THE ELLIPTICAL MONOPOLE ANTENNA

Antenna Dimensional Parameters	Symbol	Value (mm)
Antenna length	$Length$	70
Antenna width	W	30
Major axis	A	32
Minor axis	B	10
Thickness of the substrate	h_s	6
CPW gap	w	1
CPW feed-line width	f_w	5
CPW feed-line length	f_l	10
CPW ground length	g_s	35

3.2.2.3.1 Simulated Radiation Pattern of the Elliptical Shaped Monopole Antenna

Figure 3.25 demonstrates the simulated 2-D radiation patterns of the textile-based elliptical monopole antenna at 1.5GHz. It can be observed that the radiation patterns are nearly omni-directional in the H-plane whereas for E-plane, the antenna exhibits bi-directional pattern. 3-D radiations patterns of the antenna at three frequencies within the operating frequency are depicted in Figure 3.26. Compared to the previous trapezoidal shaped monopole design, stable radiation patterns are observed across the frequencies where there is no significant change on the antenna main lobe's direction. The simulated gain at the boresight of the antenna is given in Figure 3.27. It is seen that a consistent gain of 2dBi is achieved throughout the operating frequencies. This characteristic is advantageous for the imaging purpose.

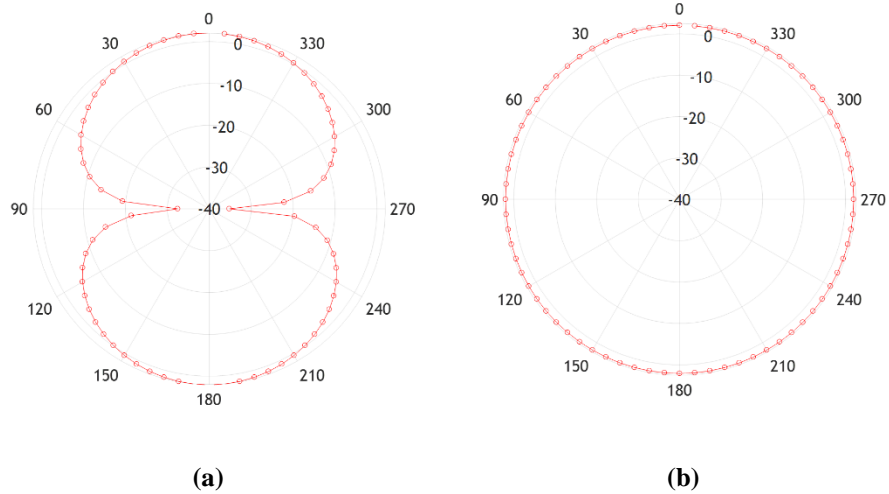


Figure 3.25: Simulated E-(XZ) and H-(XY) plane 2-D far-field radiation patterns at 1.5GHz for the elliptical monopole antenna on felt substrate

3.2.2.3.2 Time-domain Characterisation of the Elliptical Shaped Monopole Antenna

The computed time-domain responses received by the probes surrounding the elliptical monopole antenna are shown in Figure 3.28. For this antenna design, high fidelity factors of more than 0.94 are again observed at H-plane as tabulated in Table

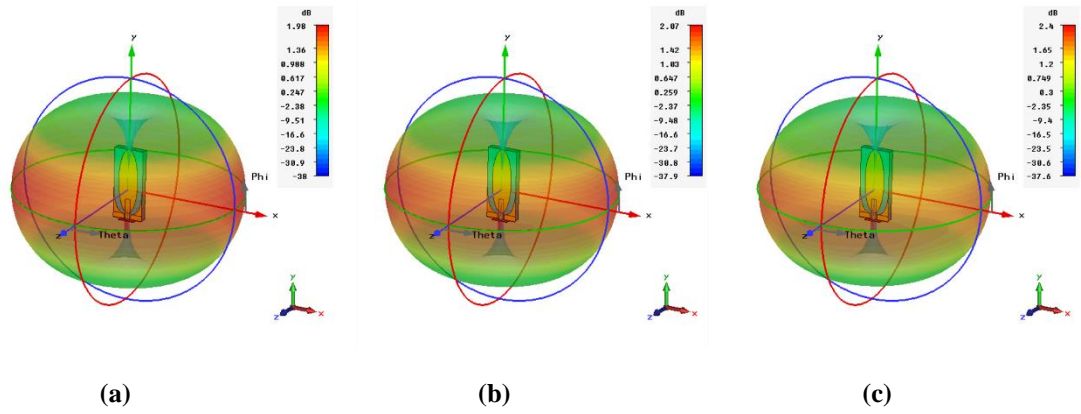


Figure 3.26: Simulated 3-D radiation patterns of the elliptical monopole antenna at (a) 1.5GHz (b) 2GHz (c) 2.5GHz and (d) 3GHz

3.5. This shows that the antenna will be able to radiate a pulse with minimal distortion which is important for the head imaging applications.

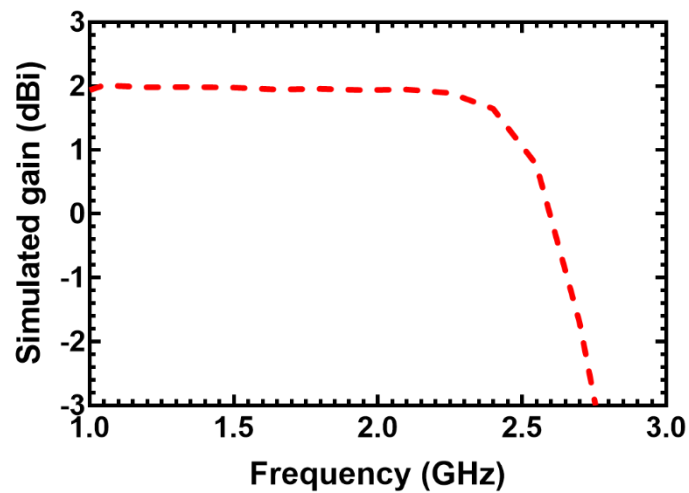


Figure 3.27: Simulated gain of the elliptical shaped monopole antenna

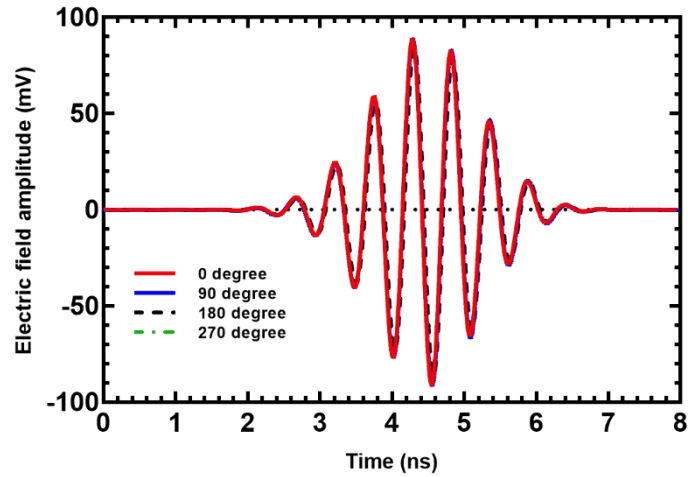


Figure 3.28: Simulated received near-field time-domain pulses radiated by the antenna in different angles without head phantom in H-plane

Table 3.5

FIDELITY FACTORS OF THE ELLIPTICAL MONOPOLE ANTENNA

Angle (degree)	Fidelity Factor
0°	0.98
90°	0.97
180°	0.96
270°	0.96

3.2.3 Performance Evaluation of the Proposed Antennas In-Close Proximity to a Human Head Phantom

Another challenge that is often encountered by sensing antennas in microwave medical imaging is the detuning and deterioration of the antennas' performance when placed in-contact or near the human body. For microwave head imaging, the sensing antenna needs to be placed closely to the head or in some cases direct contact is required so that most of the energy transmitted is focused towards the head. Therefore, an efficient antenna design must takes into consideration the effects of the lossy human

body on the characteristic of the antennas. As such, it is vital in the antenna design process to investigate the effects of the presence of the human head on the antenna performance in terms of impedance matching and to make necessary optimisation to obtain optimal performance. In addition, the effects of bending on the reflection coefficient and the radiation pattern of the antennas are also investigated since the antennas will be slightly bent to follow the shape of an artificial head phantom in an array configuration.

3.2.3.1 Inverted Trapezoidal Shaped Monopole Antenna

Figure 3.29 shows the configuration of the PET based antenna when bent to conform to the shape of a specific anthropomorphic mannequin (SAM) head phantom in the CST Microwave Studio. A 6mm separation between the antenna and the head phantom was specified in the simulation. In the actual experiments, this separation is provided by the use of felt material which acts as a spacer between the antenna and the head. The S_{11} result of the antenna is shown in Figure 3.30. It is seen that the S_{11} responses differ between the two cases where the impedance matching of the antenna deteriorates across the frequency range of 1.8GHz to 3.3GHz when the antenna is placed on the head phantom. However, the impedance matching is still below -10dB which indicates that the antenna's performance is still acceptable. The lower operating frequency edge of the antenna does not change whereas the upper frequency range increases from 3.5GHz to 4GHz. This results in increase of the impedance bandwidth of the antenna from 2.2GHz to 2.7GHz when operates in presence of the head

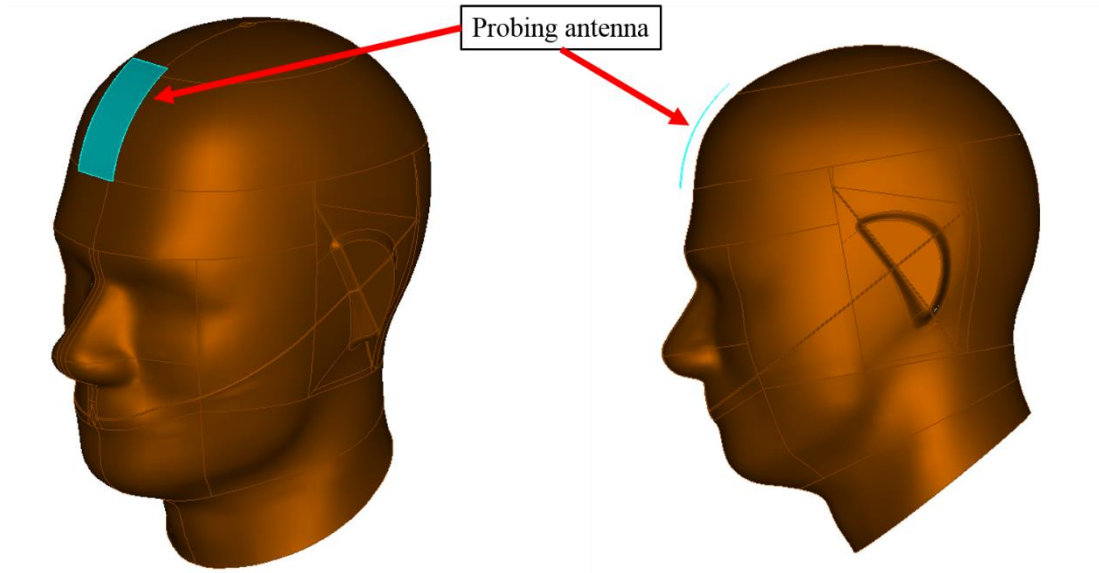


Figure 3.29: Antenna placement on the SAM head phantom in the simulation

phantom. The simulation results confirm that the antenna's impedance matching is still below -10 dB when operating in close proximity of the head phantom. As a result, no further optimisations on the antenna design was required.

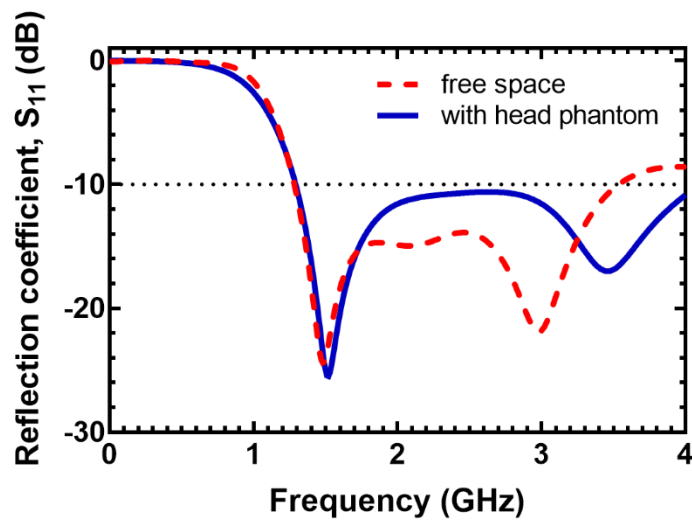


Figure 3.30: Simulated reflection coefficient of the trapezoidal monopole antenna on free space and with the presence of head phantom

For microwave imaging systems, the regions of where the antenna operates depend on the antenna size, its operating frequency range and the permittivity of the imaged body parts [65]. For the proposed antennas that were designed to operate mostly within the frequency range of 1.5GHz to 3GHz, the near-field region, r extends from 31cm (1.5GHz) to 62cm (3GHz) calculated using equation (3.10) [91]

$$r < \frac{2D^2}{\lambda_m} \quad (3.10)$$

where the average permittivity of the head phantom is assumed to be 40. λ_m is the operating wavelength in the medium and D is the largest dimension of the antenna. For both of the antenna designs, the largest dimension of the antennas is 70mm. Since the size of average human head is less than the calculated near-field range, this confirms that the antennas mainly operate within the near-field region in the microwave head imaging.

To further validate that the performance of the antenna is intact when operating in close proximity to the human head, time-domain characterisation was carried out by radiating a pulse into the head. A field probe was placed inside the head at 0° from the boresight direction of the antenna at a distance of 50mm from the centre of the antenna as illustrated in Figure 3.31 to calculate the field strength and shape of the pulse when the signal propagates from the antenna towards the head. Figure 3.32 shows the comparison of the received transmitted pulses with and without the head phantom. It

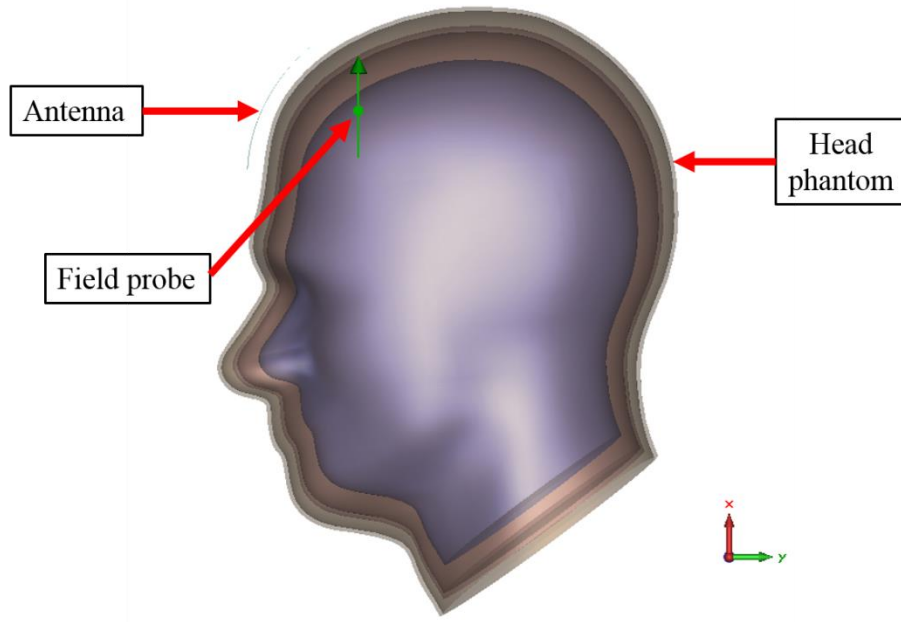


Figure 3.31: Placement of the field probe inside the head phantom

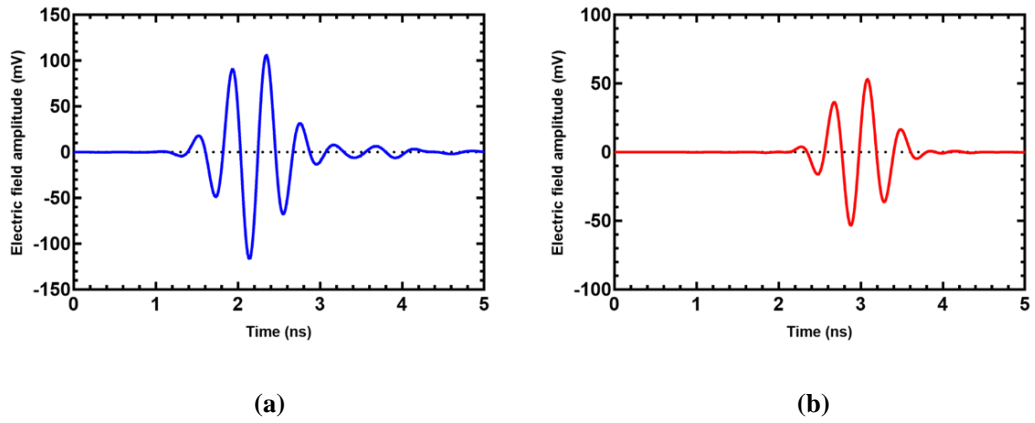


Figure 3.32: Simulated received near-field time-domain pulses radiated by the trapezoidal shaped antenna at 0° (a) without the head phantom and (b) with the head phantom in H-plane

can be seen that the amplitude of the pulse is reduced when the head phantom is present by a factor of 2 confirming that the head phantom consists of several layers of lossy biological tissues that greatly weaken the strength of the transmitted EM wave. In addition, a noticeable delay of the pulse received at the 0° probe for the case with head phantom is due to the reduction of the EM wave velocity when travelling through a high permittivity medium. In terms of the pulse integrity, the fidelity factor of the received pulse inside the head phantom was calculated using Equation (3.7). A fidelity

factor of 0.92 is achieved confirming that the pulse radiates with minimal distortion in presence of the head phantom. Another important observation that can be made is that the width of the transmitted Gaussian pulses inside the head phantom is slightly longer than that of free space that demonstrates pulse spreading occurs when the signal propagates inside the lossy and dispersive head phantom.

3.2.3.2 Elliptical Shaped Monopole Antenna

For the second antenna design, the same bending configuration was applied to the antenna as illustrated in Figure 3.29. Two scenarios were investigated. The first scenario is where an electric field probe was placed without the presence of the head phantom model. For the second scenario, the head phantom model was included in the simulation where the probe at 0° was now inside the head model. It is to be noted that the locations of the probes were in the radiating near-field region of the antenna for both cases. The amplitude and delay of the transmitted time domain Gaussian pulse containing the frequency spectrum of the antenna were compared to investigate the effects of the head phantom on the antenna performance. The computed time-domain response received by the probe at 0° the antenna are shown in Figure 3.33. The same result was obtained with regards to the reduction of the strength of the received pulse inside the head by around one half of the initial value. A small delay of the received pulse with the head phantom compared to the free space case can be attributed to the slowing down of the propagated EM wave inside the high permittivity head phantom.

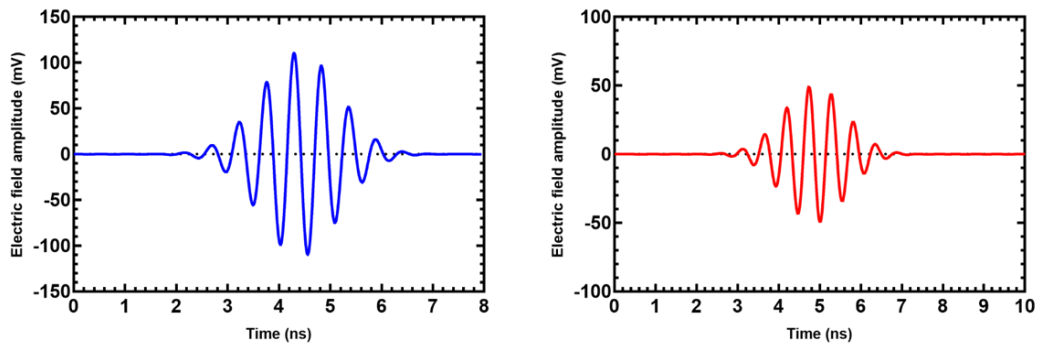


Figure 3.33: Simulated received near-field time-domain pulses radiated by the elliptical shaped antenna at 0° (a) without head phantom and (b) with the head phantom in H-plane

3.2.4 Fabrication and Measurement Results

In order to validate the performance and the characteristics of the proposed antenna, the antennas were prototyped as demonstrated in Figure 3.34. There are two monopole antenna designs that have been developed in this thesis which are trapezoidal and elliptical shaped monopole antennas. In the first design, two prototypes have been fabricated using both FR-4 and PET materials as the antenna substrate with thickness of 0.2mm and 100 μ m respectively. Although FR-4 material has been known for its rigid structure, the use of a thin FR-4 substrate makes it possible for bending or conformal configuration. The antenna on FR-4 substrate was fabricated using photolithography technique whereas for PET-based trapezoidal antenna, conductive inkjet printing technique was utilised. The polymer based PET material is used to further improve the flexibility of the proposed antenna as well as for weight reduction. For the third prototype, textile materials namely conductive textile sheet, Shieldex® Zell and felt were used for the fabrication of the elliptical monopole antenna. The reported measured conductivity of the fabric is 1.29×10^4 S/m at 2GHz [92]. The

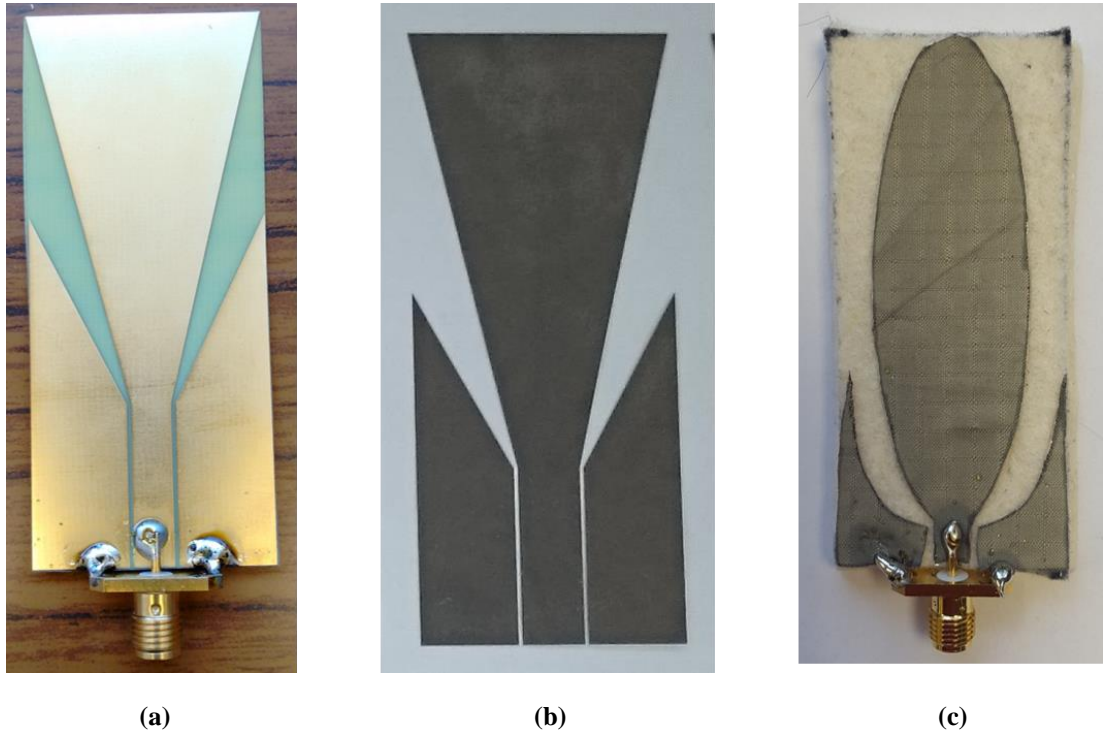


Figure 3.34: Fabricated flexible antenna elements (a) Trapezoidal monopole antenna on FR-4 (b) Trapezoidal monopole antenna on PET and (c) Textile based elliptical monopole antenna

measured permittivity, ϵ_r and the loss tangent, $\tan \delta$ of the felt are 1.55 and 0.068 obtained using a dielectric probe. The fabrication of the fully textile antenna was carried out using manual cutting tools. To fasten the conductive sheet onto the felt substrate, an ironing process was carried out to activate the heat-activated adhesive on the reverse side of the conductive fabric. The fully textile based antenna can be integrated seamlessly into a patient's head garments for wearable applications. All antenna prototypes were measured and their reflection coefficient were compared to the simulation results for validations.

3.2.4.1 Trapezoidal Shaped Monopole Antenna on 0.2mm Thick FR-4 Substrate

In this subsection, the S_{11} characteristic of the antenna was first measured in free-space and the results were compared to the simulated one. Due to the specification of the VNA used in this research, the measured frequency range was limited to 3GHz. By using a realistically shaped artificial head phantom developed in Chapter 6, the impedance matching of the antenna was also measured when in close-proximity to the head phantom. To provide ample separation between the antenna and the head phantom, felt material was used to act as a spacer as shown in Figure 3.35. Moreover, the integration of felt on the antenna structure facilitates a firm and comfortable contact of the antenna on the human head. The thickness of the felt is 6mm. It is to be noted that the use of the felt to cover the antenna does not affect the antenna's performance due to its low permittivity comparable to air and has low tangential loss as measured using a dielectric probe. The measured reflection coefficient of the antenna is illustrated in Figure 3.36 for all cases. The results show good agreement between the simulation and the experiment in terms of the impedance bandwidth of the antenna. However, S_{11} responses are not identical due to several factors such as fabrication errors and slight differences of the electrical properties of the head phantom used in the simulation and the fabricated phantom.



Figure 3.35: Photograph of the single prototype antenna (inset picture) covered with felt material

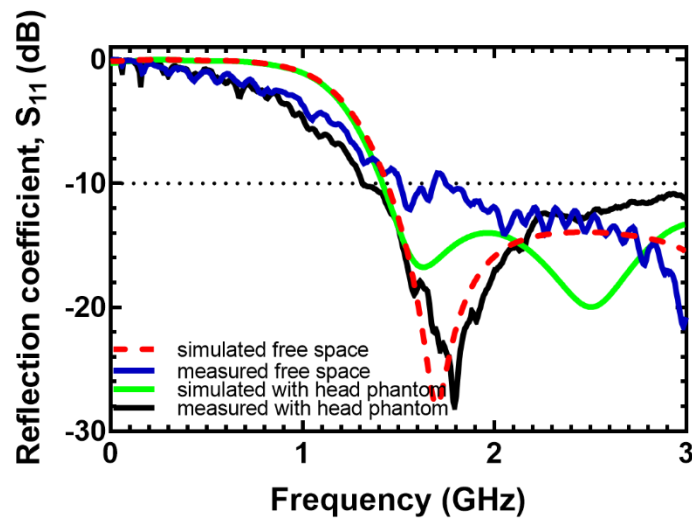


Figure 3.36: Reflection coefficients of the trapezoidal monopole antenna on FR-4

3.2.4.2 Trapezoidal Monopole Antenna on PET Substrate

The measurement was carried out on the second antenna prototype which utilised PET material which is able to provide more flexibility compared to the previous FR-4 material. The same measurement process was carried out and the measured results

were compared to the simulation results for validation. It has been found that the impedance bandwidth of the prototype antenna when placed on the artificial head phantom is increased since the lower frequency edge shifts to 1GHz as shown in Figure 3.37 while in the simulation it is at 1.3GHz. The measured result shows that the antenna manages to maintain its performance even when placed in close-proximity to the head phantom where the impedance matching of the intended operating frequency range from 1.5GHz to 3GHz is below -10dB based on the measured S_{11} response.

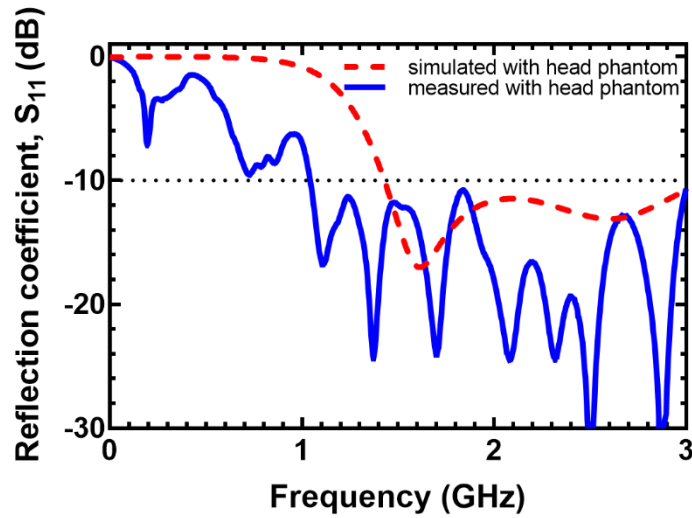


Figure 3.37: Reflection coefficients of trapezoidal monopole antenna on PET substrate

3.2.4.3 Elliptical Monopole Antenna on Felt Substrate using Conductive Textile

For the last prototype, the fully textile based antenna is designed with the aim to provide better integration of the antenna with clothing suitable for wearable head monitoring systems. The utilisation of textile materials is to improve the comfort of the wearer in comparison to other materials. Moreover, the proposed antenna can be embedded in clothing items for realisation of wearable head monitoring systems. Figure 3.38 depicts the measured reflection coefficient of the antenna in comparison with the simulated results for both in free space and on the artificial head phantom. The measured S_{11} signals for both cases demonstrates noticeable increase in the

impedance bandwidth of the antenna compared to the simulation results. It is seen that the impedance bandwidth of the textile antenna in presence of the head phantom is from 1.26GHz to 2.76GHz increases by 480MHz compared to the simulation result. Again, for the final prototype, the performance of the antenna does not deteriorate when measured on the artificial head phantom suggesting that the antenna has been optimised for use as sensing antenna in the wearable head imaging system. Moreover, the increase in measured bandwidth of the antenna is beneficial to the overall performance of the imaging system.

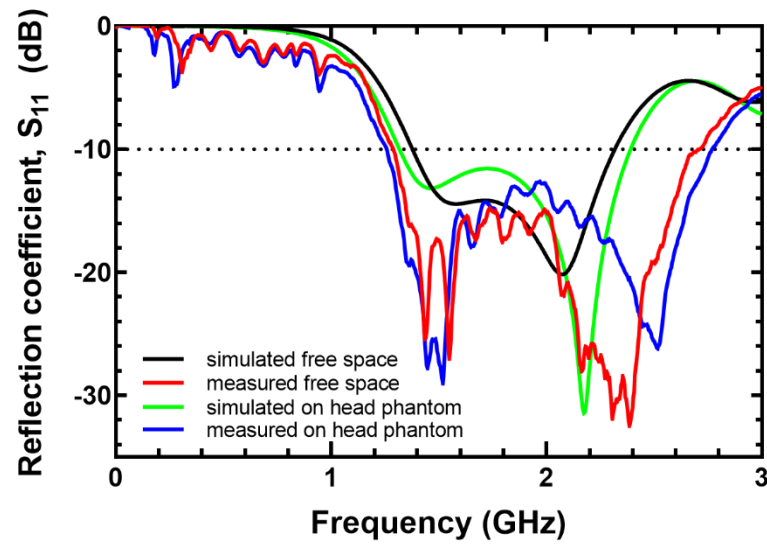


Figure 3.38: Reflection coefficients of textile elliptical antenna on free space and artificial head phantom

3.3 Summary

This chapter discussed the development of the antennas for wearable microwave head imaging applications. The antennas have been developed based on several main requirements mainly flexibility, lightweight, wideband and compactness. The proposed antennas are mainly based on planar monopole configuration to provide low-profile characteristic where the antennas can be fitted into an array to be mounted on the human head. These antennas can be categorised into two main designs based on

their shapes. The first antenna design is an inverted trapezoidal shaped monopole antenna. This antenna design has been further modified and optimised for fabrication on two different substrates which are FR-4 and PET. Both prototypes show similar performance in terms of impedance bandwidth and radiation patterns. For the second design, elliptical shaped radiating element is utilised using all textile materials. The conducting element of the antenna is made of conductive textile sheet whereas the antenna substrate is made of felt fabric. The S_{11} responses of the antennas were measured and compared with the simulation results. A good agreement has been obtained in terms of impedance bandwidth for all the antenna prototypes.

Chapter 4: Wearable Prototypes for Microwave Head Imaging

In this chapter, prototypes of wearable devices made from arrays of flexible antenna elements designed in the previous chapter are developed. For wearable applications, array configuration is the best solution where it can eliminate the need for mechanical instrument such as rotating platform to support the sensing device hence making it compact and lightweight [5], [16], [93]. However, there are several limitations and challenges that have to be addressed when designing an antenna array for microwave head imaging applications. One of the challenges is the total number of antennas that can be used in the array is limited to the space available depending on the antenna size and the human head while making sure sufficient antennas are utilised to probe the head for the detection of a stroke or intracranial bleeding inside the head. Moreover, the mutual coupling between adjacent antennas may pose a challenge in detecting weak reflected signals that may come from the stroke target. As such, a trade-off needs to be made to ensure all areas of the brain are probed by the sensing antennas while reducing the effect of coupling between adjacent antennas by keeping enough distance between them. The initial prototype uses an elliptical-shaped wearable base structure made of flexible conductive sheet and lossy dielectric absorber to hold the antennas in place. For the final prototype, a strap-based wearable head device is developed where the device can be worn like a head band. These prototypes serve as proof-of-concept wearable devices for microwave head imaging applications to further improve the current method of static microwave head imaging which can facilitate a frequent monitoring of patient's health as well as for real-time monitoring of a person's head condition.

4.1 Antenna Array with Flexible Metal Backed Lossy Dielectric Absorber

For wearable head imaging application, an elliptical array configuration is employed in this research where the sensing antennas are arranged around the human head. To realise this, the antenna array needs to be mounted on the head and to be firmly held on that position when measurements are taken. Therefore, a hat-like structure is devised and developed as a mounting base for the array where the antennas can be accommodated.

It has been reported in [94] that the performance of sensing antennas for microwave biomedical imaging can be improved by utilising directional antennas. The radiation beams of such antennas can be focused on the area of the body to be probed while suppressing the radiations coming from other directions. The radiation pattern of the proposed monopole antenna has nearly omni-directional radiation. The back lobe radiation of the antenna may mask any reflected signals that come from the stroke due to their weak signals. In [95], a metal backed dielectric absorber has been used to improve the directionality of a spiral antenna. It is also been reported in [96] that by using a metal reflector at a distance of more than 1cm from a monopole antenna, the propagated EM wave inside the breast could be increased without any deterioration of the S_{11} of the sensing antenna. In addition, an UWB monopole antenna with a reflector was presented in [97] for breast microwave imaging. Due to the use of the reflector at a distance of 6.58mm, a slight deterioration of the impedance matching of the antenna was observed. However, the directionality of the antenna was improved compared to without using the reflector.

Theoretically, a reflector should be placed at a distance of $\lambda/4$ from the antenna where λ is the wavelength of the lowest frequency edge of the antenna in free space to increase its directivity where the reflected wave will combine coherently with the forward travelling wave. At 1.5GHz, the calculated quarter wavelength of the EM

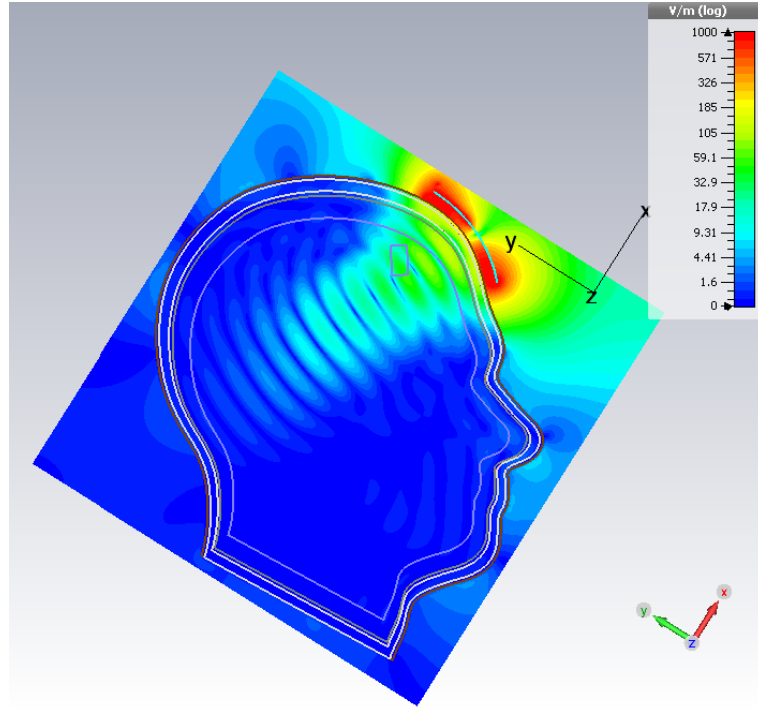


Figure 4.1: Simulated E-field distribution inside the head phantom at 1.5GHz

wave in free-space is about 50mm. However, based on the simulation conducted as illustrated in Figure 4.1, when the antenna was in close proximity to the human head, strong coupling could be observed between the antenna and the head tissues. By varying the distance of the reflector from the antenna with the presence of human head, a shorter distance than quarter wavelength is possible to improve the directivity of the antenna without sacrificing the impedance matching performance of the antenna. Thus, a simulation of the probing antenna with a reflector as shown in Figure 4.2 was carried out. Figure 4.3 demonstrates the reflection coefficients at various distances of the reflector from the antenna. It is found that a minimum separation of 25mm between the reflector and the probing antenna is required to maintain the impedance bandwidth of the antenna. The penetration of the EM wave inside the head phantom with the utilisation of the reflector is depicted in Figure 4.4. It is observed that the signal penetration inside the head is improved compared to without using the reflector.

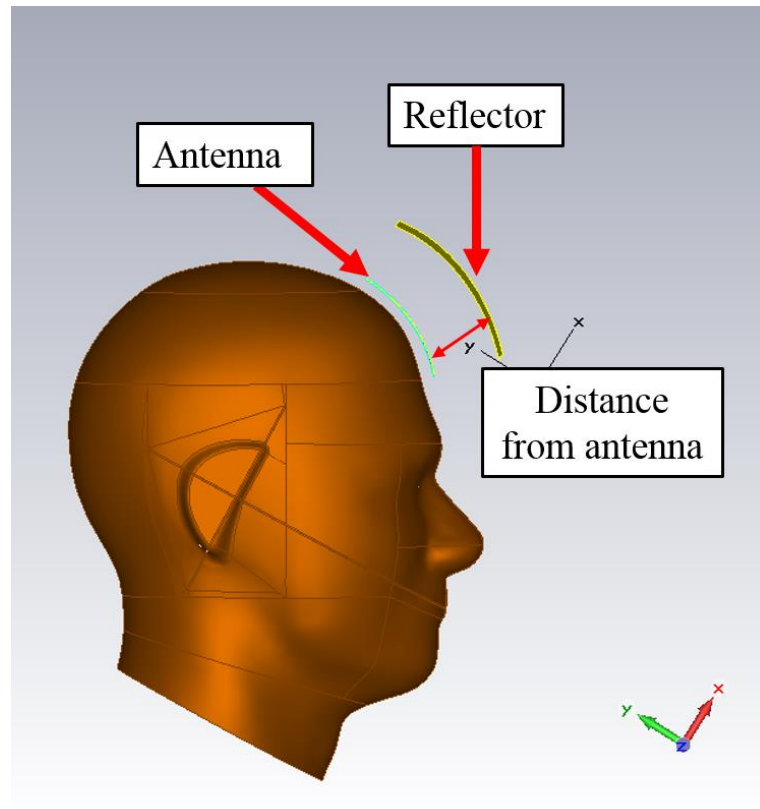


Figure 4.2: Position of the reflector to suppress the back lobe radiation for improved antenna directivity

Based on the finding from the simulations that allows the placement of a reflector much closer to the probing antenna due to the strong coupling between the head and the antenna, the use of flexible conductive sheet was considered as a reflector to suppress any unwanted radiations from the surroundings. To facilitate the placement of the reflector sheet away from the antenna, a base structure is required. The proposed base structure is aimed to act as a wearable item similar to a function of a head garments such as hats where additionally it can also accommodate the sensing antennas and the switching circuit.

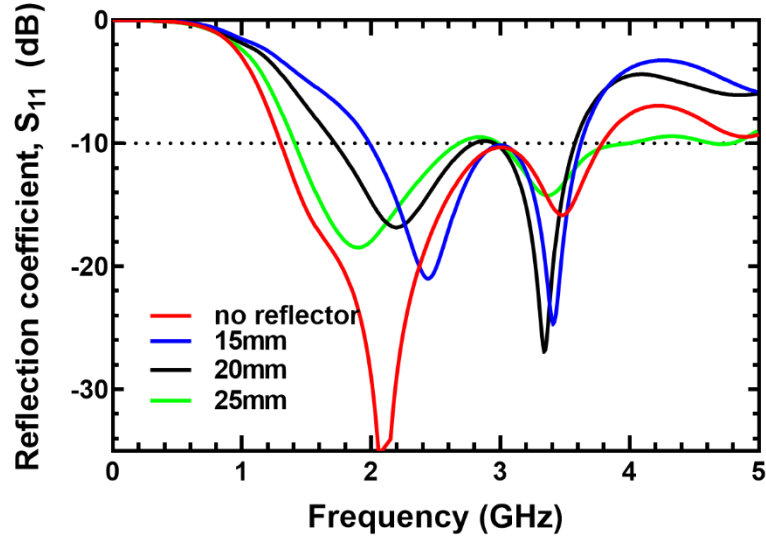


Figure 4.3: Refection coefficients of the antenna for various distance separations between the antenna and the reflector

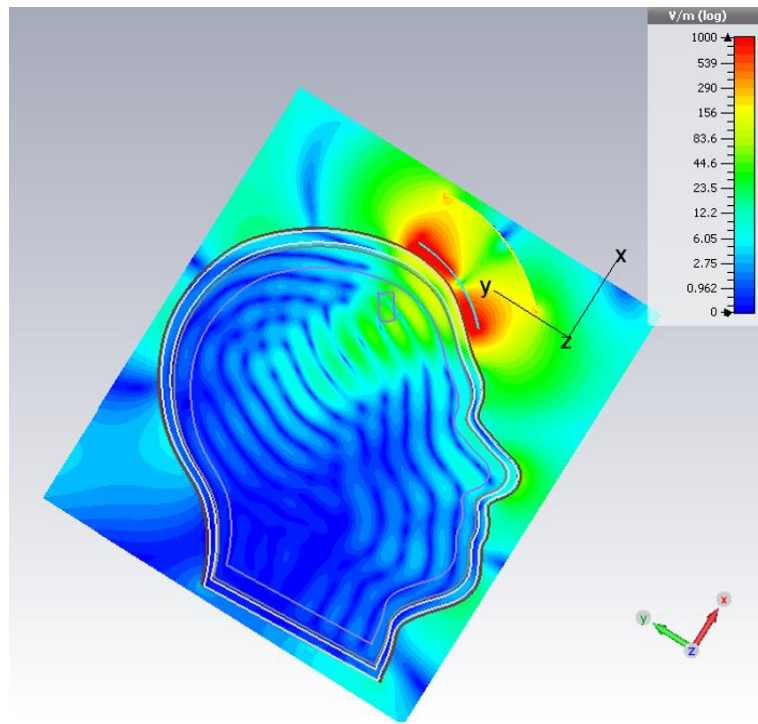


Figure 4.4: Simulated E-field distribution inside the head with the use of reflector

In [98], it has been demonstrated that to increase the directionality of a parabolic antenna, a short metallic shield can be placed around the antenna. However, the reflections coming from the shield affected the performance of the antenna. To

mitigate this issue, an absorbing material was suggested to eliminate any reflections from the utilisation of the metallic shield where the absorbing material was fit on the inside of the shield. Therefore, an absorbing material, a flexible dielectric absorber, AN70 from Emerson & Cuming covered with the flexible conductive sheet was explored and utilised in this prototype to suppress the back lobe radiation of the probing antennas. The thickness of the absorber is 19mm. With the use of felt to cover the antenna, it provides additional separation between the antenna and the flexible conductive sheet. The final separation between the antenna and the conductive sheet is 25mm. This corresponds to one eighth of the free-space wavelength at 1.5GHz. It is noted that due to the strong coupling of the EM wave between the antenna and the head, a minimum separation of only 25mm is permitted with no degradation on the impedance matching of the antenna as explained earlier.

The absorber was cut and shaped to conform to a commercially available skull phantom [99]. The general shape of the final structure of the absorber base is elliptical as shown in Figure 4.5. A hook and strap was used to attach the antennas to the base as shown in Figure 4.6. To evaluate the effectiveness of implementing flexible EM absorber on the antenna array, time-domain characterisation was conducted in the EM

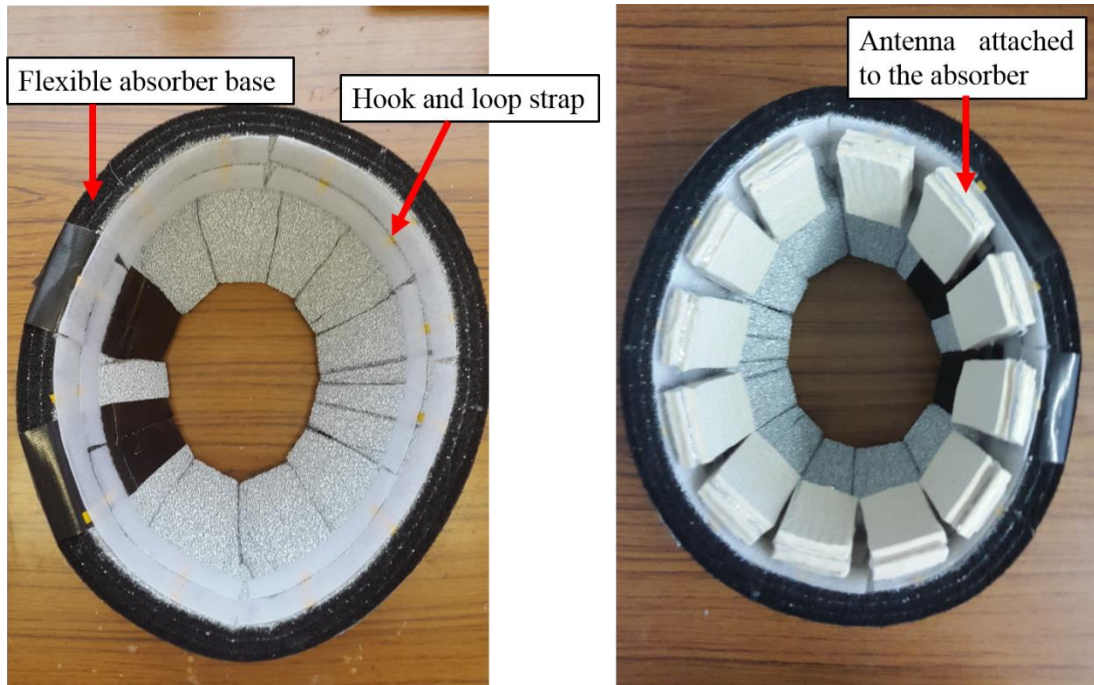


Figure 4.5: Flexible absorber shaped as a base for the flexible antennas

Chapter 4: Wearable Prototypes for Microwave Head Imaging

solver where the E-field strengths at various locations around the antenna with and without a head phantom were calculated. By observing the received E-field strengths in Figure 4.7 and Figure 4.8, the effect of using a flexible absorber backed with a reflector to suppress the back lobe radiation of the antenna can be seen by the significant reduction of the amplitude of the pulse at 180° angle as compared to the one without the reflector backed absorber. By using the received time-domain electrical signal's amplitudes, the calculated front-to-back ratio of the signal is found to be around 11.5:1 which shows improvement on the antenna directivity.



Figure 4.6: Prototype of the antenna array for trapezoidal monopole antenna on FR-4 covered with felt on the top and bottom of the antennas

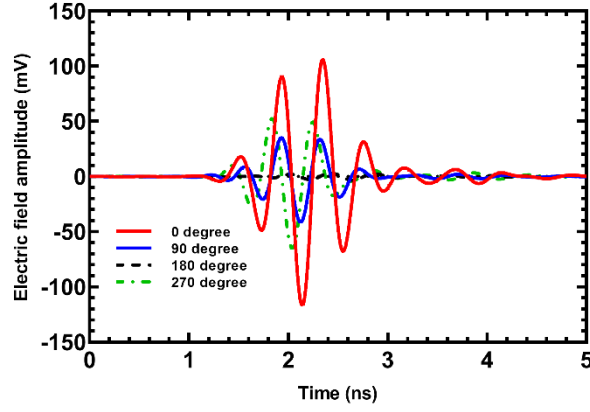


Figure 4.7: E-field strength of the transmitted Gaussian pulse with the use of flexible absorber without head phantom

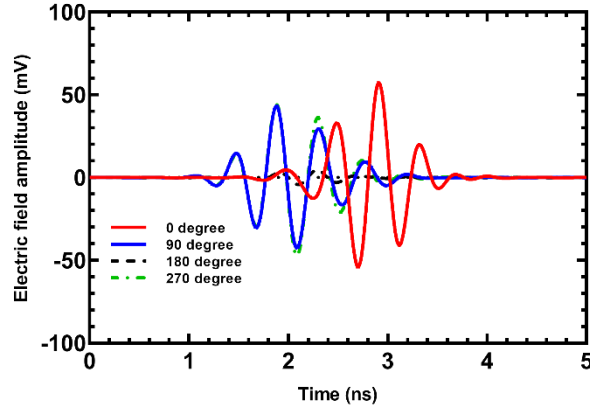


Figure 4.8: Figure 38 E-field strength of the transmitted Gaussian pulse with the use of flexible absorber with head phantom

4.1.1 Development of 12 Elements Antenna Array on Conductive Sheet Backed Flexible Absorber

To provide enough coverage to probe the human head, 12 antenna elements have been prototyped as shown in Figure 4.6. Full-wave simulations have been carried out to investigate the spatial penetration of the propagated electromagnetic waves into a head phantom from the wearable antennas by observing the radiation power density inside the head model from all the antenna elements. In addition, the attenuation of the

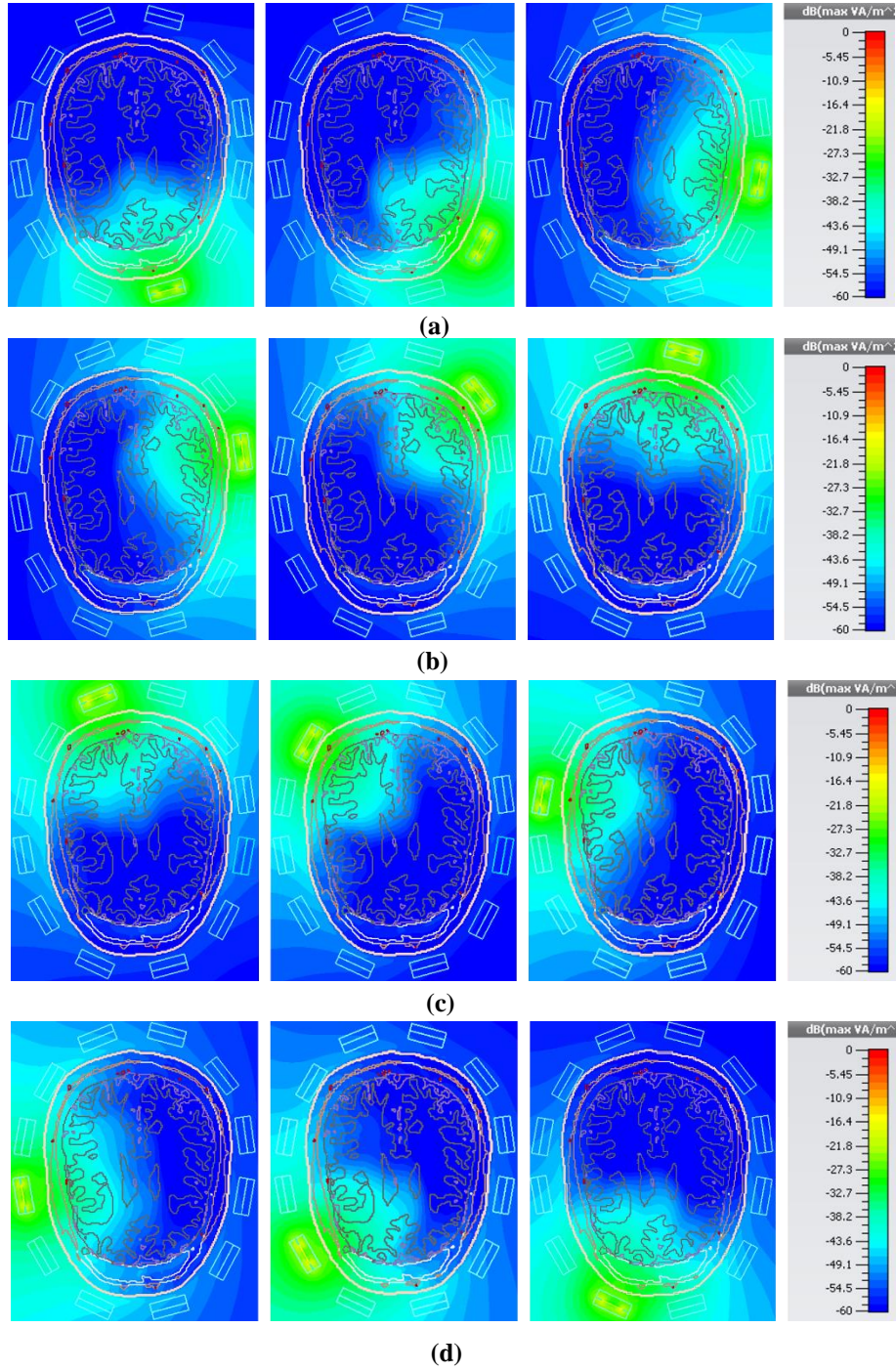


Figure 4.9: Simulated power density inside the head phantom for each antenna element in the array. (a) Antenna 1, Antenna 2 and Antenna 3. (b) Antenna 4, Antenna 5 and Antenna 6. (c) Antenna 7, Antenna 8 and Antenna 9. (d) Antenna 10, Antenna 11 and Antenna 12.

transmitted EM wave was calculated in order to estimate the power required for a pulse to make a round trip from the mono-static antennas to a stroke target. Moreover, the



Figure 4.10: Prototype of the wearable head imaging device for medical imaging applications

areas of the brain covered by the 12 antennas in the array were examined to ensure sufficient coverage was achieved for detection purpose. Although the minimum number of the antennas used for monostatic approach in wideband microwave head imaging reported in the literature was 16 [43], our 12 antenna array system is capable to detect a stroke target of size $25 \times 25 \times 25 \text{ mm}^3$ as will be discussed in the Chapter 7. Figure 4.9 shows the radiation power density at the cross section 40mm below the head crown when probed by the proposed array at 1.5GHz. It can be seen that there is enough penetration from the transmitted signal at the operating frequency of the proposed array for head imaging applications. Due to the antenna size and the circumference of average human head, further increment of the array size is very challenging which requires miniaturisation of the antenna. This will be conducted in the future.

4.1.2 Reflection Coefficients of the PET-Based Trapezoidal Monopole Antenna Array with Conductive Sheet Backed Flexible Dielectric Absorber

The impedance matching of the antenna array employed in the developed prototype as illustrated in Figure 4.10 was measured using a VNA. Figure 4.11 and Figure 4.12 show the S_{11} signals for all the antenna elements in the array for the trapezoidal shaped monopole antenna on PET substrate. It is seen that the highest

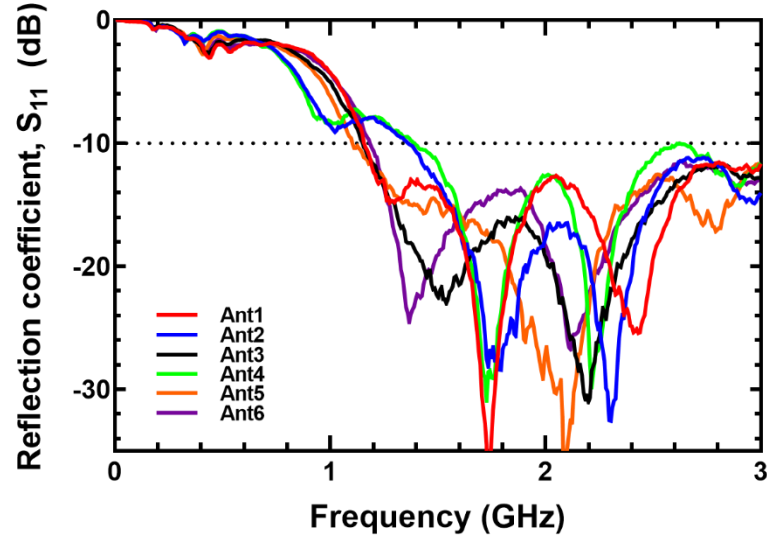


Figure 4.11: Measured S11 responses for Ant 1 to Ant 6 in the antenna array

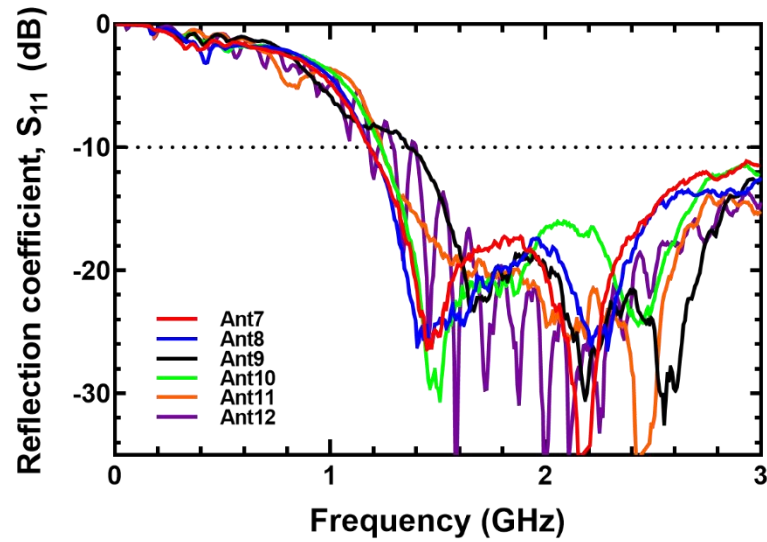


Figure 4.12: Measured S11 responses for Ant 7 to Ant 12 in the antenna array

measured lower frequency edge of the antennas is 1.5GHz for Ant4. On the other hand, the upper frequency edge of the antennas is more than 3GHz. However, due to the upper frequency limit of the VNA, the measurement was limited to only 3GHz. Moreover, it has been reported in the literature that higher frequency content does not able to provide sufficient penetration inside the lossy human head [37][6]. Therefore,

it is not the intention of the wearable imaging system to use frequency above 3GHz. As for the variation of the S_{11} signals among the antennas in the array, this can be due to the inconsistency in the fabrication process and the soldering effect of the SMA connectors.

4.1.3 Mutual-Coupling between Adjacent Antennas for Trapezoidal Shaped Monopole Antenna on PET Substrate

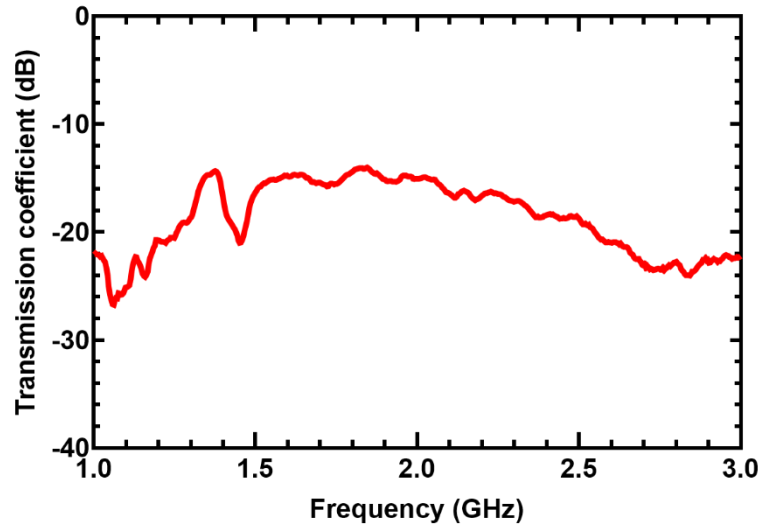


Figure 4.13: Mutual coupling between Ant1 and Ant2 in the PET based array

Another performance parameter that needs to be evaluated is the mutual coupling between the adjacent antennas in the array. One of the main requirements in developing an antenna array for biomedical imaging system is to reduce the effect of coupling between neighbouring antennas that can potentially decrease the antenna efficiency. The measured antenna coupling between Ant1 and Ant2 in the array is shown in Figure 4.13. The highest S_{21} value recorded across the operating frequency of the antenna is -14dB that shows low mutual coupling effects [100], [101]. It is expected that the low coupling effects will not jeopardise the performance of the imaging system.

4.2 Head Strap Antenna Array using 12 Antenna Elements

Although the use of flexible absorber is beneficial to suppress the back lobe radiation and to act as the mounting base for the prototype to hold the antennas, the prototype could only fit on one specific head size. In this work, an artificial head phantom was used as a reference when constructing the prototype. Therefore, to use the wearable prototype on different head size, the base must be redesigned to fit the new head shape. To mitigate this issue, a trade-off has been made by sacrificing the back lobe radiation suppression to facilitate the use of stretchable head strap structure to hold the antennas. This stretchable prototype serves as a proof-of-concept where the wearable device can be fitted on different head sizes without requiring additional modifications on the device. The new prototype is shown in Figure 4.14 where a head band is used to accommodate the flexible antennas. Compared to the previous prototype, the sensing antennas can now be firmly mounted on the head regardless of the head size. Moreover, the whole structure of the wearable device is more compact and less bulky in comparison to the previous prototype.



Figure 4.14: Flexible antennas integrated with a head band strapped on a head phantom

4.2.1 Reflection Coefficients of the Textile-Based Elliptical Monopole Antenna Array

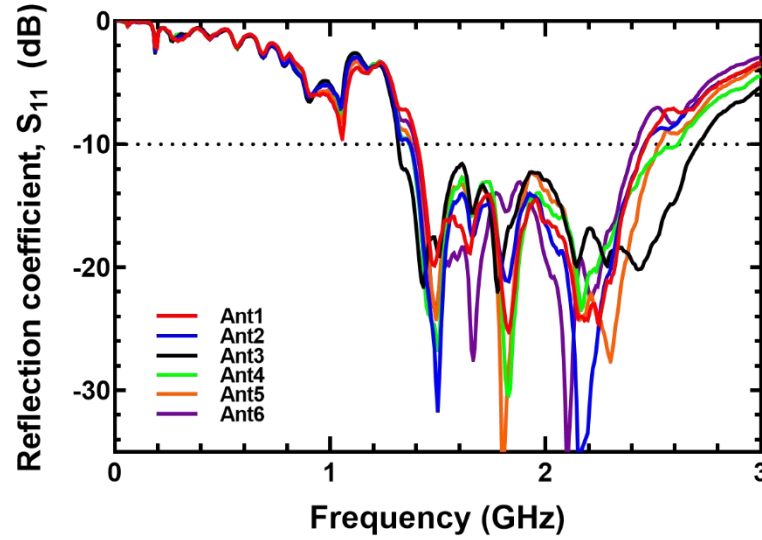


Figure 4.15: Measured S11 data for Ant 1 to Ant 6 in the textile based antenna array

The measured reflection coefficients of the antenna elements in the textile based prototype are demonstrated in Figure 4.15 and Figure 4.16. It is noted that the highest measured lower frequency edge of the proposed antennas is 1.4GHz for Ant7 while the lowest value recorded is 1.31GHz for Ant 3. In terms of impedance matching, the average measured bandwidth of the array is 1.18GHz. The wide impedance bandwidth obtained from the antennas is required for the proposed head imaging system. As for the variation of the S_{11} data among the antenna elements in the array, this due to the fabrication inconsistency and the soldering effect. It is noted that based on experience fabricating the antennas, identical S_{11} response between two antennas of the same design is almost impossible to achieve.

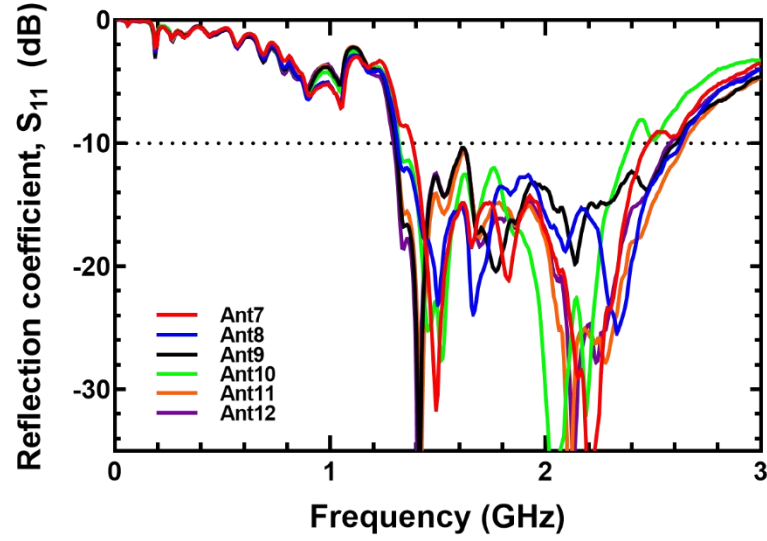


Figure 4.16: Measured S11 data for Ant 7 to Ant 12 in the textile based antenna array

4.2.2 Investigation on the Mutual-coupling between Adjacent Antennas for Elliptical Monopole Antenna Array

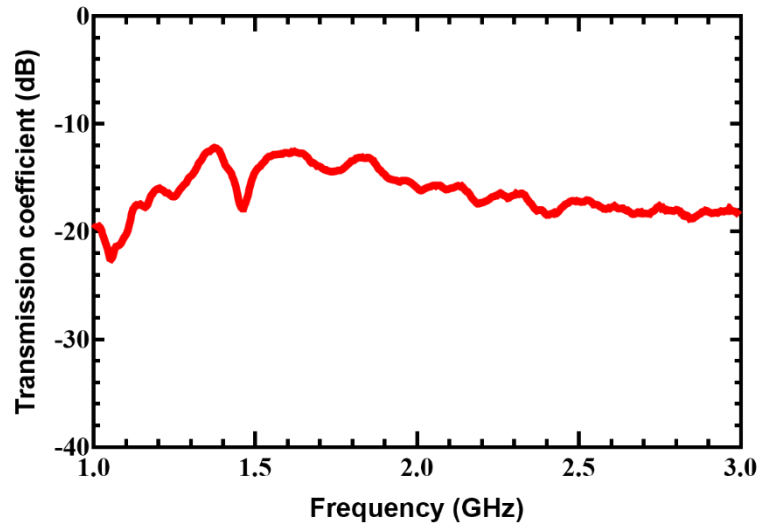


Figure 4.17: Measured mutual coupling between Ant 1 and Ant 2 in the textile based antenna array

To evaluate and analyse the effect of mutual coupling between the adjacent antennas for the textile antenna design, the transmission coefficient between two

adjacent antennas in the array namely Ant1 and Ant2 was measured as presented in Figure 4.17. It is seen that the highest S_{21} value for the antenna array is -12dB between Ant1 and Ant2 which indicates that reasonably low mutual coupling value. Based on this result, it is concluded that the distance between the antenna elements in the proposed array is sufficient to assure that the nearby antennas does not significantly interfere with the operating antenna. It is to be noted that during the scanning of the head phantom, only one antenna in the array is activated at a time while the remaining antennas are switched off.

4.3 Specific Absorption Rate and Maximum Allowed Transmitted Power

The safety requirement of the proposed wearable imaging device was investigated based on the specific absorption rate (SAR) values [102]–[104]. SAR is a measure of how electromagnetic wave is absorbed by human tissues. SAR is a function of electrical conductivity, σ (Siemens/meter), the received E-field from the radiated energy, E (Volts/meter), and the mass density of the tissue, ρ (kg/m³). The SAR can be calculated by averaging over a specific volume (typically measured over 1g or 10g of tissue) using Equation (4.1) below.

$$SAR = \frac{\sigma}{\rho} |E|^2 \quad (4.1)$$

The specific absorption rate (SAR) values were calculated at several frequencies within the operating frequency band of the antenna by varying the transmitted power from 1mW to 100mW to investigate the effects of the EM wave exposure to human head. The maximum limit of SAR imposed by the UK government is 2 W/kg for 10g of tissue mass. Therefore, this limit must be complied by the proposed wearable imaging system to ensure safe diagnosis [105]. Figure 4.18 shows the peak SAR values from 1.3GHz to 3GHz frequency band. The peak SAR values at frequency of 1.3GHz are 0.0038W/kg, 0.0383 W/kg and 0.3830 W/kg for transmitted power of 1mW, 10mW and 100mW respectively. The calculated SAR values are all below the regulated maximum limit indicating the feasibility of using the proposed antennas for wearable microwave head imaging systems. It can be seen that the EM wave absorbed

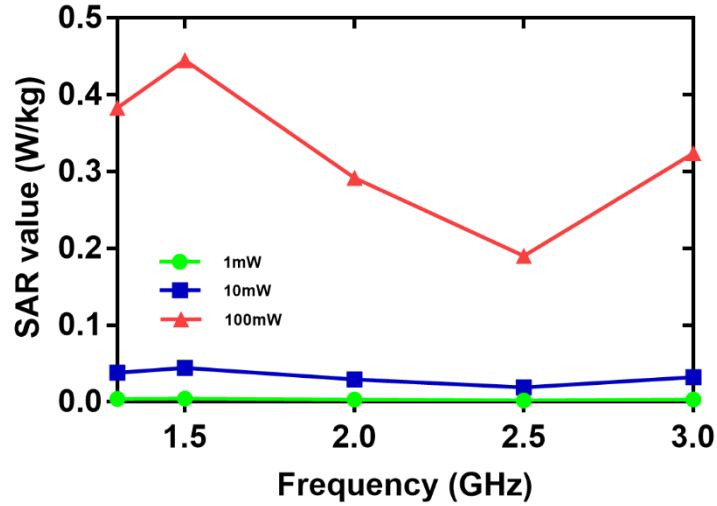


Figure 4.18: The simulated maximum SAR values over the operating frequency of the antenna

by the biological tissues increases linearly with the transmitted power. It is concluded that transmitted power of more than 100mW should be avoided to ensure safe operation of the imaging system. The spatial SAR distribution inside the head phantom at 1.5GHz at three different power levels are illustrated in Figure 4.19. Figure 4.19 demonstrates increase in power absorption by the head as the transmitted power of the antenna is increased. It is also observed that there is gradual reduction in power dissipation from the skin layer towards the middle section of the head since the propagated wave experiences more losses as it travels inside the head phantom across all transmitted power levels. To investigate the spatial SAR distribution across the operating frequency of the antenna, another simulation was carried out by transmitting 10dBm of power towards the artificial head phantom in the simulation.

Figure 4.20 shows the spatial SAR distribution at four frequencies namely 1.5GHz, 2GHz, 2.5GHz and 3GHz. It is seen that at 1.5GHz, the electromagnetic power absorption occurs at a deeper region of the head compared to other frequencies. Meanwhile, at 3GHz, the power loss is mainly localised at the outer layers of the head phantom. It can be concluded that low frequency microwave signal can penetrate deeper into the human head compared to higher frequency signal where most of the power is absorbed at the most outer layers of the head.

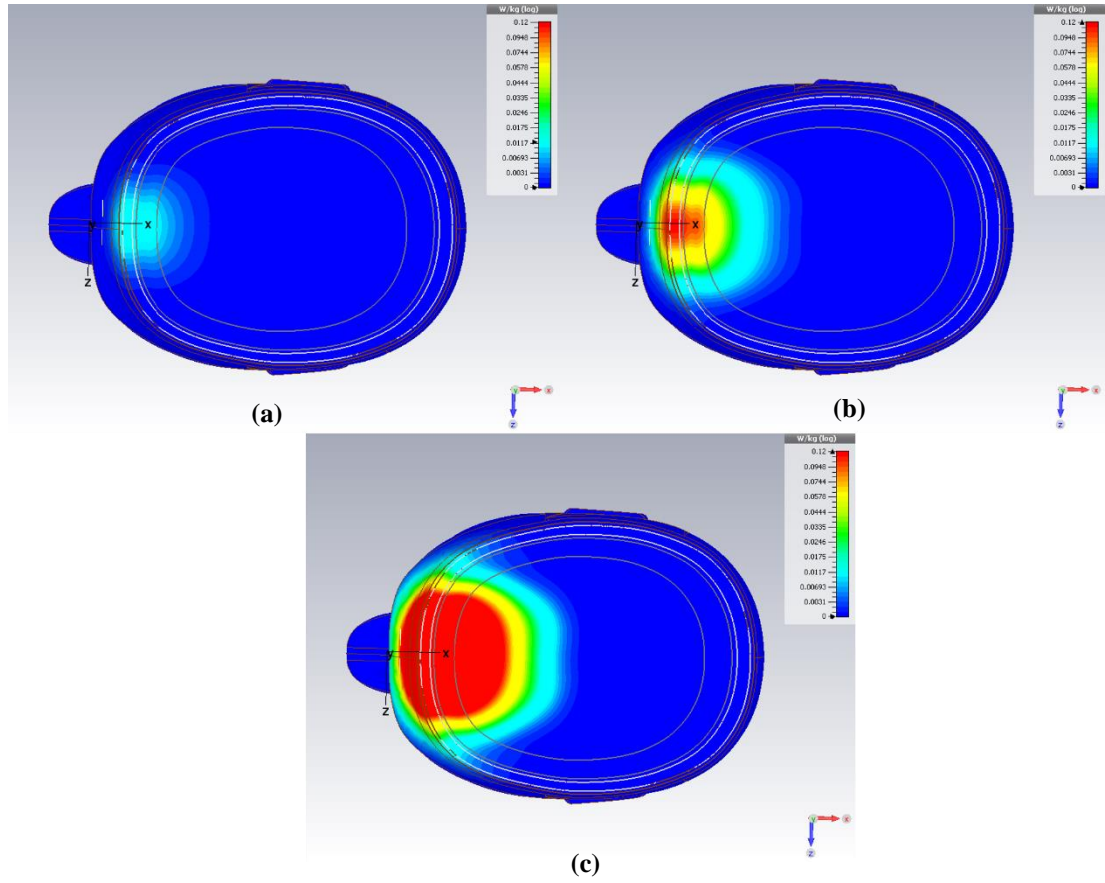


Figure 4.19: Simulated SAR distribution inside an artificial human head at 1.5GHz for (a) 1mW, (b) 10mW and (c) 100mW

The effects of radio wave signals exposure on human body have been an ongoing research topic. Several reports have been published that indicate microwave radiation might have biological effects on humans based on the tests carried out on rats [106]–[108]. However, the test in [108] were carried out with a SAR value of 0.6W/kg for 2 hours over 3 months on rats which is much more than the required power and time for the proposed system for stroke detection and monitoring applications. Moreover, it has been found in [109] that there was no evidence to support that microwave radiation could increase the risks of cancer in humans. In addition, the advantages of using the proposed system to detect and monitor stroke condition on patients far outweigh its potential side effect since the disease requires immediate attention to save their lives.

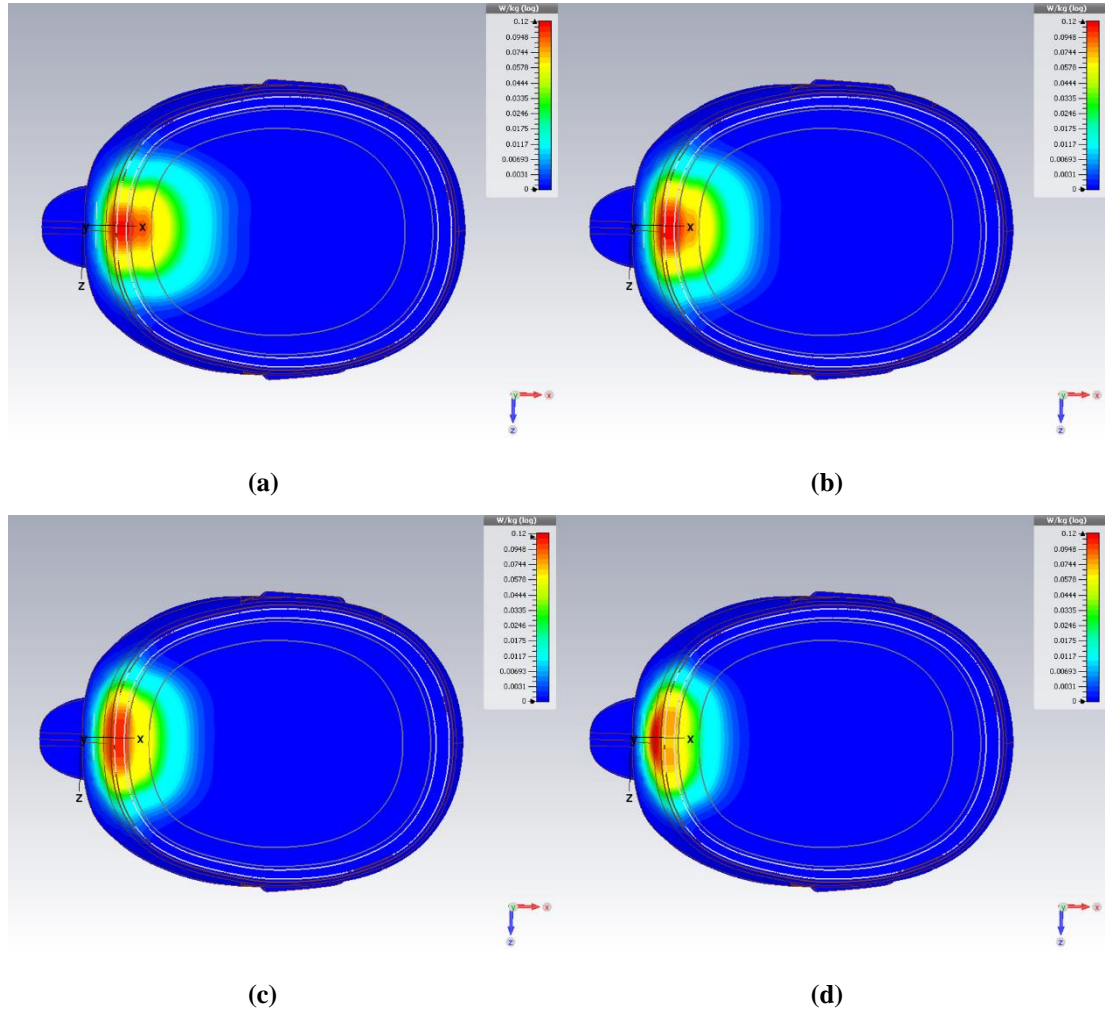


Figure 4.20: Simulated SAR distribution inside an artificial human head at (a) 1.5GHz, (b) 2GHz, (c) 2.5GHz and (d) 3GHz

4.4 Summary

This chapter discussed the development of the wearable antenna array using the antenna elements developed in the Chapter 3. The main considerations that have been made on developing the wearable array are the number of the antennas in the array, the minimum separation of adjacent antennas to reduce mutual coupling effect, flexibility and comfortability of the wearable prototype. To fit an antenna array on a patient head, two main configurations have been explored. The first prototype is designed by attaching the flexible antennas on a flexible absorber covered with a conductive sheet that has been shaped according to an artificial realistic human skull.

Chapter 4: Wearable Prototypes for Microwave Head Imaging

The main objective of using the reflector backed absorber is to suppress back lobe radiations of the monopole antennas that may compromise the performance of the proposed head imaging device. Additionally, the absorber also serves as a wearable unit that can be worn by a patient. For the second configuration, a wearable prototype has been realised by utilising a head band. The sensing antennas are attached to the head band to enable the prototype to be used for different head shapes compared to the first prototype where its structure is relatively rigid. The S_{11} signals of the antenna arrays were measured for both prototypes. Based on the measurement results, the impedance bandwidth of the antennas when arranged in an array show similar performance as a single element due to ample separation between them. Besides, the mutual coupling effect between two adjacent antennas evaluated by mean of transmission coefficient, indicates low coupling effect. To measure the safety aspects of the proposed wearable array, the SAR values at different transmitted power levels and frequencies were calculated in an electromagnetic solver, CST Microwave Studio. To ensure that the proposed wearable imaging system operates within the safety regulations imposed by a relevant governing body, the power transmitted by the sensing antenna should be limited to 0.1W. It is found that low frequency content microwave signal provides better penetration depth inside the human head compared to higher frequency signal. Hence, it is very crucial to use low frequency microwave signal in the range of 1GHz to 3GHz for head imaging systems.

Chapter 5: Novel Compact RF Switch Circuit for Wearable Head Imaging Systems

5.1 Introduction

To develop a wearable head imaging device, a compact and lightweight RF switching circuit for the antenna array presented in the previous chapters is developed using commercial off-the-shelf (COTS) components. Two evaluation boards of monolithic microwave integrated circuit (MMIC) single-pole eight-throw (1P8T) switch, HMC321LP4E and single-pole four-throw (1P4T) switch, HMC241ALP3E from Analog Device are chosen [21][20]. The switches offer wideband operating frequency range from DC to 4GHz which is sufficient to cover the operating frequency normally used for head imaging applications. In order to provide enough penetration and sensible resolution inside the human head, most of the research in the literature utilise frequency band between 1GHz to 4GHz [11], [28], [32]. The diagram of the proposed switching architecture is shown in Figure 5.1.

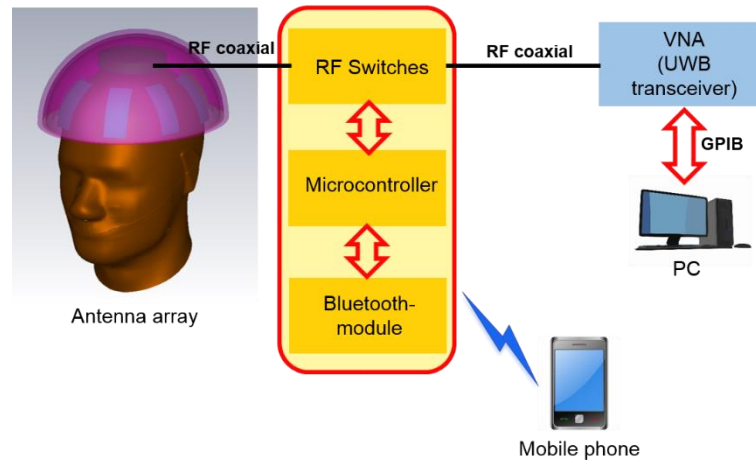


Figure 5.1: Diagram of the proposed RF switching system for wearable application

In order to serve as the switching controller circuit of the wearable system, an Arduino Nano board from Arduino was selected based on several criteria mainly its compact size and low power consumption. Both of the RF switches and the Nano board operate at 5V and can be easily powered up using a 9V battery. The microcontroller embedded inside the Arduino Nano, Atmel Atmega328P, consumes only 0.2mA during its operation mode. Another reason for the proposed integration of the microcontroller with the switches is to enable future integration with an ultra-wideband transceiver as a system on a chip (SoC) eliminating the need for an external and bulky transceiver such as vector network analyser. However, in this research, the main function of the micro-controller is limited to controlling the switches during their operations where an external vector network analyser is still utilised for signal generations and acquisitions.

Five control pins from the Arduino board are connected to both of the switches which control the selection of the switches' ports. A wireless connection is also implemented in the system to enable wireless control using an android based smartphone via Bluetooth module. The selection of Bluetooth module was due to its low power usage compared to WiFi module thus further reducing the power consumption of the overall system. An android application was coded and installed into a mobile phone to provide the graphical user interface (GUI).

To investigate the performance of the RF switches, their impedance matching performances were evaluated in terms of reflection coefficient using a vector network analyser at all the ports at frequency range up to 3GHz. The insertion losses of the switches were also measured. Finally, the proposed switching system was then connected to an array of twelve ultra-wideband monopole antennas. The reflection and transmission coefficient measurements were taken with the presence of an artificial head phantom for further analysis as will be presented in the next chapter.

Further work has been carried out to transfer the initial design using the off-the-shelf components to a final integrated circuit prototype using 6 layer PCB technology. The circuit was designed using DesignSpark software where several optimisations have been conducted to realise a compact fully integrated switching circuit. The

It consists of 23 programmable input and output (I/O) lines which are more than enough for the intended RF switching purposes. The additional features of Atmega328P include a flash memory (up to 32kB), data memory of 2kB, universal asynchronous receiver-transmitter (UART) interface, serial peripheral interface (SPI) and 8 analog to digital converter (ADC) channels. The device is in TQFP32 package and its pin configuration is illustrated in Figure 5.2.

5.2.2 GaAs MMIC SP4T Non-Reflective Switch

In the proposed switching circuit, two RF switches which are SP4T and SP8T switches have been utilised to form a single-pole eight-throw SP12T switch due to limited availability and high cost of a SP12T IC design in the market. In addition, by using two separate RF switches, the circuit can also be configured as multi-static configuration apart from the mono-static operation that is implemented in this research. The multi-static configuration could further increase the amount of useful data collected for future use especially for detection and monitoring of other kind of head diseases [29].

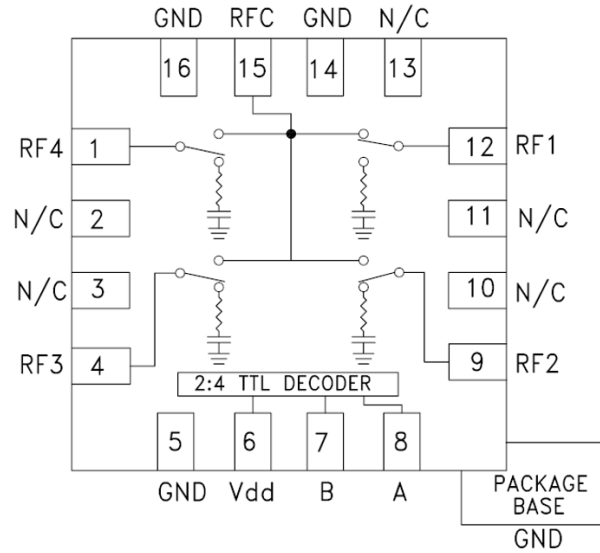


Figure 5.3: HMC241ALP3E SP4T non-reflective switch

[20]

The single pole four throw (1P4T) RF switch, HMC241ALP3E from Analog Device was chosen due to its low cost and low power consumption [20]. The switch operates on 5V which is the same voltage rating across the entire components in the circuit to reduce the voltage converters that may be required if different voltages are used. Moreover, the switch requires only 2 control lines and a positive bias to select each path that provides significant improvement over other gallium arsenide (GaAs) SP4T switches which normally require 4 to 8 control lines [20]. The HMC241ALP3E is housed in a 3×3 mm QFN package. Figure 5.3 shows the functional diagram of the 1P4T switch.

5.2.3 GaAs MMIC SP8T Non-Reflective Switch

The second RF switch employed in the circuit is HMC321LP4E SP8T non-reflective switch from Analog Device. The switch operates on 5V and requires 3 control lines to select one from the 8 available paths. Both of the switches are suitable for 50Ω systems. The HMC321LP4E is housed in a 4×4 mm QFN package and its functional diagram is shown in Figure 5.4.

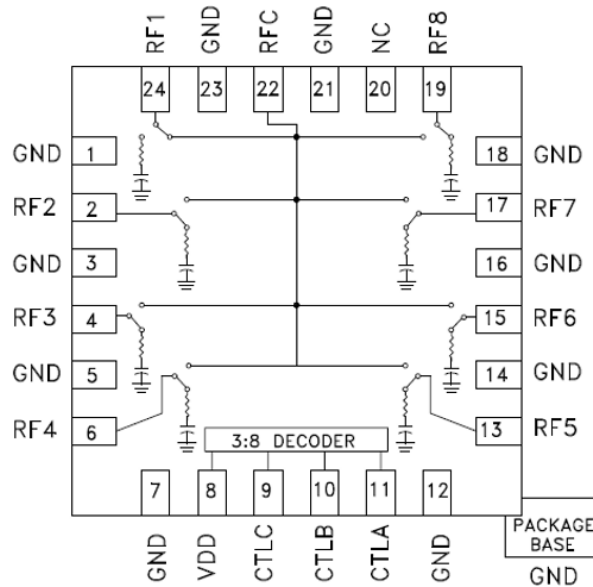


Figure 5.4: HMC321LP4E SP8T non-reflective switch [21]

5.2.4 USB to UART Interface FT232RL

Another important component in the circuit is a USB to UART interface FT232RL device. The FT232RL is used for the microcontroller to achieve a real time control. The device translates USB into UART interface in order for the microcontroller to communicate through USB connection to other mobile terminals. In this research, this connection enables the micro-controller to be programmed through a laptop or a PC. The FT232RL pin configuration is shown in Figure 5.5. The device is packaged in a 28 pin shrink small outline package (SSOP).

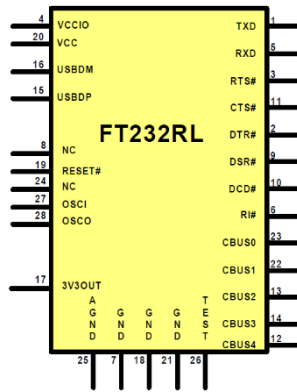


Figure 5.5: FT232RL pin configuration [22]

5.2.5 Bluetooth Module for Wireless Control

To achieve wireless control over the switching circuit, a low cost and low power consumption HC-06 Bluetooth module is selected. The HC-06 Bluetooth module has operating voltage of 3.3V to 5V with a built-in 2.4GHz antenna [23]. The wireless transceiver in the module has sensitivity (bit error rate) of up to -80dBm. When in operation, the current drawn by the module is around 8mA. Figure 5.6 shows the HC-06 Bluetooth module used for wireless control in the switching circuit design.

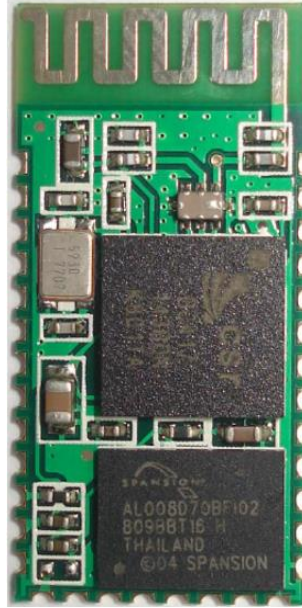


Figure 5.6: HC-06 Bluetooth module [23]

5.3 Characterisations of the RF Switches on Evaluation Boards using Vector Network Analyser

For the initial prototype of the switching circuit, most of the components utilised in the design came with their respective evaluation boards such as the RF switches. All of these components were then stacked together to build a compact RF switching circuit to be integrated with the proposed flexible antenna array to form a wearable interface for microwave head imaging and detection systems.

At first, the performances of both of the switches on their evaluation boards were first evaluated in terms of their insertion losses and reflection coefficients at each of the RF ports. The measurements were carried out using a two-port vector network analyser, HP8753C as exhibited in Figure 5.7. Due to the limitation of the VNA, only measurements up to 3 GHz were carried out. Nevertheless, considering that the RF switches are to be used for microwave head imaging and detection systems, most of the antennas designed for these applications work below 3GHz in order to provide adequate electromagnetic wave penetration inside the human head [11], [28].

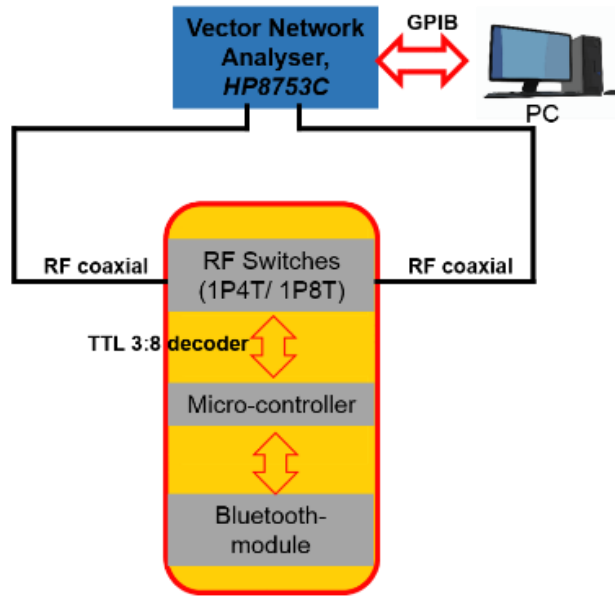


Figure 5.7: Diagram of the measurement setup for the RF switches

The insertion losses of the 1P4T switch and the 1P8T switch are shown in Figure 5.8 and Figure 5.9 respectively. It can be seen that the insertion loss of the 1P4T switch is lower than the 1P8T switch by 1.06 dB up to 3GHz. The maximum measured insertion loss at 2.5GHz is 2.54 dB at port7 of the 1P8T switch. The switches' reflection coefficient characteristics are illustrated in Figure 5.10 and Figure 5.11 respectively. The average measured reflection coefficients of the 1P4T and 1P8T switches at 2.5 GHz are -26.2 dB and -18.9 dB accordingly. The maximum measured reflection coefficient value is -17.5 dB at port 7 of the 1P8T switch. The difference in S_{11} responses between the two switches could be attributed to fabrication inconsistency

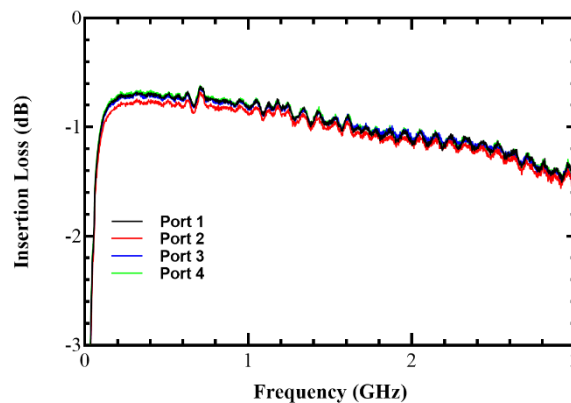


Figure 5.8: Measured insertion loss of single-pole-four-throw (1P4T) RF switch

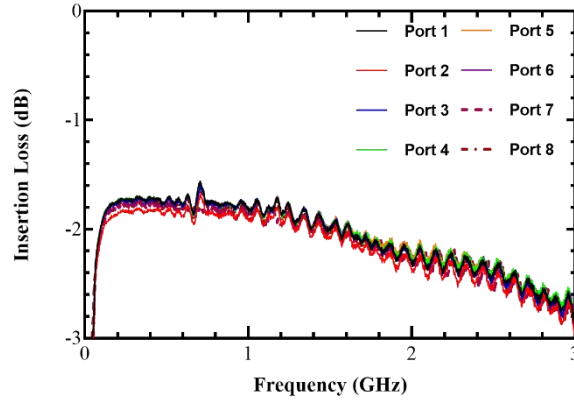


Figure 5.9: Measured insertion loss of single-pole-eight-throw (1P8T) RF switch

of the boards such as the dimensions of the co-planar waveguide (CPW) transmission line and soldering effects. Nevertheless, the measurement results show excellent impedance matching characteristic up to 3GHz which match the values provided by the datasheets. It is important to ensure that the switches' impedance matching would not deteriorate the performance of the antenna array that is to be integrated later in the final system.

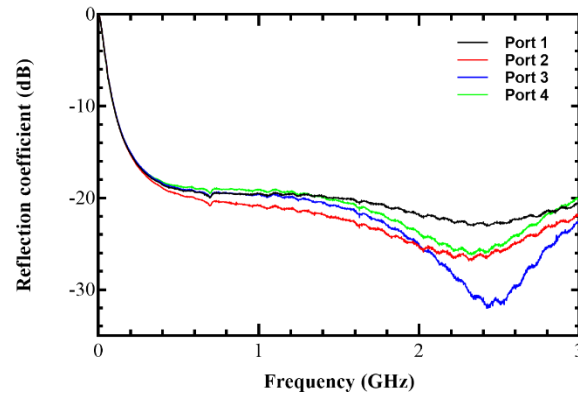


Figure 5.10: Measured reflection coefficient of the single-pole-four-throw (1P4T) RF switch

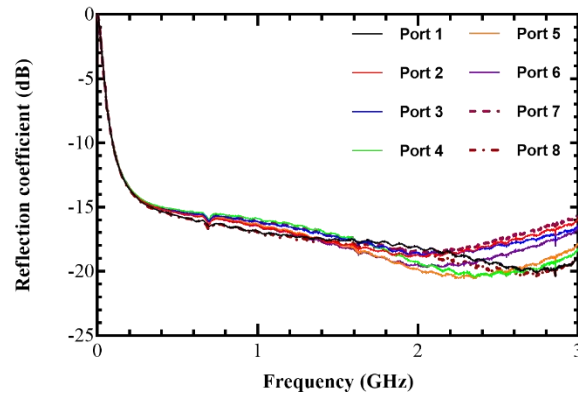


Figure 5.11: Measured reflection coefficient of the single-pole-eight-throw (1P8T) RF switch

5.4 Development and Implementation of the RF Switching Circuit

5.4.1 RF Switching Configuration

There are two main configurations that can be implemented using the developed circuit as illustrated in Figure 5.12; mono-static and multi-static switching configurations.

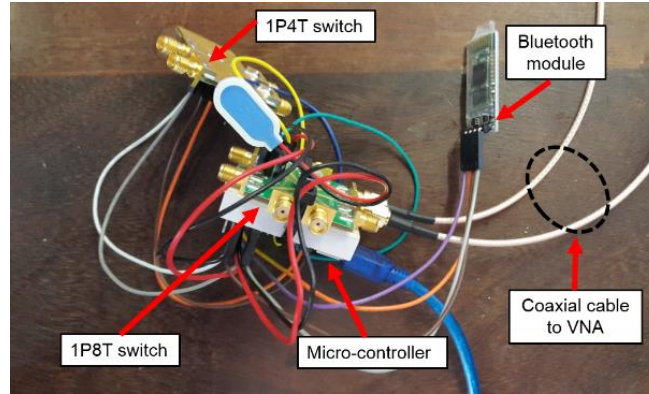


Figure 5.12: Photograph of the first prototype of the switching circuit

5.4.1.1 Mono-static Switching Configuration

In this research, the mono-static switching configuration was adopted for the signal generation and acquisition when probing artificial heads. In this method, each of the twelve antennas in the array is selected wirelessly using an android based mobile

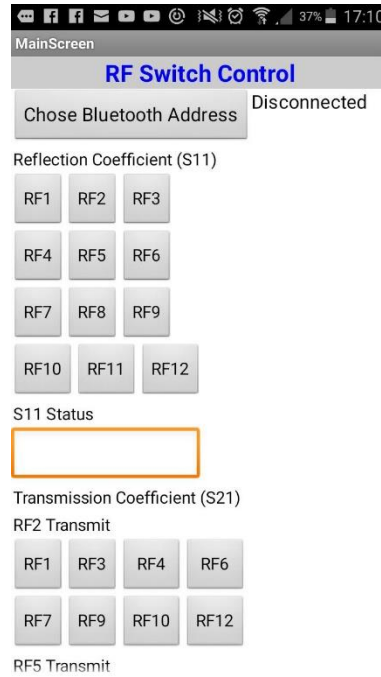


Figure 5.13: Graphical user interface on an android smartphone for the RF switch

phone. The wireless connection between the circuit and the mobile phone is established via the Bluetooth module described earlier. The circuit was first programmed via Arduino integrated development environment (IDE) with a control program to provide a control mechanism to the system. Next, a simple application was developed on android platform which provides a simple mean of selecting each one of the antennas in the array using a mobile phone as an interface.

For this mono-static arrangement, the data collected are the reflection coefficients of each of the antennas. Since the number of antenna elements utilised for the wearable head imaging system proposed in this research is twelve, hence twelve unique S_{11} data are acquired. These data were then processed to create a useful image that indicates the location of the stroke inside the head if existed. The photograph of the graphical user interface (GUI) on an android phone is shown in Figure 5.13.

5.4.1.2 Multi-static Switching Configuration

Alternatively, the proposed switching circuit can also be configured as multi-static configuration where an antenna pair in the array can act as transmitting and receiving antennas respectively. In this method, four antennas are connected to the

SP4T switch act as transmitting antennas while the remaining eight antennas connected to SP8T switch serve as the receiving antennas. This configuration provides 24 unique transmission coefficient data that can be analysed for imaging or detection purposes. However, the S_{21} data collected using this method were not being used in the imaging process due to algorithm complexity that it may pose but will serve as future improvement to the system.

5.4.2 PCB Implementation of the RF Switching Circuit

To improve the switching system, a PCB implementation of the circuit in order to realise a compact integrated circuit (IC) of the switch is developed using the same components from the initial prototype. Instead of using the components' evaluation boards, most of the key components were fabricated on a single piece of PCB board making it more compact than the first prototype. This will enhance the performance of the device in terms of its size and provide better integration with the antenna array.

5.4.2.1 Circuit Diagram

Similar to Arduino Nano, this circuit consists of Atmega328P as its micro controller, an SP4T RF switch, an SP8T switch, USB to UART FT232RL and a voltage regulator as shown in Figure 5.14. The only difference between this circuit and the initial prototype is the SP8T switch where the previous version of the switch (HMC321LP4E) has been discontinued by its manufacturer and is replaced with a newer version (HMC253ALC4) that offers better performance in terms of its insertion loss. However, all other characteristics of the switch such as its operating voltage and pin configuration remain unchanged. The circuit design and the PCB layout were constructed in the PCB design tool, DesignSpark PCB.

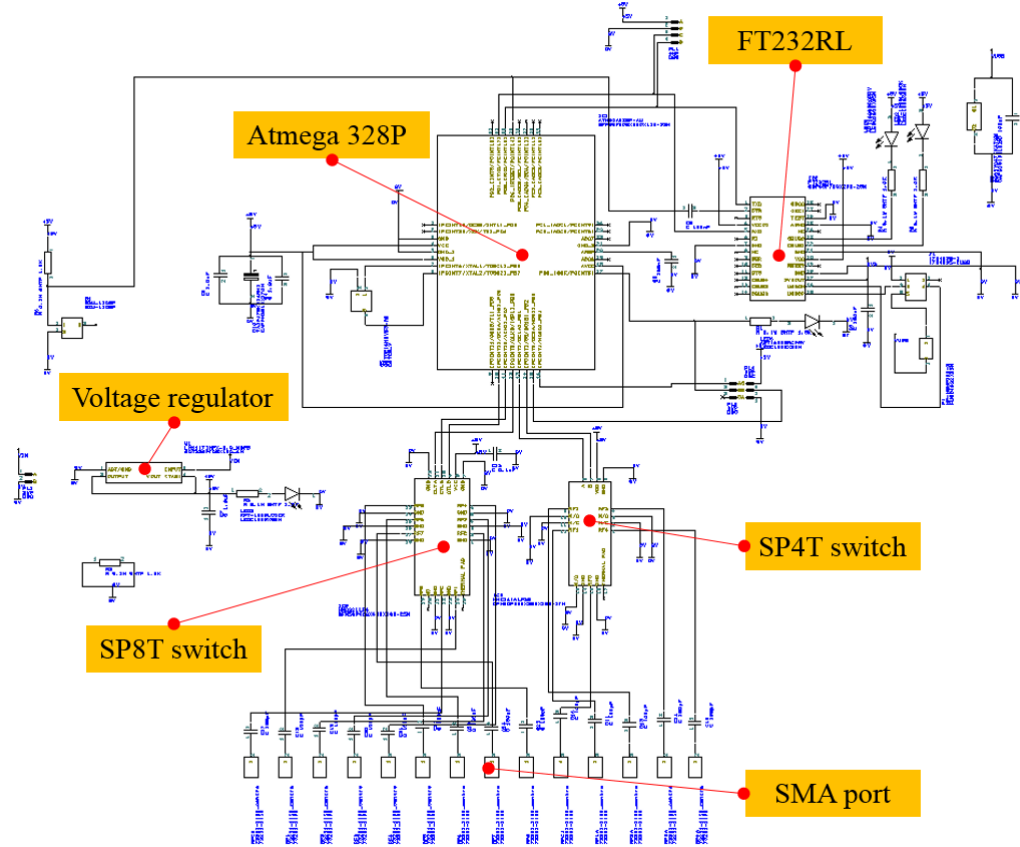


Figure 5.14: Schematic of RF switching circuit diagram

Out of 32 pins on the microcontroller, only 20 pins are used in this application. 5 pins which are PIN10, PIN11, PIN12, PIN13 and PIN14 serve as control lines to both of the RF switches. PIN7 and PIN8 are connected to a crystal oscillator of 16MHz. The FT232RL chip communicates with the microcontroller via PIN1 and PIN5 for USB communication. The main external power supply is connected to the microcontroller using PIN4 and PIN6. The remaining pins are mostly connected to the ground where several coupling capacitors and pull-up resistors are utilised to protect the microchips.

5.4.2.2 Evaluation of the Circuit via Breadboard Testing

Before fabricating the circuit on a PCB, the design based on the schematic shown in Figure 5.14 was first built on a breadboard to test its functionality. An adapter was

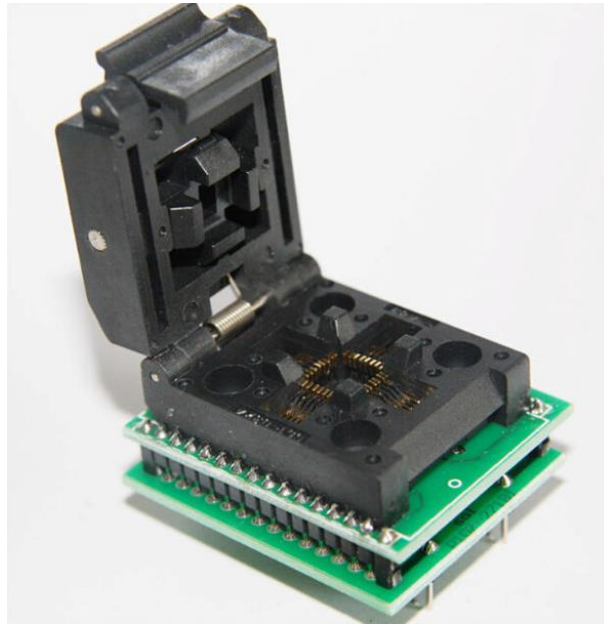


Figure 5.15: TQFP-32 adaptor for Atmega328P-AU

used to place the Atmega328P-AU on the breadboard since it was housed in TQFP-32 package as shown in Figure 5.15.

The microchip was first installed with bootloader and programmed using Arduino IDE with the switching control application. Once the control program has been installed onto the chip, the actual connections based on the schematic were made as illustrated in Figure 5.16. Based on Figure 5.16, the adapter with the microcontroller inside was placed on the breadboard where several jumper wires were used to make the connections to others components in the circuit. A voltage regulator was used to convert the 9V from an external battery to 5V to power up the Atmega328P chip. The voltage regulator also supplies voltages to the switches and the FT232TL device. Five LEDs were connected to the control pins (PIN10, PIN11, PIN12, PIN13 and PIN14) to test the circuit. A Bluetooth connection was established between the microcontroller and an android mobile phone where the LEDs can be turned on and off based on the developed program during the test. This indicates that the circuit was working properly according to the design.

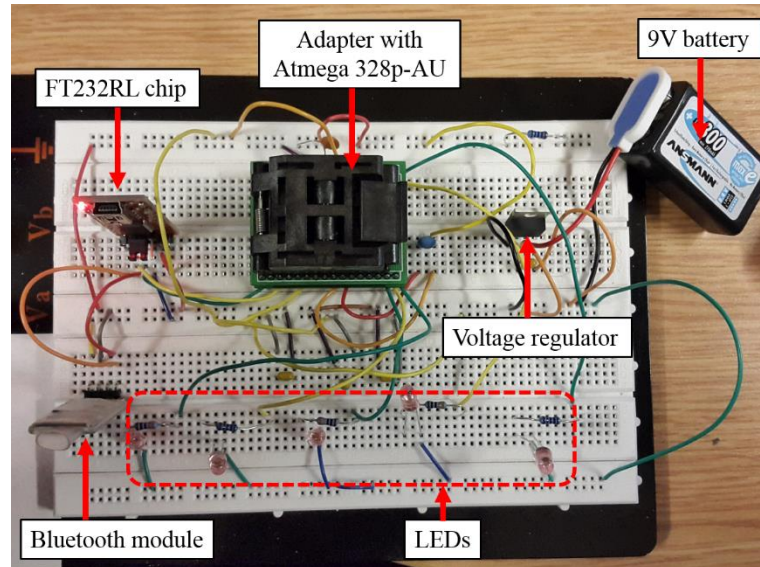


Figure 5.16: Breadboard to test the control circuit for the switch

RF and DC signal	Layer 1
Ground Plane	Layer 2
DC signal	Layer 3
Power Plane	Layer 4
Ground Plane	Layer 5
RF and DC signal	Layer 6

Figure 5.17: 6 layer PCB stack up

5.4.2.3 Fabrication of the Circuit Design on PCB

Based on the success of the circuit implementation on the breadboard, the circuit design was translated into PCB structure using DesignSpark PCB software. In this design, a 6 layer PCB with 6 metal layers structure was selected as shown in Figure 5.17.

The selection of the 6 layer PCB stack up is driven by several factors such as the need to facilitate the integration of both DC and RF signals on the same board, to reduce the size of the board, to minimise the electromagnetic interference (EMI) and to ensure the components can be easily arranged across the board. The top and the bottom layers of the PCB are for both DC and RF signal traces. The second and the

fifth layer are reserved for ground plane. The power plane is located at layer 4 of the PCB. At layer 3, only DC signals are populated on that layer.

Most of the components are placed on the top layer which include the Atmega328P-AU chip, 1P4T RF switch (HMC241ALP3E), USB interface FT232RL and the voltage regulator. The 1P8T RF switch (HMC253ALC4) is placed on the bottom layer to avoid potential overlapping with the RF traces from the other switch. The ground planes are set at the two layers below the top and bottom layer in order to facilitate the construction of the microstrip transmission line for the RF paths. The 6 layers are connected using vias. The track dimensions for the DC traces is 100 μ m while for RF traces, 300 μ m width of signal line is utilised. The wider RF line used is to minimise the overall loss of the RF signal routes.

5.4.2.3.1 Optimisation of the Microstrip RF Transmission Lines on 6 layer PCB Board

One of the main challenges in the PCB design is to optimise the RF paths that connect the switches to the SMA ports. In the initial prototype, the switches were on evaluation boards where the routings have been already fabricated on the board by their manufacturers. In this single PCB design, the routings need to be redesigned based on the PCB technology used for the circuit. There are several factors that need to be taken into account such as the impedance matching of the path to ensure that the RF signals can travel smoothly with minimal losses between the ports, the losses due to bends on the paths and the availability of space on the board that also includes DC paths from other components. Due to the selection of the 6 layer PCB technology, the RF paths can be efficiently separated from the DC paths.

The track width for the RF traces is set to 300 μ m where the characteristic impedance (Z_0) of the microstrip line is 50 Ω . Since all twelve SMA ports on the circuit need to be placed around the edges of the board, the RF traces from each port to the switches have to be carefully constructed to ensure the impedance of the line remains at 50 Ω . To ensure lines' losses are kept at minimum, the amount of bends on the traces are minimised. After the RF routes has been finalised, the PCB layout was transferred to CST Microwave software to characterise the RF path before going into actual PCB

Chapter 5: Novel Compact RF Switch Circuit for Wearable Head Imaging Systems fabrication. This would provide valuable insight into how the transmission lines would behave.

5.4.2.3.1.1 UWB Microstrip-to-Microstrip Transition

The straight SMA ports from Molex used in the circuit are actually intended for a two layer PCB board with thickness of 1.6mm. However, the 50Ω microstrip lines on the 6 layer board are designed with a thickness of only $200\mu\text{m}$ between the signal and the ground layer. As such, a microstrip-to-microstrip transition between the 50Ω microstrip lines at the pad of the SMA ports to the transmission line is required. To accommodate this, a rectangular slots are cut at each layer on the PCB to make sure that 50Ω microstrip line is realised at the pads where the SMA connectors will be soldered. The width of the centre trace is set to 2.5mm which translates to 50Ω . At the boundaries as shown in Figure 5.18, the ground of the microstrip lines are at different levels although both of the lines are at the same impedance value of 50Ω . Based on this transition design, the overall structure as shown in Figure 5.19 was simulated and further optimised in CST Microwave Studio.

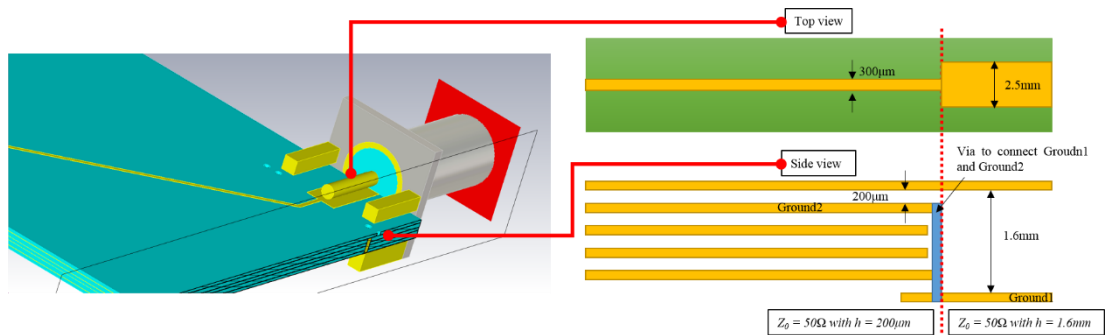


Figure 5.18: Detailed microstrip-to-microstrip line transition structure

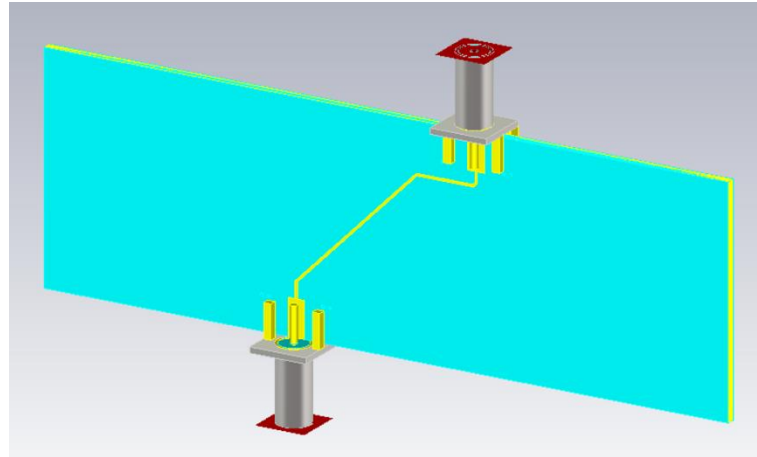


Figure 5.19: One of the RF traces on the PCB simulated in EM solver

Several vias are used to connect Ground1 and Groud2 of the transmission lines at the transition. Figure 5.20 shows electric field lines at the transition between two different thicknesses of microstrip lines. It can be observed that the electric fields are confined between the centre conductor and the bottom grounds as expected of a microstrip line along the line although both lines have different thickness. This indicates smooth field transformation has been obtained using the proposed transition method.

The reflection and transmission coefficients of the line are depicted in Figure 5.21 and Figure 5.22. The results show that the transition and the routing of the RF

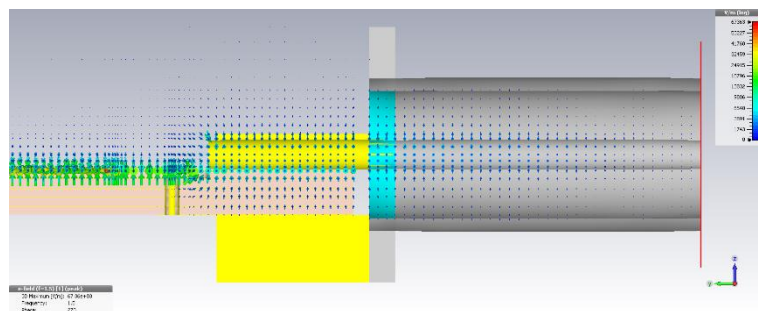


Figure 5.20: Simulated electric field lines at the cross section of the microstrip-to-microstrip transition

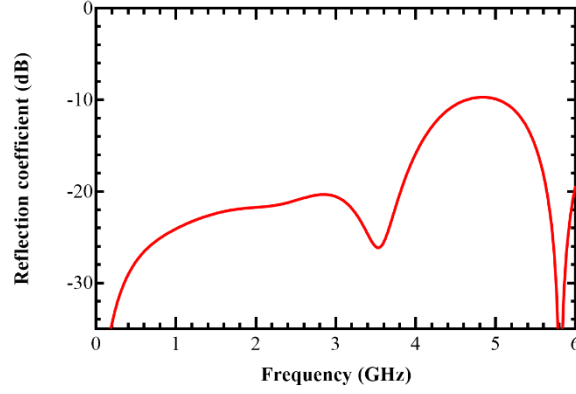


Figure 5.21: Measured reflection coefficient of the single-pole-four-throw (1P4T) RF switch

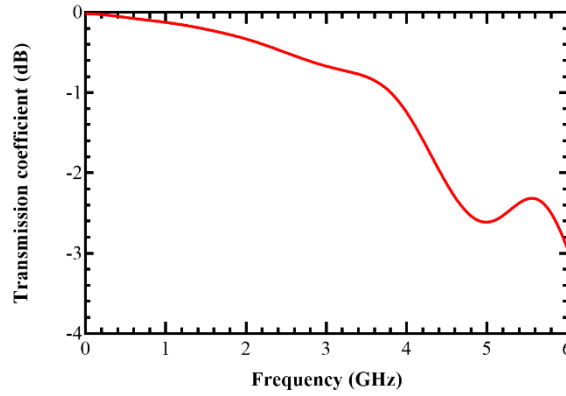


Figure 5.22: Measured reflection coefficient of the single-pole-four-throw (1P4T) RF switch

path between two ports are optimised for the PCB design since the S_{11} and the S_{21} are below -10dB and less than 1dB up to 3GHz respectively.

Figure 5.23 displays the final PCB layouts with overall dimension of 70mm \times 55mm. Once the PCB layout has been finalised, the PCB structure was fabricated by Multi Circuit Board Ltd in Germany [110] and assembled by a technician in the University of Edinburgh.

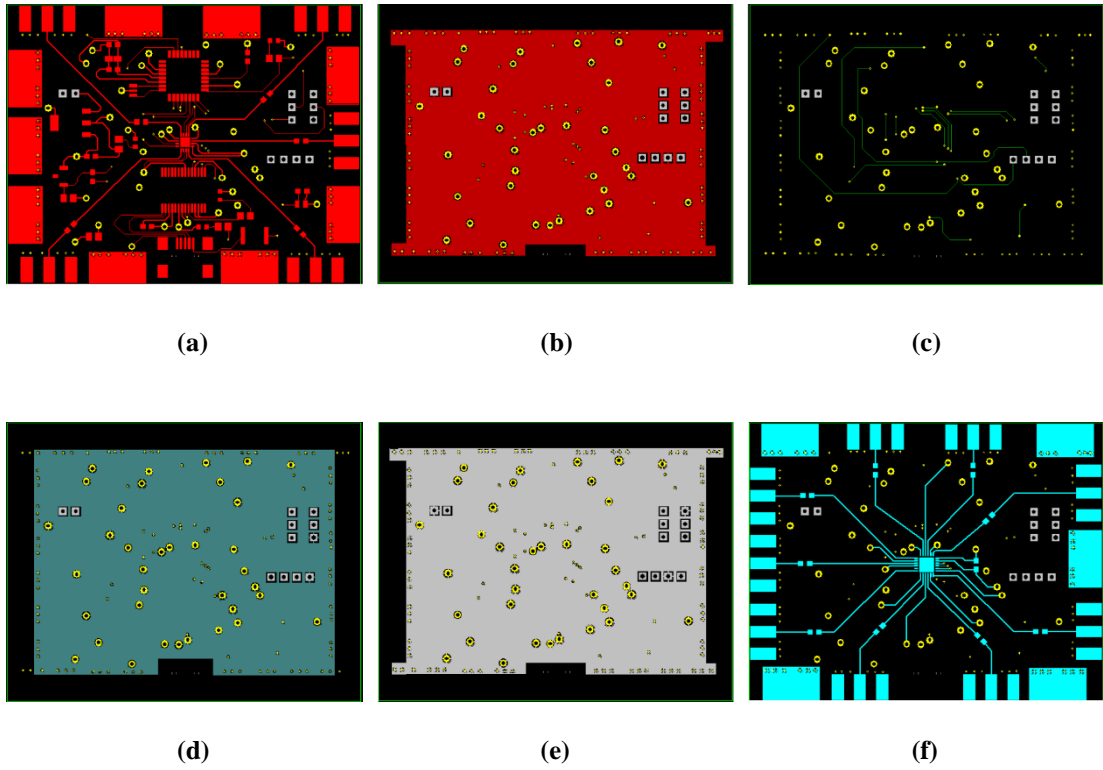


Figure 5.23: PCB layout of the circuit design (a) Layer 1 (b) Layer 2 (c) Layer 3 (d) Layer 4 (e) Layer 5 and (f) Layer 6

5.4.2.4 Evaluation of the PCB Design

The final fabricated PCB design is illustrated in Figure 5.24. The fabricated PCB was then characterised based on the measurement setup shown in Figure 5.25. The performance of the switching circuit was measured in terms of reflection and

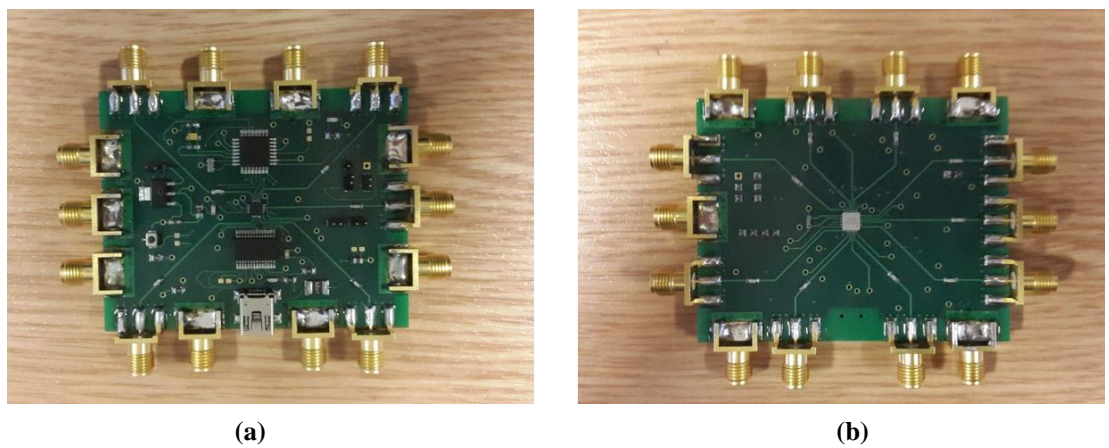


Figure 5.24: Fabricated PCB design (a) Top view (b) Bottom view

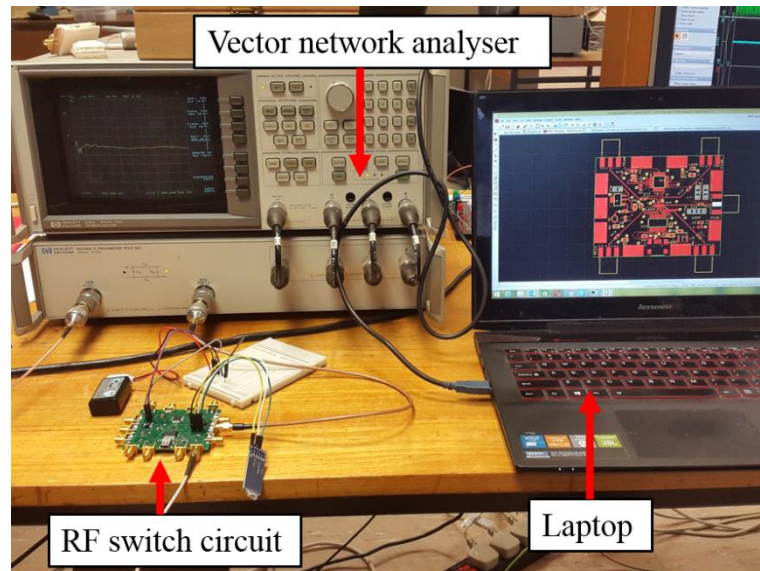


Figure 5.25: Measurement setup for the PCB design

transmission coefficients similar to the initial prototype. The impedance matching at all of the switches' ports and the insertion losses at all paths between the input and output ports were evaluated based on the S_{11} and S_{21} parameter respectively. The switches' reflection coefficient characteristics are illustrated in Figure 5.26 and Figure 5.27 respectively. The average measured reflection coefficients of the 1P4T and 1P8T switches at 2 GHz are -21.3dB and -15.88dB. The maximum measured reflection coefficient value is -6.16dB at port1 of the 1P8T switch. It is seen that most of the ports show deterioration in the impedance matching above 2.2GHz where the S_{11} values increases to -6dB. This reduction in the matching performance was not shown

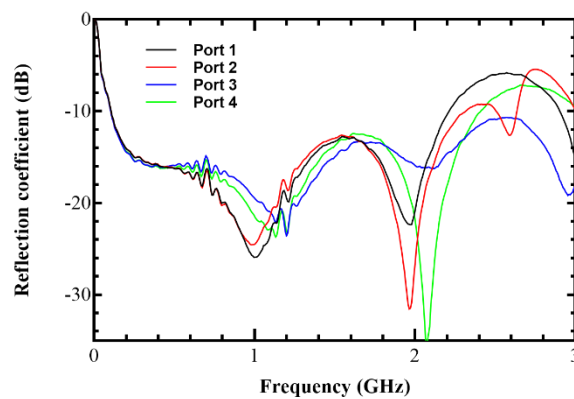


Figure 5.26: Measured reflection coefficient of the single-pole-four-throw (1P4T) RF switch

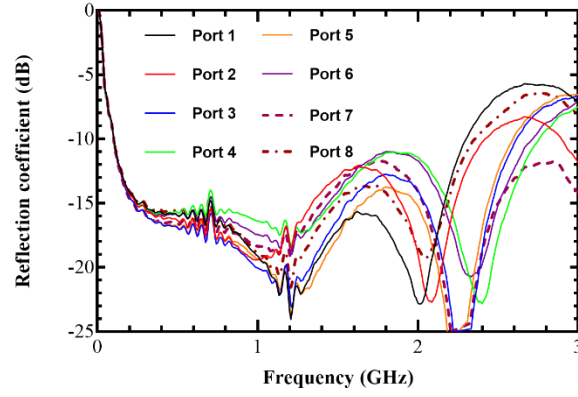


Figure 5.27: Measured reflection coefficient of the single-pole-eight-throw (1P8T) RF switch

in the simulation results earlier. This could be due to the several reasons such as different dielectric constant value for the FR-4 and the thickness of the layers of the 6 layer PCB used in the simulation compared to the actual values. Nevertheless, the S_{11} values below -6dB is still acceptable which indicates around 75% of power are being delivered compared to 90% of power for -10dB standard [111]. The insertion losses of the 1P4T switch and the 1P8T switch are shown in Figure 5.28 and Figure 5.29 respectively.

It is seen that the insertion loss of the 1P4T switch is slightly lower than the 1P8T switch by 0.34dB at 2GHz. The maximum measured insertion loss is 9.51dB at 2.7GHz of port 2 of the 1P4T switch. Due to high loss of the circuit, the operating frequency of the switch should be limited to 2.2GHz. Due to reduction in matching

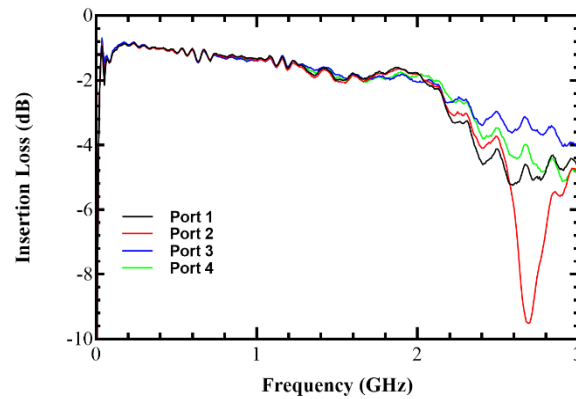


Figure 5.28: Measured insertion loss of single-pole-four-throw (1P4T) RF switch

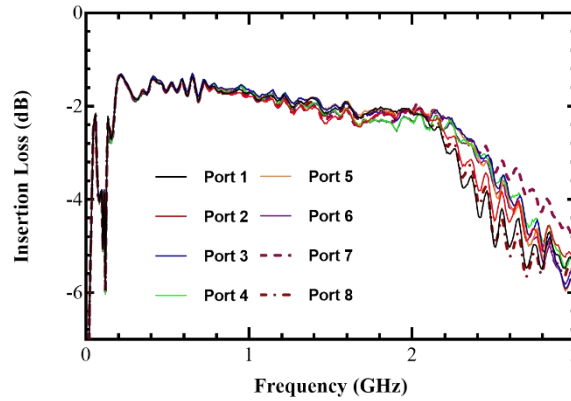


Figure 5.29: Measured insertion loss of single-pole-eight-throw (1P8T) RF switch

performance of the switches above 2.2 GHz, significant increases in the insertion loss up to 4dB are also observed for most of the ports whereas in the initial prototype, the maximum insertion loss is around 2.91dB at 3GHz an increase of 1dB. This can be attributed to signal loss due to higher number of bends on the RF traces compared to the switches on the evaluation boards. Further improvement on the matching performance above 2.2GHz should be addressed in the future.

5.5 Summary

In this chapter, a novel compact RF switching circuit for wearable head imaging systems has been presented. In the first prototype, the circuit was built using off-shelf-components consisting of Arduino Nano board, evaluation boards of two RF switches and a Bluetooth module. A control program was developed and programmed onto the circuit where the device can be controlled wirelessly using an android phone. There are two main configurations that the circuit can be utilised which are mono-static and multi-static methods. The RF switches were characterised in terms of their reflection and transmission coefficients using a vector network analyser. Based on the success of the initial prototype, the circuit was redesigned on a PCB where the components are integrated on a single board rather than separate boards stacked together.

The schematic and the layout of the circuit were designed using DesignSpark PCB, a free PCB tool by RS Components. Based on the schematic, the design was transferred to a breadboard for initial testing. Next, the RF traces on the board were

Chapter 5: Novel Compact RF Switch Circuit for Wearable Head Imaging Systems

first characterised and evaluated using an EM solver, CST Microwave Studio. Afterwards, the fabricated PCB design was characterised and compared to the initial prototype. Overall, the PCB design shows good performance in terms of impedance matching and insertion loss although some deterioration could be observed especially for frequency range above 2.2GHz. Chapter 6 will demonstrate the full integration of the switching circuit and the antenna array for validation of the detection performance of the system on an artificial head phantom.

Chapter 6: Experimental Measurement on Artificial Head Phantoms

6.1 Introduction

In this chapter, testing and performance validation of the prototypes are performed using artificial head phantoms that mimic the electrical properties of actual human head. Firstly, an initial experiment using liquid based phantom is conducted to investigate the smallest stroke target that the proposed antenna could detect and sense. A liquid which has similar electrical characteristic to that of brain tissue in terms of permittivity and conductivity is used to represent the brain while an artificial blood of various sizes are also fabricated to mimic a haemorrhagic stroke. In the next stage, a realistically shaped artificial head phantom is fabricated using low cost and nontoxic ingredients to be used in the second stage of the experiment. The main materials for the artificial head tissues are tap water, sugar, agar and salt. In addition, to improve the lifespan of the phantom, preservative material such as sodium benzoate is used to kill the bacteria, fungi and spores that may grow on the artificial tissue for repeatable testing purpose. Finally, lamb brains are used for the phantom to further investigate the detection capability of the proposed wearable head imaging devices.

There are three main sections of this chapter. Section 6.2 presents an initial experimental work on a simple phantom consisting of a liquid mimicking brain tissue and various sizes of stroke-like targets to verify the sensitivity and the detection capability of the proposed antenna. Section 6.3 describes the fabrication process of the artificial head phantom used in the experiment and the measurement setup for the second experiment. The analysis of the measurement results is given in Section 6.4.

6.2 Investigation on the Sensitivity and the Detection Capability of the Proposed Antenna

In this section, the detection and sensitivity of the antennas were investigated by performing experiments on a liquid based phantom. A liquid with electrical properties similar to brain tissue was fabricated according to recipes in [29]. The main ingredients of the artificial brain are tap water, sugar and salt. To represent haemorrhagic stroke, cube shaped targets of various sizes were also fabricated. To validate the electrical properties of the developed fabricated tissues, a dielectric probe, 85070E from Agilent was used to measure the final product and compared with the actual tissues based on data from literature in terms of its permittivity and conductivity [112]. Due to the use of tap water instead of distilled water, the recipes has been changed accordingly to take into account the higher conductivity of the tap water. The final recipes of the artificial brain blood are given in Table 6.1. The measurement setup for measuring the electrical properties of the fabricated tissues is shown in Figure 6.1. The critical components of the dielectric measurement system are a vector network analyser, 85070E dielectric

Table 6.1
RECIPES FOR WHITE MATTER AND BLOOD PHANTOMS
(VOLUME PERCENT)

Ingredients	White Matter (%)	Blood (%)
Tap water	47.7	59.8
Sugar	43.5	29.3
Agar	8.6	10.8
Salt	0.2	0.1

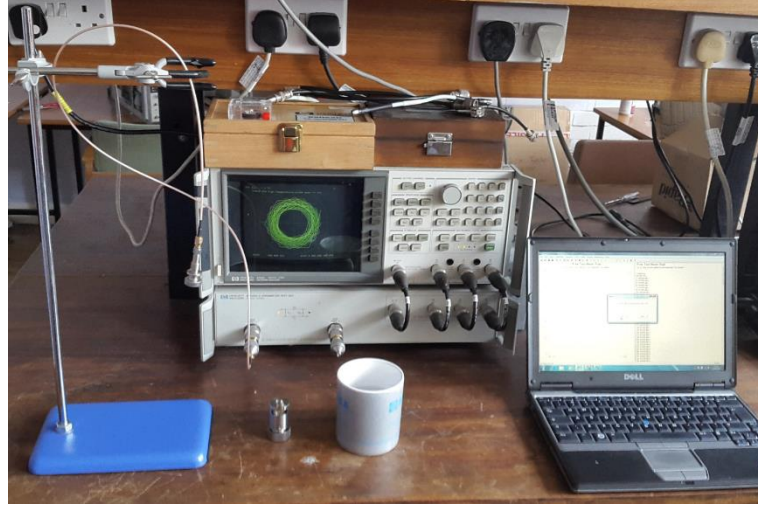


Figure 6.1: Dielectric measurement setup

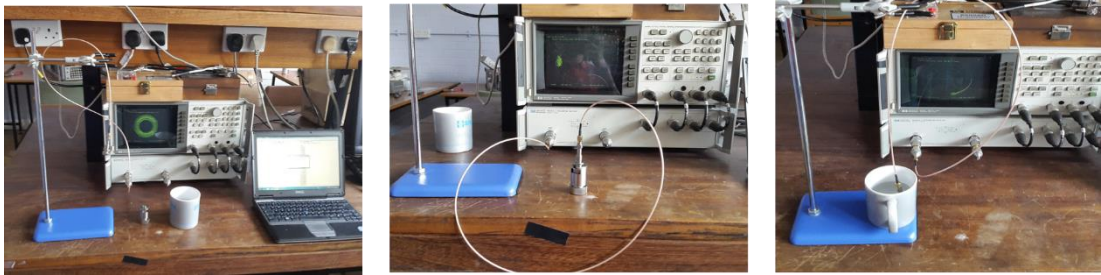


Figure 6.2: Calibration standard for the dielectric probe (a) air (b) shorting probe (c) water

probe kit, 85071 materials measurement software and a laptop. The probe calibration was performed by measuring three standards which are air (open), shorting block (short) and water as illustrated in Figure 6.2.

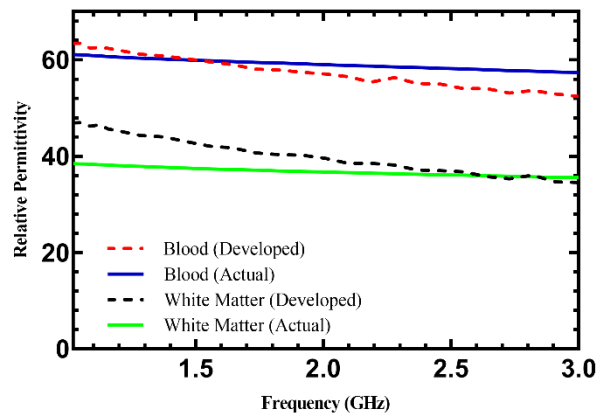


Figure 6.3: Relative permittivity of the fabricated phantom

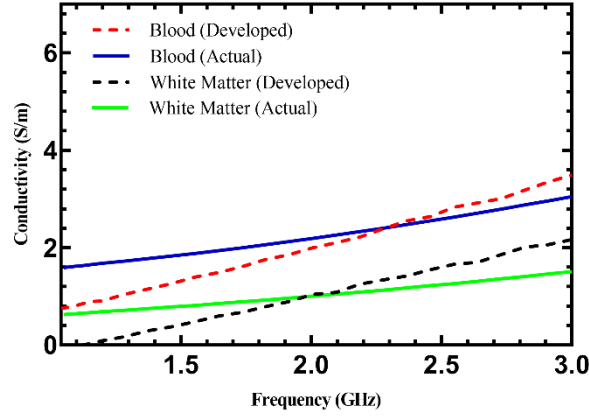


Figure 6.4: Conductivity of the fabricated phantom

The measured dielectric constant and conductivity of the developed liquid for the brain tissue and the stroke are compared to the actual tissues' properties obtained in [112] as displayed in Figure 6.3 and Figure 6.4 respectively. The brain tissue for this experiment is represented by white matter due to its larger ratio than the grey matter in human brain. It is seen that the variation of the permittivity of fabricated liquid based brain tissue with the actual brain is around 5% across the frequency range up to 3GHz. For the artificial stroke tissue, a good agreement was obtained with the actual blood where the variation is less than 10% and 23% for the permittivity and the conductivity respectively. The average dielectric contrast between the healthy brain and the stroke from 1.5GHz to 3 GHz is 1.52. As for the conductivity, the average contrast is 1.73 across the same frequency band.

Next, experiments were conducted using the monopole antennas described in Chapter 3 on the liquid-based phantom. The main objective of the experiments is to evaluate the sensitivity of the antennas to detect the existence of a stroke embedded inside the artificial brain. Previous studies on microwave head imaging systems mostly employed Vivaldi antennas as the probing elements due to its high gain and directionality. Furthermore, compact 3-D directional antennas proposed in [15], [28] have also been used for the head imaging applications. However, these type of antennas are not practical for wearable applications due to their high profile and rigid

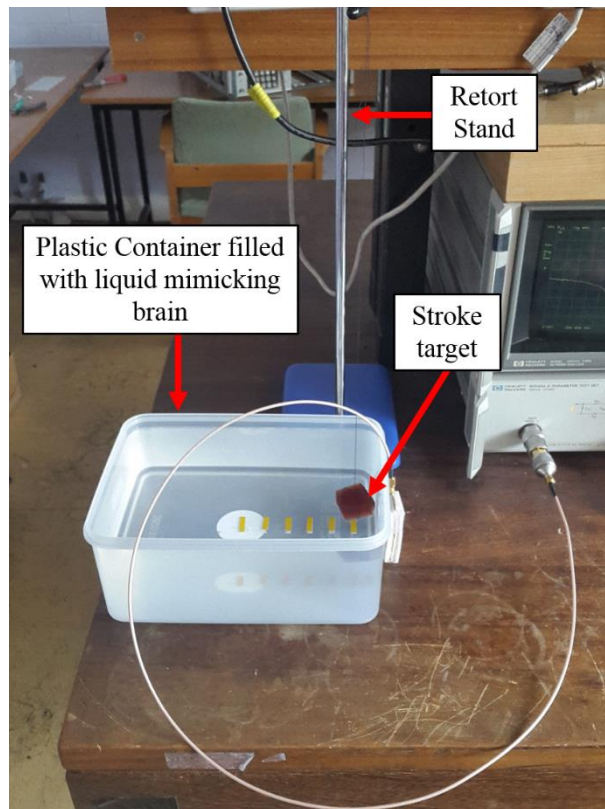


Figure 6.5: Measurement setup for antenna sensitivity test

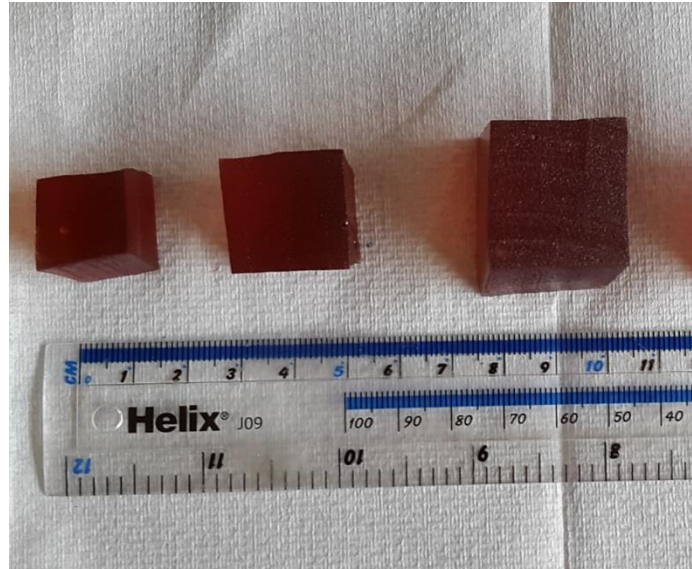


Figure 6.6: Artificial stroke targets with various size

structure. Therefore, initial experimental studies were needed to verify the efficacy of using flexible monopole antennas such as the one proposed in this thesis for microwave head imaging. The experimental arrangement is shown in Figure 6.5.

The experimental setup consists of a rectangular plastic container filled with liquid mimicking brain with a cube shaped artificial blood target immersed inside the liquid. Several sizes of the target were fabricated from $15\text{mm} \times 15\text{mm} \times \text{mm}$ to $25\text{mm} \times 25\text{mm} \times 25\text{mm}$ as shown in Figure 6.6. The antenna was attached on the container with a 6mm gap between the antenna and the container which is provided by the felt spacer. No matching liquid is used in this imaging device in order to reduce its complexity and overall weight. As a result, it is expected that the signal to noise ratio of the EM power transmitted and received by the antenna could be lower than those that employed matching liquid due to the reflection at the air-head interface [113]–[115]. Nevertheless, several research have shown that without using a matching liquid, successful detection of stroke and other diseases such as traumatic brain injuries are achieved by proper antenna designs [11], [12]. A part from the blood size, the distance from the antenna to the target was also varied. Before performing the measurement, a standard calibration procedure was carried out on the VNA. Measurements were taken at 401 points over the frequency range of 300kHz to 3GHz where the data were averaged over 3 frequency sweeps. The S_{11} data for all cases were measured and transferred into a laptop for post-processing.

The variation of the S_{11} signals for different sizes of the blood target at a distance of 20mm from the antenna are shown in Figure 6.7. The result shows that only target of size 15.63cm^3 could produce detectable and consistent different in S_{11} magnitude compared to the reference signal (no target present) over several measurements. Similar results were obtained for other antennas. As for the smaller targets, the scattered signals could be too weak to be detected by the utilised VNA to cause any change to the measured reflection coefficient of the probing antenna. Having found the smallest volume of the stroke that the antenna could detect, its distance to the antenna was varied in the next experiment. It can be clearly seen that the farther the target is from the antenna, the smaller the difference in S_{11} magnitude. This concludes that the strength of the reflected signal is weaker as the distance of the target is increased. However, the variation of the signal's amplitude is not consistent throughout the operating frequency band of the antenna compared to the reference signal when there is no target. It is observed that pronounced difference in S_{11} values occurs at 2.2 to 3GHz frequency range whereas at 1.5GHz to 2GHz frequency band, smaller variation of S_{11} data was recorded. This scenario has also been reported in [57] for breast cancer detection where the authors observed only at frequency below 1GHz shows detectable differences in the reflected signals although the antenna has been designed to operate up to 9GHz. They reported that by windowing the frequency domain data in the range of 0.1GHz to 1GHz, there is no resolution loss compared to using the whole frequency spectrum up to 9GHz. However, by removing the data below 1GHz, the system fails to detect the existence of the tumour in the breast. Hence,

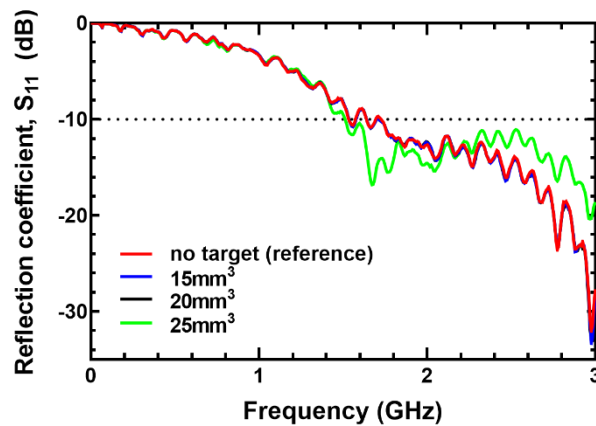


Figure 6.7: Variation of S_{11} magnitude for different target size

it is concluded that extensive experiments have to be conducted to find the optimal frequency ranges of the sensing antenna and its sensitivity in detecting small target in order to develop an efficient and accurate microwave head imaging device. Moreover, it is important to identify the limit of a sensing antenna in terms of the smallest target it could detect. In this experiment, the proposed flexible antennas could detect a blood clot with volume of 15.625cm^3 which is reasonably small considering that the antenna did not employ any matching liquid. In terms of stroke monitoring applications, it was reported in [116] that the survival rate of a stroke patient depends on the volume of parenchymal haemorrhage. For haemorrhages with a volume of less than 30cm^3 , the 30-day mortality were 23%, 7% and 53% for deep, lobar and cerebellar haemorrhages respectively [116]. This shows that a fast detection of the existence of blood clot inside

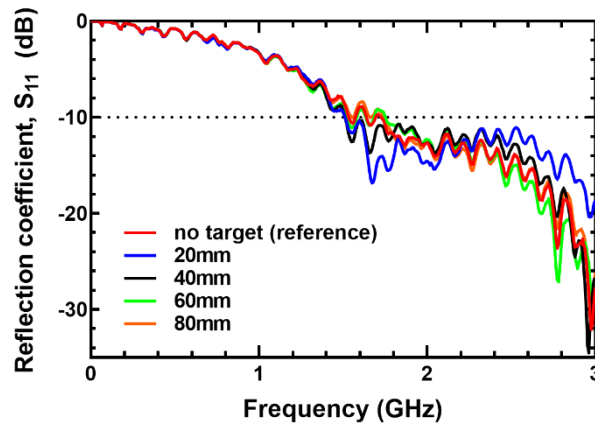


Figure 6.8: Variation of S11 magnitudes by varying the distance of the blood clot ($25\text{mm} \times 25\text{mm} \times 25\text{mm}$) from the antenna

the brain could potentially save a patient's live. In terms of the depth of the stroke inside the brain, the S_{11} signal could no longer be differentiated with the reference signal at a distance of more than 60mm as demonstrated in Figure 6.8. It is concluded that a formation of blood clot near the skull should be able to be detected by the proposed antennas. However, a detection of intraventricular haemorrhage might be very challenging or even impossible using the current antenna due to its location deep inside the brain.

6.3 Measurement Setup for the Wearable Prototype Testing

Based on the promising results from the initial experiments on a liquid based phantom, more complex and realistic head phantoms were adopted in the next measurements. Instead of using only a single antenna, a wearable prototype was assembled by integrating the antenna array with the switching circuit developed in the



Figure 6.9: Prototype with a dielectric absorber with switching circuit

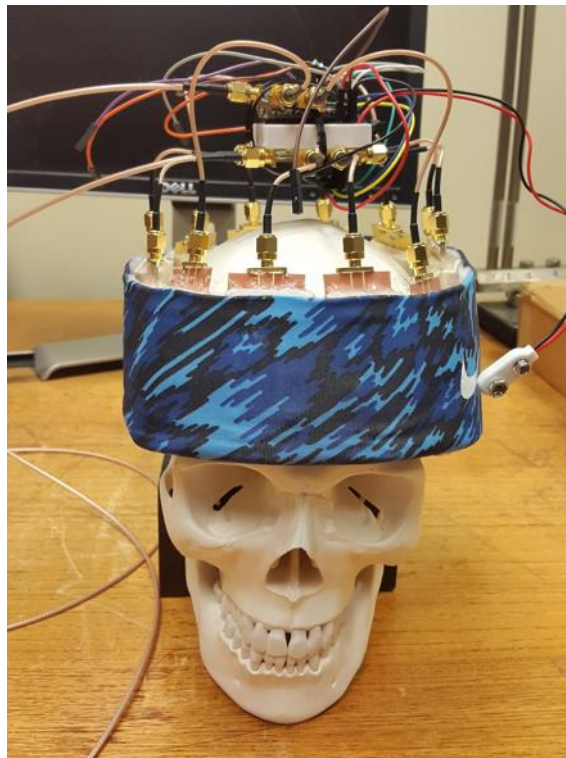


Figure 6.10: Strap based prototype without the use of an absorber

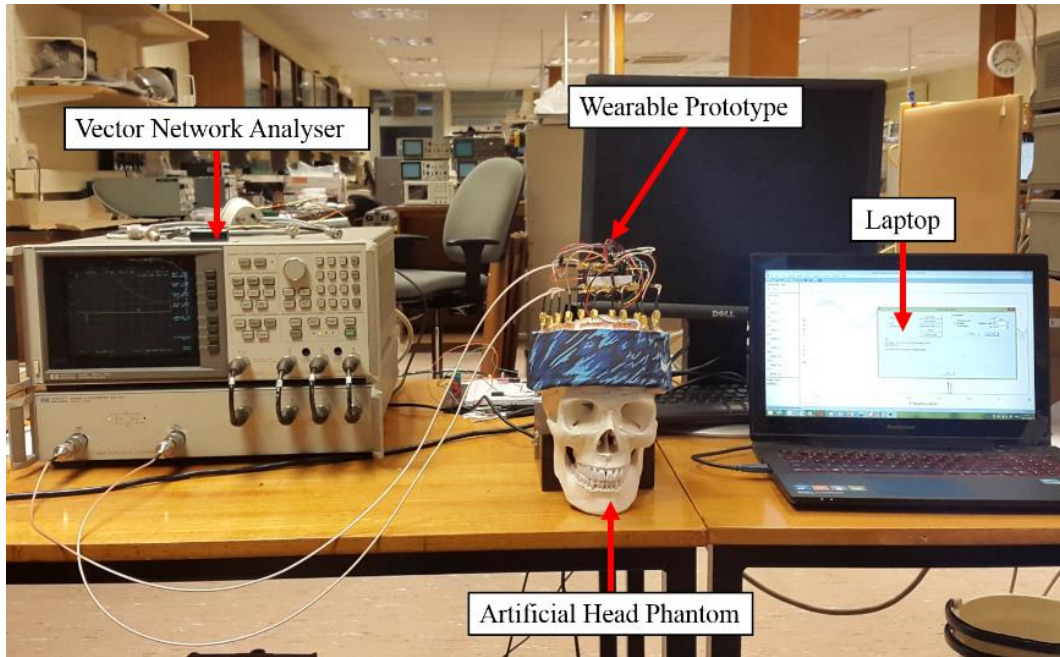


Figure 6.11: Measurement setup for stroke detection using artificial head phantom

previous chapters. Figure 6.9 and Figure 6.10 display the two main prototypes of the wearable devices developed from array of antennas and the proposed RF switching circuit. The measurement setup for the wearable devices is illustrated in Figure 6.11. It consists of the wearable device prototype, a head phantom, a VNA and a laptop.

6.3.1 Realistically Shaped Human Head Phantom using Low Cost Materials

The artificial head phantom developed in this section follows the recipes presented in [29] where slight modification has been made to the ratio of the mixture due to the use of tap water instead of distilled water. This is due to higher conductivity of tap water compared to distilled water. A commercially available skull made from polyvinyl chloride (PVC) is used as a shell for the phantom. The dielectric constant of the skull is approximately 3.1. This hard shell layer is assumed to represent several other head layers which are skin, fat and muscular parts apart from the skull itself [66]. The skull consists of upper and lower parts where the cavity is filled with materials that mimic the properties of the brain tissue. The general procedure used to fabricate the materials is as follows.

1. A measuring jug is first filled with tap water. Then, sugar is added slowly to the solution with continuous stirring to form a thick liquid. The actual amount of the materials used depends on the quantity needed based on the proportions shown in Table 6.1. A small quantity of sodium benzoate is added to protect the phantom from mould. For artificial stroke target, a small quantity of red food colouring paste is added to the solution.
2. Next, the mixture is added with salt to increase the conductivity of the solution if needed. The dielectric probe is used to measure the mixtures to ensure similar properties to that of actual tissues are obtained. The dielectric measurement is conducted at this stage since the mixture is still in liquid state in order to avoid any air gap between the probe and the phantom which could lead to inaccurate measurement results [29].
3. To solidify the solution into a relatively stiff gel, agar is added to the mixture. It is expected that the dielectric constant values of the final product do not vary substantially by adding agar.
4. The solutions are heated to 70-80°C. The heating is kept at that temperature while stirring until it becomes nearly semi-solid. Then, the heating is stopped and the mixture is allowed to cool down for 2 minutes.

The gel like mixture is then poured into the cavities on both parts of the skull. The phantom is put into a freezer overnight to completely solidify the mixture. Figure 6.12 shows the final fabricated head phantom.



Figure 6.12: Fabricated artificial head phantom

A stroke target is inserted into the phantom by creating an equal size cavity in the brain tissue. In the subsequent experiments, the location of the stroke was varied to evaluate efficacy of the detection system.

6.3.2 Artificial Human Head Phantom using Lamb's Brains

The development of head phantom is crucial to mimic the actual human head for testing and validation purposes before going into clinical trial. There are several realistic head phantoms that has been presented in the literature for microwave head imaging [66], [117], [118]. However, these head phantoms were made from artificial ingredients hence might not able to replicate the heterogeneity of an actual brain. For this reason, another phantom has been fabricated by using an actual animal brains. Several lamb brains were used to replace the artificial brain tissue in the previous phantom construction. At first, the electrical properties of the lamb brain were measured using the dielectric probe as illustrated in Figure 6.13. The measurements were made by probing several locations on the lamb brain and the data were averaged.



Figure 6.13: Measurement the electrical properties of lamb brain

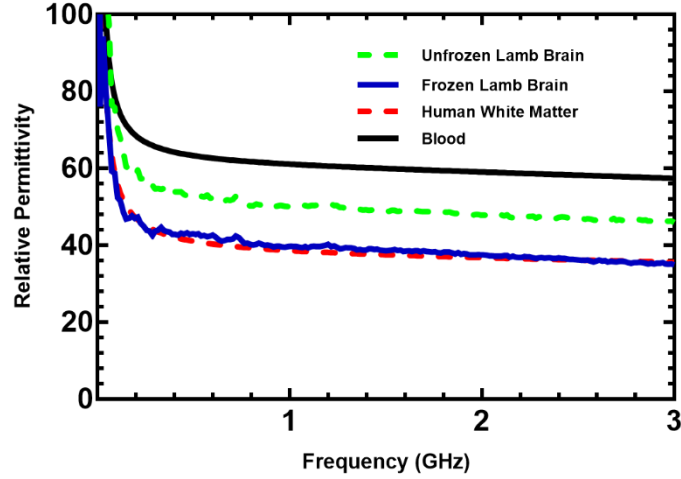


Figure 6.14: Measured dielectric constant of lamb brain

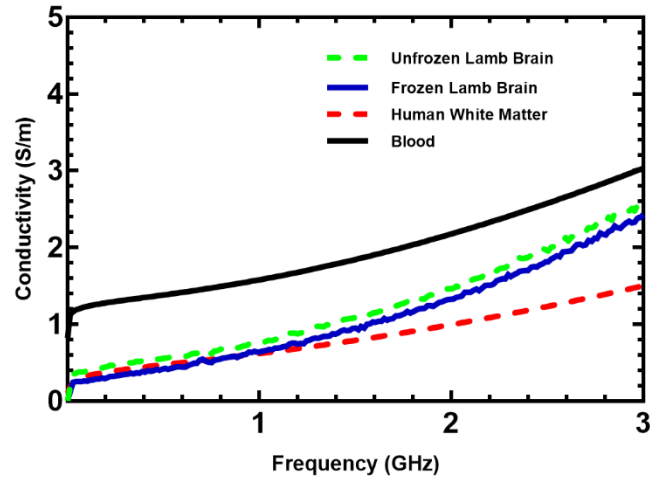


Figure 6.15: Measured conductivity of lamb brain

The measured permittivity of two states of the lamb brains which are frozen and unfrozen were compared to the actual white matter as depicted in Figure 6.14. It can be seen that the permittivity of frozen lamb brain is in agreement with the white matter with variation of less than 5% across the frequency band. As for unfrozen condition, the dielectric constant of the lamb brain increases by around 25%. However, the noticeable increase in the permittivity of unfrozen lamb brain could be due to the existence of water layer between the probe and the brain when the measurement was made since it was done during the defrosting process. As such, the permittivity values taken from the frozen brain should reflect more accurate data. The dielectric contrast

between frozen lamb brain and blood varies from 1.53 at 1GHz to 1.64 at 3GHz. On the other hand, the contrast between unfrozen brain and blood is from 1.21 to 1.25 across the same frequency band.

In addition, the measured conductivity of the brain is given in Figure 6.15. The conductivity increases by around 10% when the brain was defrosted. Both cases show an increase of up to 50% from conductivity of white matter. The higher conductivity of the lamb brain would result more losses to the propagated EM signal hence making the detection of stroke become more challenging. The conductivity ratio between the frozen lamb brain and the blood is from 2.04 to 1.18 over 1GHz to 3GHz frequency range. The fabricated head phantom filled with the lamb brains is illustrated in Figure 6.16.

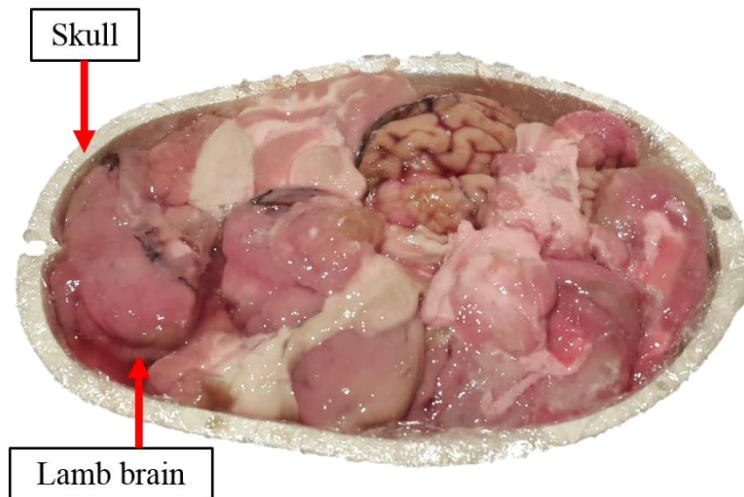


Figure 6.16: Artificial head phantom filled with lamb brain

6.4 Measurements Results and Analysis

6.4.1 Reflection Coefficient Measurements

For measurements using the proposed wearable antenna array, two measurements were carried out with a healthy head (no bleeding) and then with a head

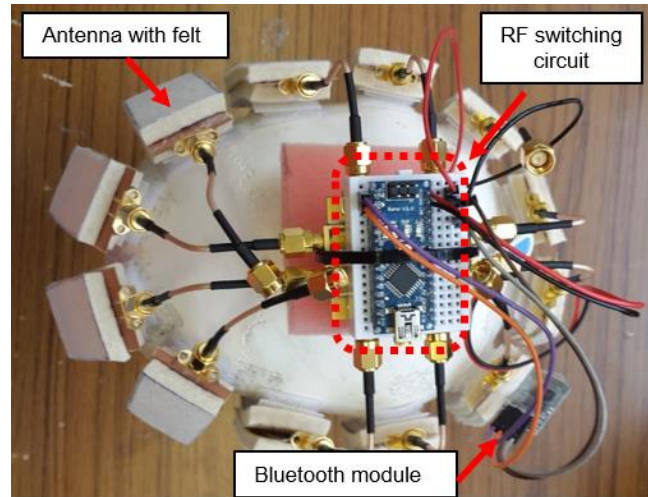


Figure 6.17: Location of the antennas and the switching system (top view)

phantom with a blood clot. The location of the antennas placed on the head phantom is shown in Figure 6.17 where the absorber was removed for clarity. During the measurements, the absorber was attached to the antennas to suppress the back lobe radiation in order to prevent the system from measuring the unwanted surrounding noise. The size of the spherical blood clot placed inside the head phantom is 30mm in diameter corresponds to a volume of 14.14cm^3 as shown in Figure 6.18.

The reflection coefficients of the antennas closer to the blood clot are then compared between these two scenarios. Since there are twelve antennas in the array, twelve reflection coefficient responses were recorded as shown in Figure 6.19 and Figure 6.20 for healthy and unhealthy cases respectively. This method can be viewed

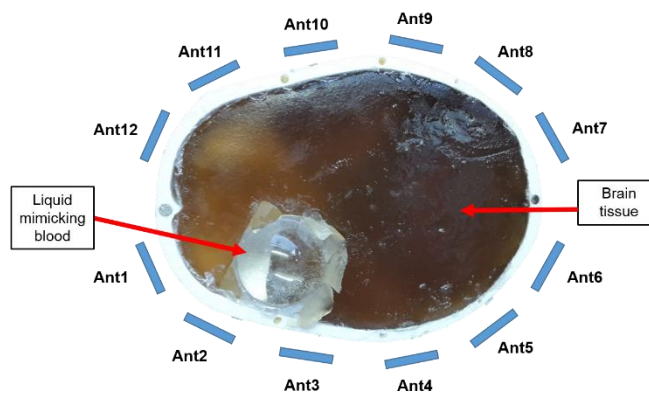


Figure 6.18: Location of the blood clot inside the head phantom

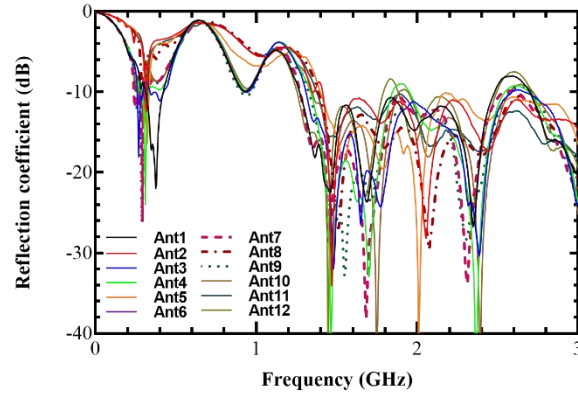


Figure 6.19: Measured reflection coefficient of the antennas with the presence of healthy head phantom

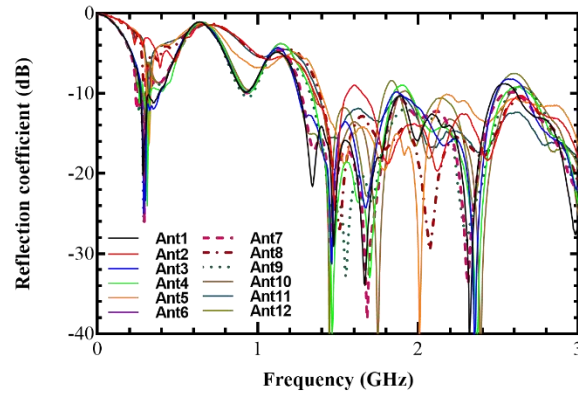


Figure 6.20: Measured reflection coefficient of the antennas with the presence of unhealthy head phantom

as mono-static radar approach where only one antenna is active at a certain time. Based on Figure 6.21, it can be seen that the reflection coefficient values of the three antennas (referred as Ant1, Ant2 and Ant3) which locations were the closest to the spherical target show noticeable differences between healthy and unhealthy head which confirms the finding reported in [15]. This is due to the changes in the dielectric constant of the materials along the propagation path of the signal transmitted and received by those antennas due to the existence of the blood clot. As for the other antennas, their S_{11} responses were not affected since the blood clot was not within their signal propagation paths or their location were too far from the target.

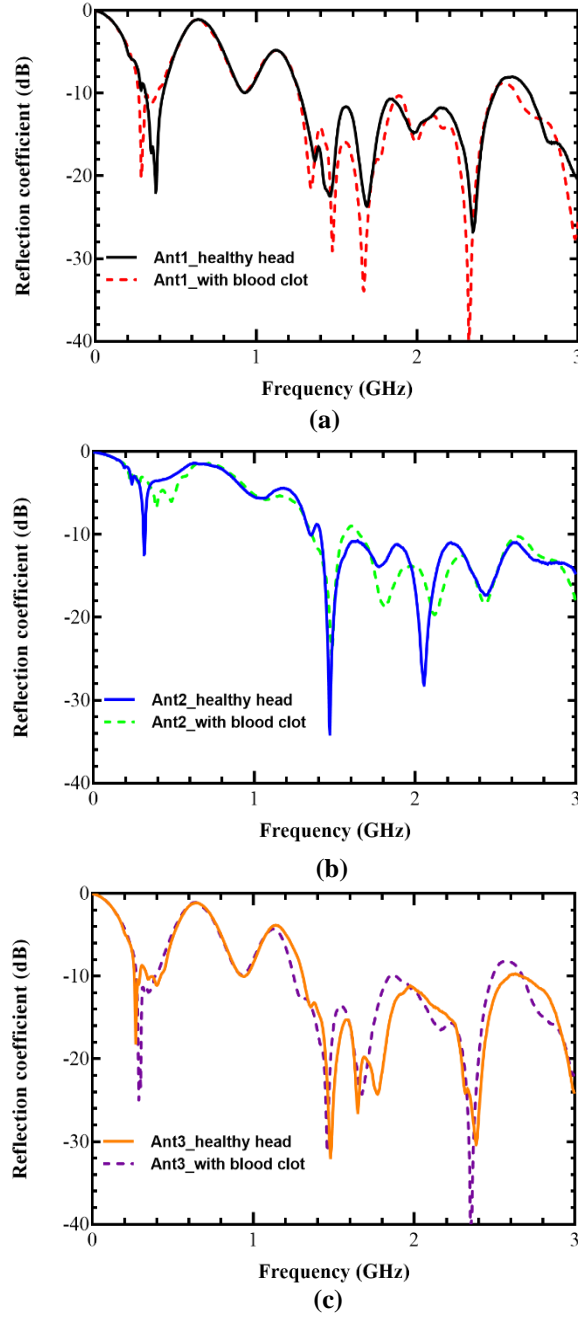


Figure 6.21: Measured reflection coefficient of the antennas with healthy and unhealthy head (a) Ant1 (b) Ant2 (c) Ant3

6.4.2 Transmission Coefficient Measurements

By using four of the antennas from the array as transmitting antennas and the remaining eight antennas as receiving antennas, thirty two transmission coefficient

channels were collected for both scenarios. This method has been implemented in [9], [29] for the detection of subdural hematoma and stroke types where machine learning algorithms were utilised for the classification of the diseases.

In this method, the 1P4T switch is connected to the four transmitting antennas while the remaining eight antennas are connected to the 1P8T switch. The amplitudes of S_{21} were measured for all the 24 communication channel pairs. However, for brevity only S_{21} between antenna 2 (as transmitting antenna) and the eight receiving antennas will be analysed. The measured S_{21} results between antenna 2 and the receiving antennas are plotted in Figure 6.22 and Figure 6.23 for both healthy and unhealthy head conditions. In general, from the S_{21} results, it is concluded that antenna pairs that are further apart have higher insertion loss due to longer path taken by the signal to travel between them. Moreover, the insertion loss also increases with frequency since the head phantom and biological tissues in general have higher loss at higher frequencies.

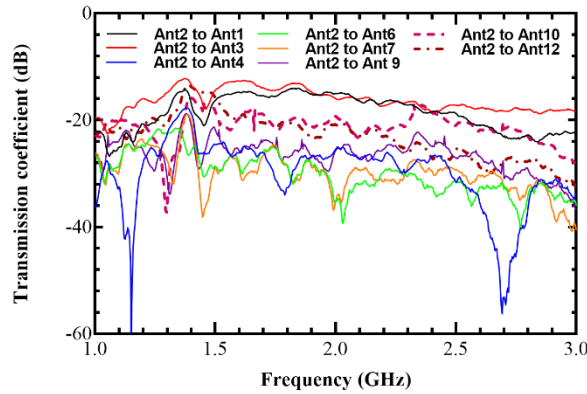


Figure 6.22: Measured transmission coefficients between antenna 2 and the receiving antennas for healthy head phantom

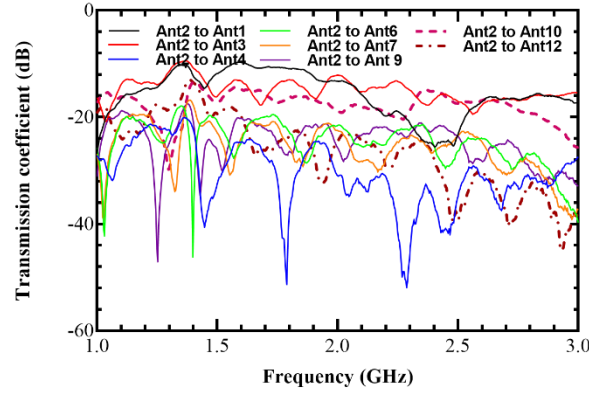


Figure 6.23: Measured transmission coefficients between antenna 2 and the receiving antennas for unhealthy head phantom

To investigate the differences in amplitude of S_{21} between healthy and unhealthy cases, the transmission coefficients for two antenna pairs namely Ant2-Ant1 and Ant2-Ant3 are plotted in Figure 6.24. It can be seen that the insertion loss for Ant2 and Ant1 pair for the unhealthy case is lower than the healthy case between 2 GHz to 2.5 GHz. This could be attributed to the existence of the blood clot in the path of the antenna pair where the higher conductivity of the blood clot compared to the brain tissue causes the transmission path loss to increase. The trend could also be observed for Ant2-Ant3 pair at 1.6 GHz and 2.5 GHz frequency range where the transmission loss is higher for the unhealthy case than the healthy brain due to the formation of the blood clot in its

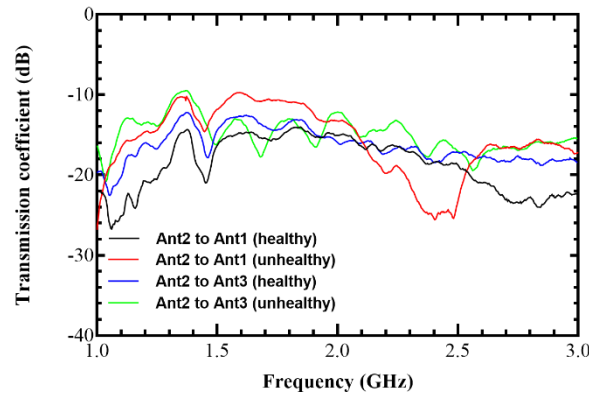


Figure 6.24: Measured transmission coefficients of the antennas with healthy and unhealthy head for antenna 2-antenna 1 and antenna 2-antenna 3

path. By applying advanced post-processing techniques such as machine learning algorithm on the collected transmission path loss data, detection or imaging of potential head diseases such as stroke or traumatic brain injuries could be implemented using this transmission coefficient method.

6.5 Summary

In this chapter, testing and performance validations of the prototype have been described. Initial experiment was conducted to verify the sensitivity of the proposed antenna by using a liquid-based phantom with similar properties to that of real human head. The smallest fabricated artificial stroke target that could be detected is 15.625cm^3 in volume. Based on this finding, further tests have been carried out on a realistically shaped head phantom using the wearable antenna array prototype. The main ingredients of the head phantom are water, sugar, salt and agar. Moreover, another head phantom has been fabricated using lamb's brains which is able to better mimic the heterogeneous human brain. It is found that there is detectable variation in S_{11} signals of the sensing antennas due to the existence of a blood clot inside the artificial human heads. Moreover, in terms of the transmission coefficients of the antennas, it is seen that when the blood clot is located in transmission path of two adjacent antennas, the insertion losses are higher compared to the healthy head. By using the measured S_{11} data from the measurements, the imaging results from the proposed wearable prototypes are presented in Chapter 7 using a confocal algorithm technique.

Chapter 7: Microwave Imaging Results for Stroke Detection

7.1 Introduction

Experiments on realistic-shaped human head phantoms with similar electrical characteristics have been conducted to validate the performance of the proposed wearable interface prototypes for stroke detection applications. It is found that there are detectable differences on the reflection coefficient of the sensing antennas between a healthy head and an unhealthy head. By using this data, an image of the scatterers inside a human head can then be created using a confocal imaging algorithm. In this research, a confocal microwave imaging algorithm called delay and sum technique (CDAS) is applied to the measured data. To adapt CDAS algorithm for the imaging process, a conversion from frequency domain signal to time domain signal on the collected S_{11} data is carried out using inverse Fast Fourier Transform (IFFT) method. To assist the CDAS algorithm, an interpolation technique is proposed to determine the depth of a stroke inside the brain using the received signal strength from the measured S_{11} data. It should be emphasized that differential signals are utilised in this research. A head scan of a healthy head is first taken and then a scan of a head embedded with a stroke. Then, the signals are subtracted in order to get the differential signals which are used as input data for the CDAS algorithm to create an image of the scatterers inside the human head. This method can potentially be applied for real-time monitoring systems or bedside monitoring for stroke patients.

This chapter consists of four main sections. Section 7.2 give an overview of the CDAS algorithm adopted in this research. The differential signal method utilised as part of the calibration procedure for the imaging algorithm is presented in Section 7.3. Afterwards, imaging process of haemorrhagic stroke in simulation environment is described in Section 7.4. In Section 7.5, stroke detection and localisation based on the experimental data described in Chapter 6 are presented.

7.2 Confocal Delay and Sum (CDAS) imaging algorithm

To verify the detection capability of the proposed wearable head imaging system, the widely used imaging algorithm in wideband microwave biomedical systems called confocal delay and sum (CDAS) technique is adapted in this thesis. This method was originally developed for ground penetrating radar applications [1]. A preliminary numerical analysis of CDAS method for breast cancer detection was conducted in [2] to evaluate its efficacy. Promising results were obtained where further experimental studies were carried out to investigate its feasibility [3], [27]. As of now,

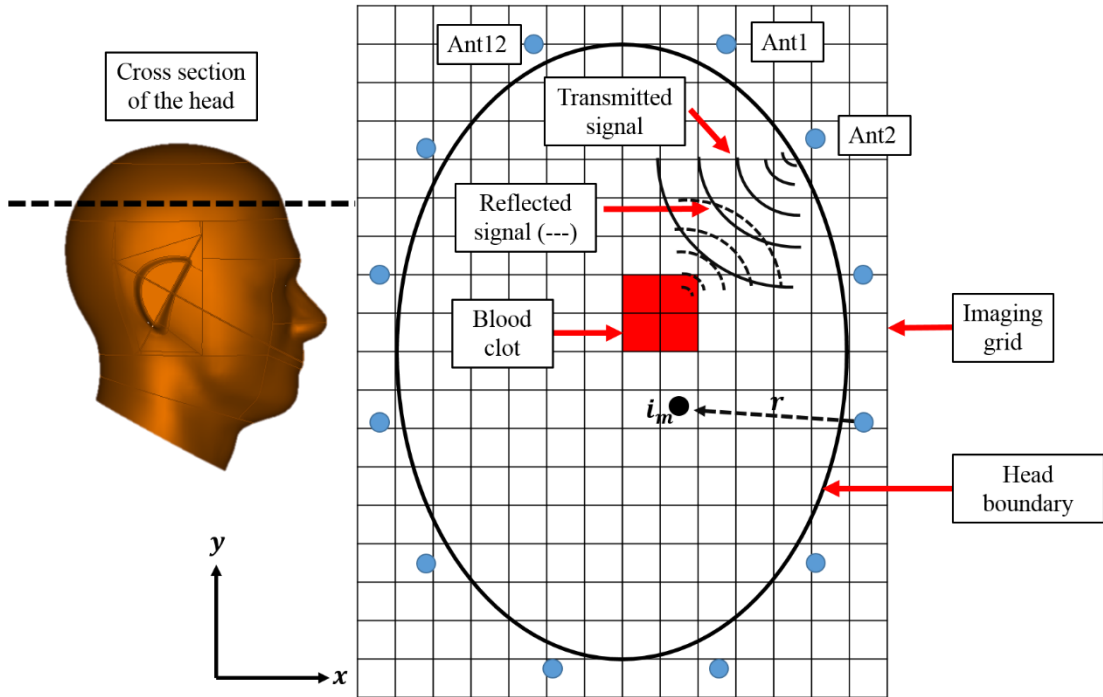


Figure 7.1: Imaging domain of the cross sectional of the head

there are several variations of this method where some modifications have been proposed to improve its detection accuracy and localisation for detection of various diseases ranging from breast cancers to traumatic brain injuries [119].

Consider a 2-D imaging domain of the human head as shown in Figure 7.1. An array of 12 antennas are placed at equal distance between each other surrounding the head. The positions of each of the antennas represented in Cartesian coordinate are given by

$$a_n = [x_n, y_n] \quad (7.1)$$

where n is the number of the n th antenna. The imaging area inside the head is represented by I , where the imaging points inside it are denoted as

$$i_m = [x_m, y_m] \quad (7.2)$$

where m is the number of the m th point in the imaging area.

The propagation time of the signal from the n th antenna in the array to the m th point in the imaging area, I is calculated based on the Equation (7.3) [57]

$$\tau_n(i_m) = \left\{ \frac{\sqrt{(x_n - x_m)^2 + (y_n - y_m)^2} \sqrt{\epsilon_{eff}}}{c} \right\} \quad (7.3)$$

where ϵ_{eff} is the effective dielectric constant of the head. For this research, the value of ϵ_{eff} is 40 which is the average measured dielectric constant values of the artificial brains.

Then, the intensity value at the imaging point, i_m is defined as [57]

$$I(i_m) = \left| \sum_n A_n (2(\tau_n(i_m))) \right|^4 \quad (7.4)$$

where A_n is the signal of the antenna at location n .

7.3 Differential Signals Method

For the imaging process using the wearable head devices, differential signals method is utilised for the calibration purposes [16]. It has been shown in Chapter 4 that the antennas in the array have different responses among them making it impossible to use the averaging method or neighbouring antenna subtraction for the calibration step without invalidating the accuracy and detection capability of the system [120]. To obtain the differential signals, head scans without and with the haemorrhagic stroke are carried out. The signals for both cases are then subtracted to create the differential signals where they are input into the imaging algorithm. This method will be useful in detecting the formation of stroke where it is able to compare the S_{11} variation over time particularly for monitoring purposes. Throughout the thesis, the differential signals will be used for the imaging process. In addition, any unwanted

effects due to reflections from the surroundings and the RF switching circuit that are present in both signals will be cancelled out.

7.4 Image Reconstruction of a Head Phantom with Haemorrhagic Stroke in Simulation Environment

Using the confocal algorithm explained earlier, the performance of the wearable antenna system is investigated via electromagnetic simulation. 12 antennas were positioned around the human head model as shown in Figure 7.2. The distance between adjacent antennas was kept constant. A Gaussian pulse of bandwidth 1.5GHz (1.5GHz to 3GHz) was generated and transmitted into the head by the each of the antenna in the array. The Gaussian-modulated sinusoidal pulse's width corresponds to the frequency bandwidth of the trapezoidal shaped antenna is given by Equation (7.5) [58]

$$V(t) = \sin[2\pi f_0(t - t_0)e^{-(t-t_0)^2/2\tau^2}] \quad (7.5)$$

where f_0 is the centre frequency at 2.25GHz, $t_0 = 5\tau$, and $\tau = 0.4ns$. In mono-static radar approach, the same antenna acts as the transmitter and the receiver. Hence, in this case, the same antenna will collect the reflected signal.

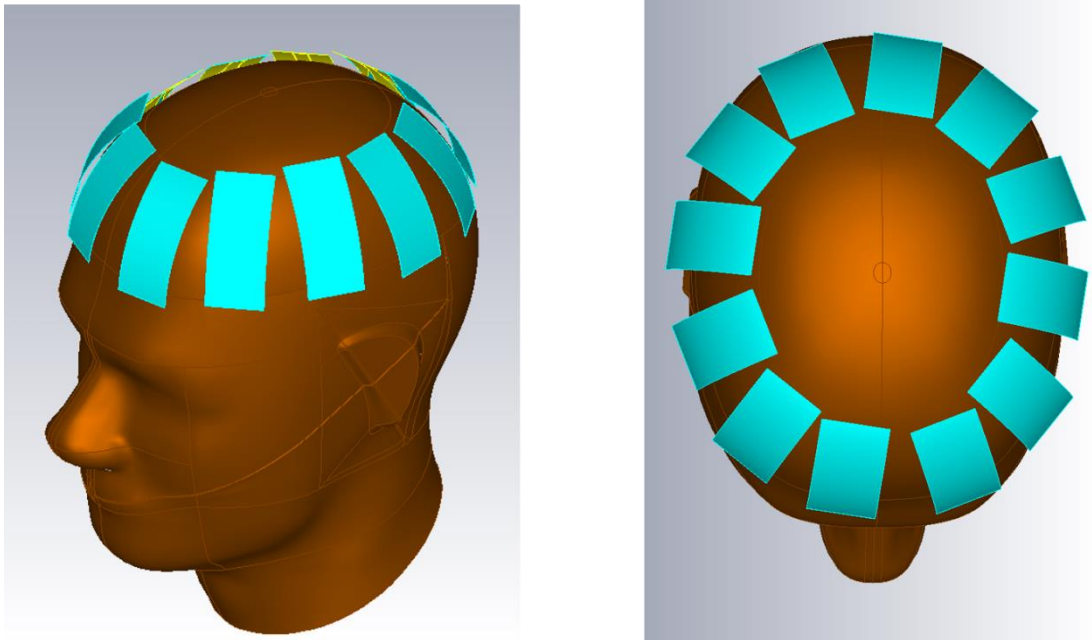
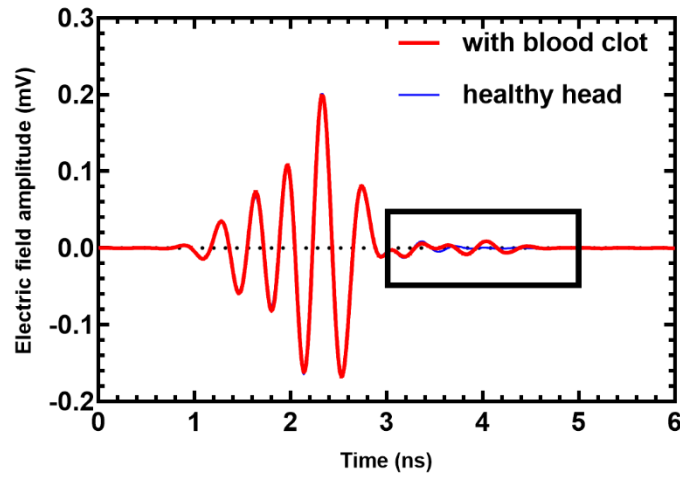
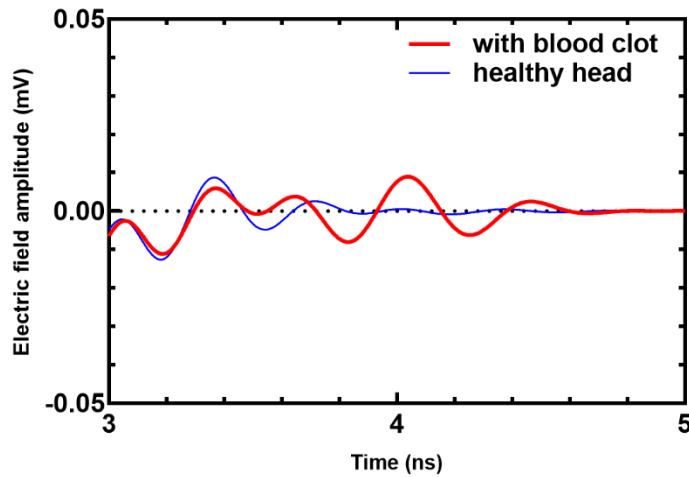


Figure 7.2: Placement of antenna array on the artificial head phantom in the simulation

First, each of the antennas in the array transmitted a Gaussian pulse into the head without stroke to represent a healthy head. All twelve time domain responses for healthy case were collected. Next, a cubic target of size $25\text{mm} \times 25\text{mm} \times 25\text{mm}$ was inserted into the head to mimic a haemorrhagic stroke. It is to be noted that the size of the target was selected since it is the smallest target that the antennas can detect based on the experiments conducted in Chapter 6. Moreover, it is found that a volume of the blood clot of less than 30cm^3 can potentially increase the survival rate of a patient suffering from stroke [121]. The properties of the target are assigned with the electrical



(a)



(b)

Figure 7.3: Time domain response for Ant1. (a) Reflection from the stroke (b) Close up signal

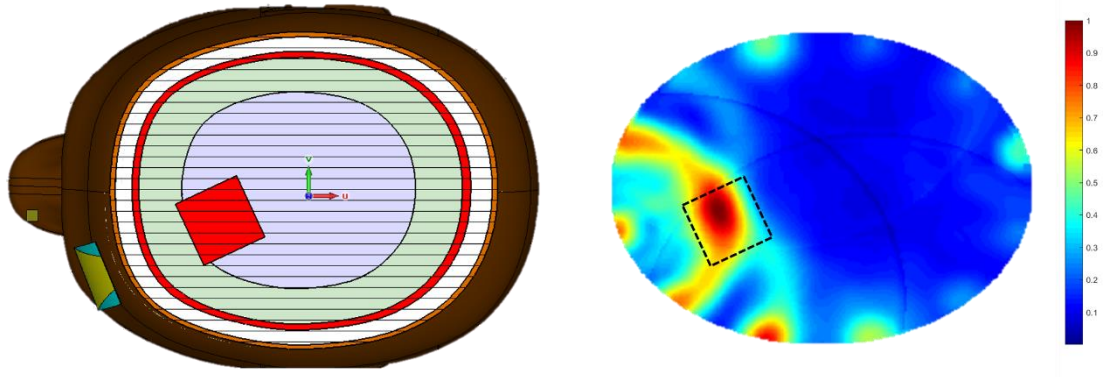


Figure 7.4: (a) Location of the stroke inside the head phantom, (b) reconstructed image of the head model with a blood clot indicated by the dashed black rectangle shape.

properties of blood. Twelve time domain responses for unhealthy case were then acquired.

The time domain responses for Ant1 that was the closest antenna to the stroke for healthy and unhealthy cases are shown in Figure 7.3. It can be seen that there is a small reflected pulse from 3ns to 5ns for the unhealthy case which is due to reflection from the stroke. For healthy case, there is no obvious reflection seen on the time domain response. Based on the ϵ_{eff} of 42 which represents the average dielectric constant of the head used in the simulation and the distance of the stroke from the antenna, the calculated round trip delay of the transmitted pulse is 3.4ns corresponds to a time inside the time window of the observed reflected pulse in the result. Based on the simulation data, the 2-D image of the head created using the confocal algorithm was generated as illustrated in Figure 7.4 based on the responses from all twelve antennas. It is seen that the reconstructed image is able to show the approximate location of the stroke represented by the dashed black square. Furthermore, the imaging result confirms that a stroke inside the head phantom could be detected with sensible accuracy by using only 12 antenna elements in the array.

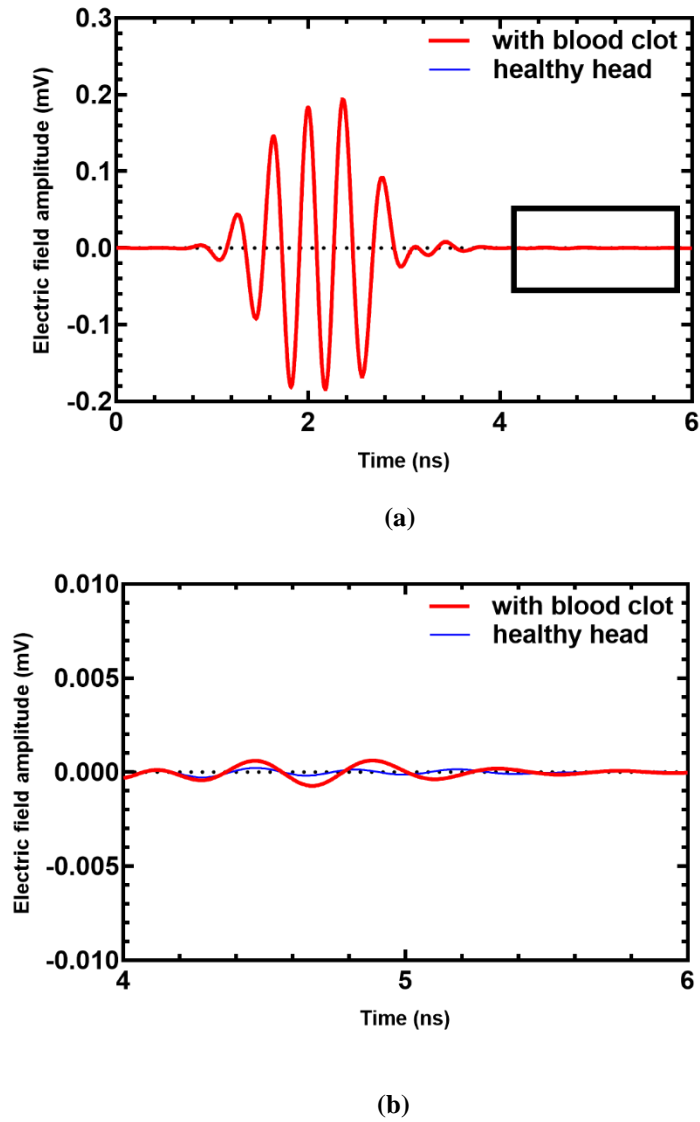


Figure 7.5: Time domain response for Ant3. (a) Reflection from the stroke (b) Close up signal

Another simulation was conducted where a blood clot was embedded slightly deeper inside the brain. Again, a small reflection is observed at 5ns as illustrated in Figure 7.5 although the reflected pulse's strength is weaker than the previous case considering that the distance is larger in this case. The reconstructed image is given in Figure 7.6 which further confirms the detection and localisation of the stroke formation inside the head.

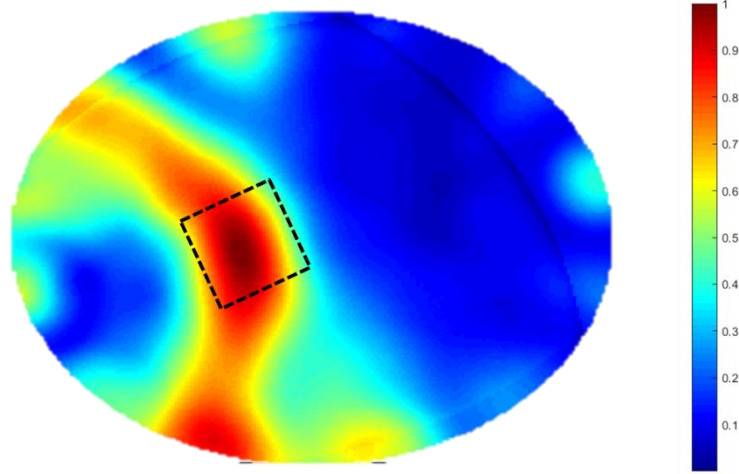


Figure 7.6: Reconstructed image of the head model with a blood clot indicated by the dashed black rectangle shape.

7.5 Image Reconstruction of Head Phantom with Haemorrhagic Stroke using Measurement Results

In the experiments, the measurements were carried out in the frequency domain using a vector network analyser rather than in time domain. As such, to adapt the CDAS algorithm, the S_{11} data must be converted to the time domain [3], [119]. The inverse Fourier transform is implemented for the conversion from frequency domain to time domain. Then, the signals are calibrated by subtracting the signal received at the antennas with and without the stroke target to create the differential signals.

After the conversion of the S_{11} data from the frequency domain to time domain, the recreated pulse is then shifted to the time window that represents the location of the stroke. Considering that a detection of stroke or any internal bleeding inside the head using mono-static method causes a change of S_{11} response of the sensing antenna, the difference in variation of the S_{11} data to the reference signal (no target present) correlates to the distance of the stroke inside the head phantom based on the experiments conducted. It is found that for the same stroke target's size, the average magnitude of the S_{11} data reduced by $1/d^4$ where d is the distance from the antenna to

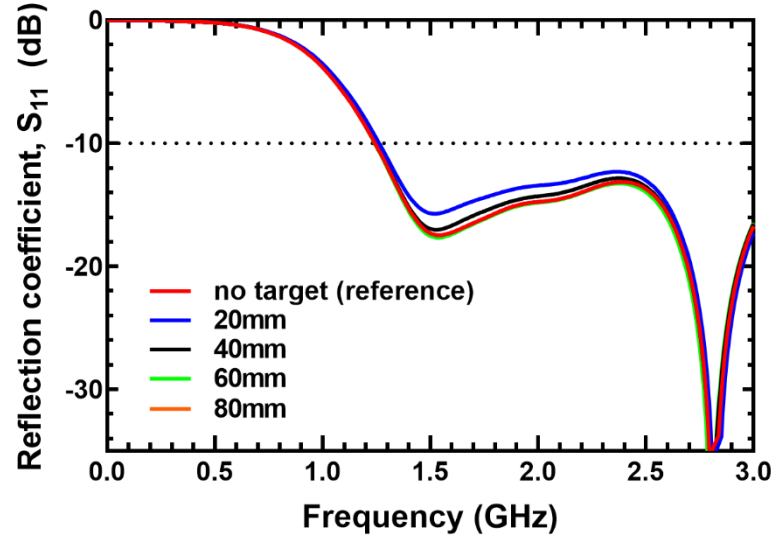


Figure 7.7: Simulated reflection coefficient of the antenna for various stroke depths

the stroke. To verify this finding, a simulation using a realistic head phantom as shown was carried out using CST Microwave Studio. Figure 7.7 demonstrates that S_{11} response of the probing antenna for a shallow stroke has higher difference in S_{11} over the reference signal compared to deeper stroke location. The magnitudes, $|\Gamma|$ of S_{11} data in decibels were calculated and averaged over the number of frequency points used across the operating frequency band of the antenna. The difference of the magnitude against the distance of the stroke from the antenna is illustrated in Figure 7.8. The data was compared to several plots to find the best fit. An inverse fourth power

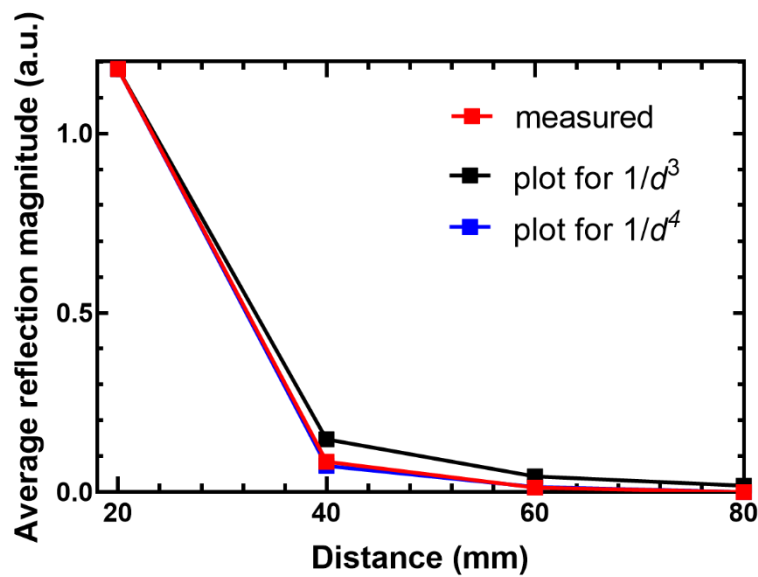


Figure 7.8: Average reflection magnitude over stroke depth

of distance plot which shows a close match with the simulated data. It is concluded that the magnitude of the signal is reduced by approximately $1/d^4$ similar to the one obtained in the experiments. This can be explained by the region of which the antenna operates where at the radiating near field, the E-field and the H-field strength reduces with distance by $1/d^2$ hence the power density attenuated by $1/d^4$ [91]. By using this information, an interpolation technique can be applied to determine the delay for the synthetic pulse created from the IFFT conversion. This step is applied to the measurement results to reconstruct the image of the artificial head phantom. In summary, the overall steps of the imaging process is illustrated in Figure 7.9.

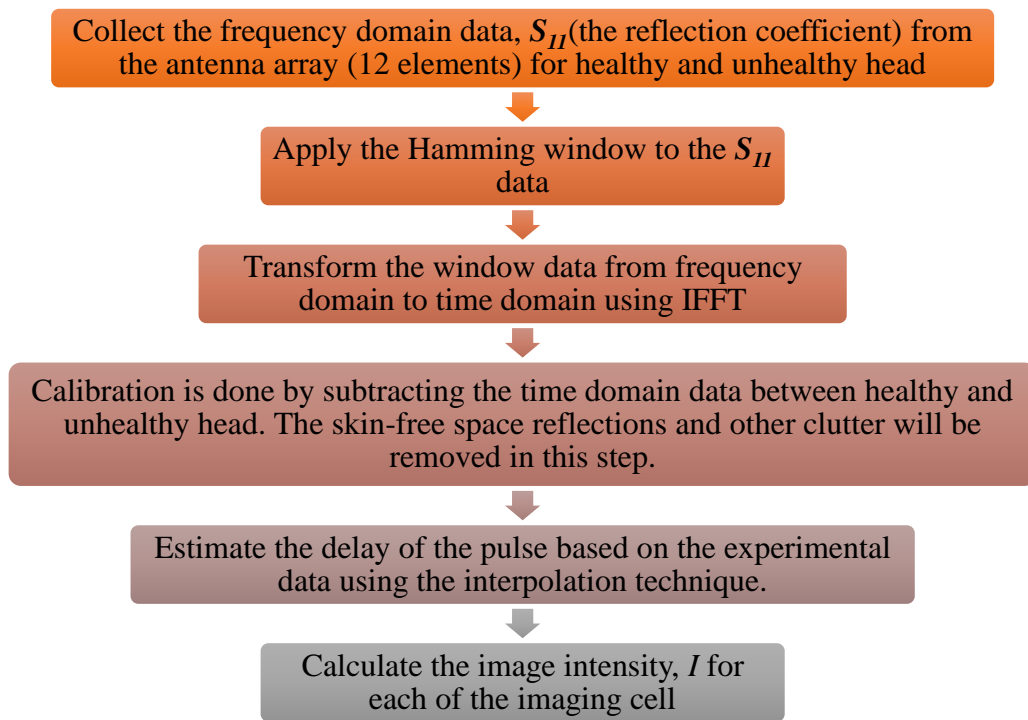


Figure 7.9: Imaging process using measured S_{11} data

After the conversion from frequency domain and to time domain and by applying the proposed interpolation method to estimate the delay of the synthetic pulse, the 2-D image of the head phantom with haemorrhagic stroke as shown in Figure 7.10 can be produced by applying the CDAS imaging algorithm. The measured data used to create this image were acquired using the absorber based prototype with the trapezoidal shaped antennas. The actual position of the stroke is given by the black circle mark on the image. Based on the reconstructed image, it is seen that the wearable device is able to detect the location of the stroke although it shows a bit larger target size than the original. This can be attributed to the number of the antennas used in the array and the bandwidth of the operating frequency band of the antenna where it can be improved using more antennas in the array.

Afterwards, the fully textile antenna array implemented as strap-based prototype was used to scan the phantom filled with brain lambs. The blood clot was embedded at two different positions inside the brain indicated by the black rectangle as exhibited in Figure 7.11. Again, the wearable prototype was able to successfully detect the locations of the stroke inside the artificial head phantom with sensible accuracy. However, due to the lower frequency bandwidth of the elliptical shaped monopole antenna, the target appears to be larger than the one imaged using the

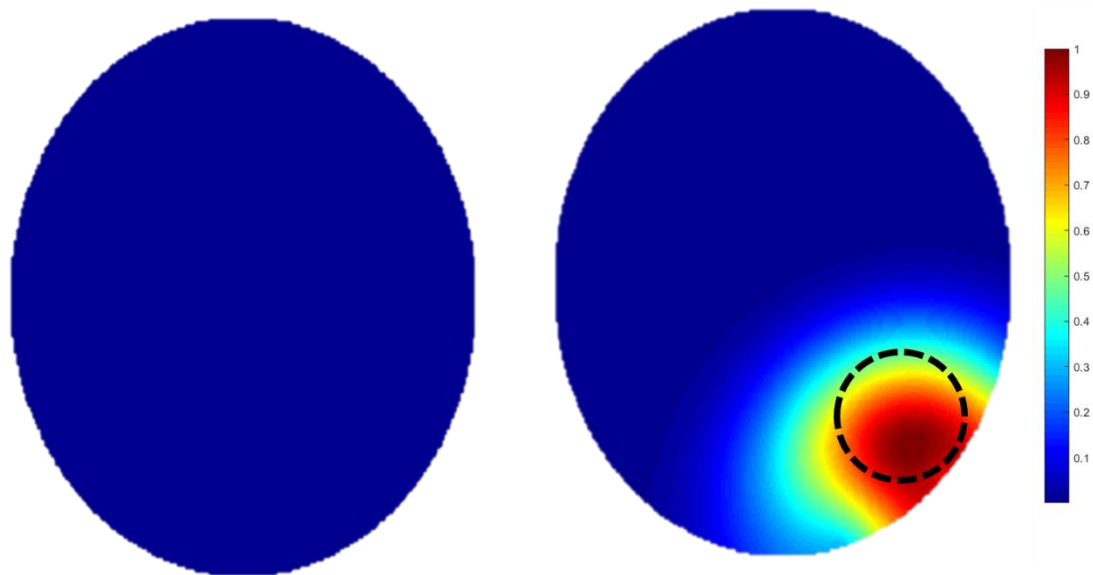


Figure 7.10: The reconstructed image using the first prototype on an artificial head phantom.

(a) Healthy head and (b) Head with a stroke (indicated by the black circle)

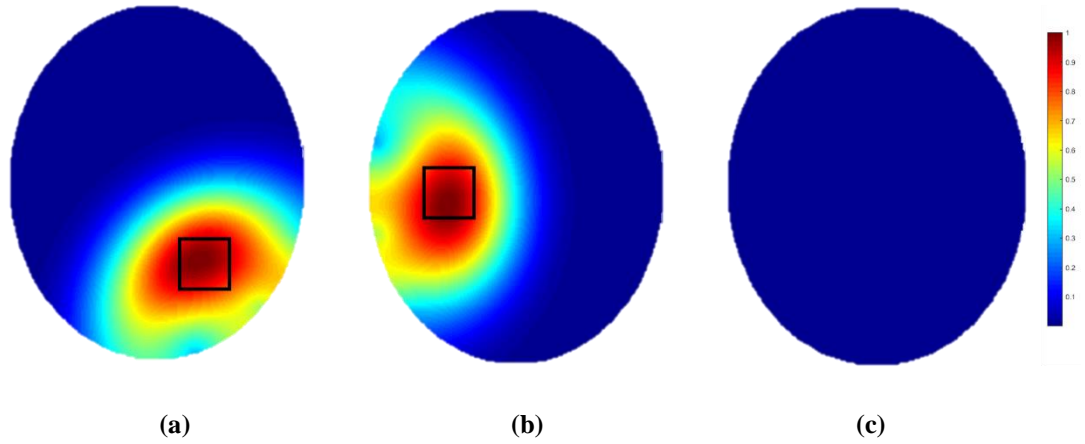


Figure 7.11: Imaging results for (a) stroke location 1, (b) stroke location 2 and (c) healthy brain scenario using the strap based prototype on lamb brain phantom

trapezoidal antenna. It is concluded that the frequency bandwidth of the antenna corresponds to the width of the synthetic pulse after performing the IFFT making the imaged target response to be larger than its actual size.

As a comparison, another measurement was done using the trapezoidal antenna on the phantom filled with the lamb brains. For the same blood clot location, the

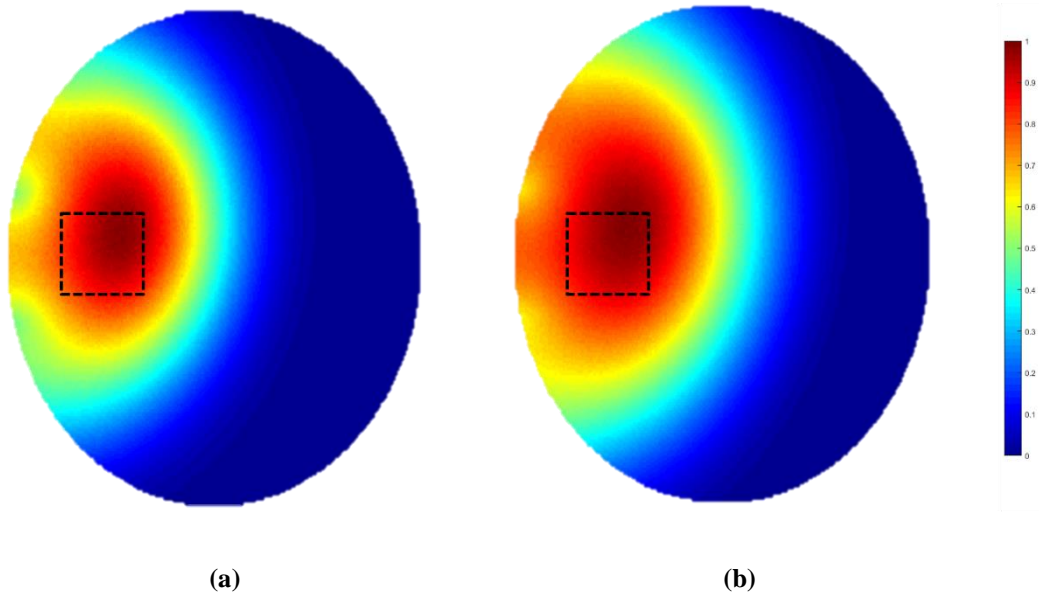


Figure 7.12: Imaging results for (a) trapezoidal monopole antenna prototype, (b) textile based prototype and (c) on lamb brain phantom

reconstructed images by both prototypes are shown in Figure 7.12. It is seen that both prototypes were able to show the location of the blood clot. However, the size of the target produced by the textile antenna array is larger than the trapezoidal antennas due to its lower bandwidth.

One of the limitations of the proposed interpolation technique is that it mainly depends on the difference in magnitude of the S_{11} response between a reference signal (healthy condition) and the signal of unhealthy head (with blood clot) to estimate the depth of the stroke. However, the S_{11} response when a blood clot is formed inside the head may not be similar between two different patients due to their different head shape and thickness of brain tissue layers. This could lead to inaccurate estimation of the pulse delay making the localisation of the bleeding inaccurate. Nevertheless, it can be improved by collecting data from different stroke patients where a database can be created and used when performing the interpolation step [122]. Furthermore, the database can also be improved to include the effects of different sizes of stroke towards the S_{11} response where a combination of both can provide accurate estimations for both the distance and the size of the stroke or any blood clot formed in the brain. It is seen that in the current confocal imaging algorithm, the size of the stroke in the reconstructed image depends on the width of the recreated pulse and the number of the antennas used in the array. However, a smaller pulse width requires higher bandwidth where this can be very challenging for microwave head imaging considering that frequency above 3GHz is not effective in providing sufficient penetration depth inside the human head. Since the imaging algorithm utilises the differential signals, the formations of clutter does not exist in the image. All the unwanted reflections from the surroundings and the switching circuit have been successfully removed during the calibration process. In addition, it is important to ensure that the antennas are placed at the same positions when two successive scans are made to assist with the calibration process.

Table 7.1

THE PERFORMANCE OF THE HEAD IMAGING SYSTEMS ARE COMPARED IN TERMS OF ITS ADVANTAGES AND LIMITATIONS.

System	Antenna type/ Number of antenna	Operating frequency (Hz)	Accuracy, $\Delta = \ pm - c\ $	Advantages	Limitations	Potential applications
[11]	Vivaldi/16 & 32 antennas	1GHz to 4GHz	1mm/0.7mm	High gain antenna	High profile and bulky	Static haemorrhage stroke detection
[28]	Folded Dipole/32 positions around the head using 1 antenna	1.1GHz to 3.4GHz	-	Directional antenna and compact	Rigid structure	Portable traumatic brain injury detection
[32]	3D slot rotated antenna/18 positions around the head using 1 antenna	1.41GHz to 3.57GHz	-	Directional antenna and compact	Rigid structure	Portable haemorrhage stroke detection
[12]	3-D folded dipole antenna	1GHz to 2.4GHz	1.43 mm	Directional antenna and compact	Rigid structure	On-site rapid diagnosis of intracranial hematoma
Proposed prototype	Flexible monopole antennas/12 antennas	1.5GHz to 3GHz	10mm	Flexible structure, light weight and compact	Bi-directional	Wearable real-time head monitoring

As a comparison, the performance of the wearable head imaging system is compared to similar radar-based head imaging systems in the literature as tabulated in Table 7.1. The performances of the wearable head imaging system are compared in terms of its advantages and limitations. It is shown that the accuracy of the proposed wearable head imaging system are comparable to other systems in the literature although it might not give the best accuracy considering the least number of antennas

used in the system. Additionally, the reconstructed images from proposed system do not show noticeable clutters due to the use of differential signals method. It is expected that the wearable system is able to be used for frequent scanning or real-time monitoring for high risk patient or personnel in various fields.

7.6 Summary

In this section, a confocal imaging algorithm has been applied to the wearable microwave head imaging devices to verify their performances to detect haemorrhagic stroke inside the human head. The imaging algorithm has been implemented for both simulations and experiments. For experiments, additional steps have been carried out to adapt the measured S_{11} data to the image reconstruction algorithm using the classical confocal delay-and-sum technique. The first step is to convert the reflection coefficient of the antenna from frequency domain to time domain to recreate the propagating pulse. Next, an interpolation method has been proposed by using the relationship between the measured average differences in magnitudes of the S_{11} data over the stroke's distance from the antenna based on the experimental data. By interpolating the measured S_{11} data, the estimated delay of the pulse is obtained and used in the imaging process. It have been shown that the proposed interpolation step manages to reconstruct the image of the head to indicate the location of the stroke with sensible accuracy.

Chapter 8: Conclusion and Future Work

This thesis presents the development and implementation of wearable head imaging devices for bio-medical applications with verification on detection of haemorrhagic stroke inside an artificial human head. This chapter summarises the research studies presented in this thesis. The main objectives of each chapter are reviewed and the achievements from the studies conducted are highlighted. Future directions based on the research presented in this thesis are suggested. This chapter is organised as follows. Section 8.2 summarises the conclusion of each chapter in this thesis. The main contributions arising from this research are described in Section 8.3. Section 8.4 proposes future developments based on the study and finally, Section 8.4 concludes the chapter.

8.1 Chapter Summary and Conclusion

Chapter 2 presents the literature review in the field of microwave medical imaging emphasizing on the implementation of the microwave system on breast cancer detection and diagnosis of the human head. The fundamental principle behinds radar-based microwave imaging is that malignant tissues or blood in the body would scatter more energy when illuminated with electromagnetic wave. Due to the reflected signals, the sensing antennas can detect the presence of tumours inside the breast or the formation of blood clot inside the brain by measuring the reflected signals. By applying suitable imaging or sensing algorithms, the location of the tumours or blood clot can be determined with sensible accuracy. For head imaging applications, several research have been carried out to verify the effectiveness of the microwave technology in detecting or classifying different head diseases such as stroke, traumatic brain injuries and intracranial hematoma. In addition, a classifier system has been proposed to detect the type of stroke suffered by a patient in order to deliver the right treatment. Afterwards, a wearable concept of using flexible antenna array as sensing element is described. The proposed wearable device offers many advantages such as it can be directly mounted on the head, provide comfort to the wearer, light weight and low cost.

This sensors can be used for several testing setups ranging from static systems, portable and real-time wearable monitoring systems.

The most vital component in any microwave imaging system is the sensing antenna. There are several main requirements in the implementation of a flexible antenna for microwave head imaging applications. In addition to typical requirements of a rigid sensing antenna, flexibility and light weight are some of the key features to ensure successful employment of wearable devices. In Chapter 3, the design aspects of the flexible antenna are described and verified. Several flexible materials namely flexible FR-4, PET and textile have been used to fabricate the antennas where their performances are validated in terms of impedance matching, radiation pattern and fidelity of the transmitted pulse. There are two main designs of the antenna namely trapezoidal monopole and elliptical monopole antennas. Planar monopole design is adopted in this research due to its inherent low profile and wideband characteristics. Parametric optimisations are carried out mainly on the feeding lines of the antennas to optimise their impedance bandwidths. The antennas are prototyped and measured. The measured frequency of the trapezoidal monopole antenna is from 1.34GHz up to 3GHz whereas the textile-based elliptical antenna operates at 1.3GHz to 2.76GHz. Based on the simulations conducted, both antennas show high fidelity factor that ensures low signal distortion. Moreover, the performances of the antennas when operate in close proximity to a fabricated realistic head phantom are investigated to confirm that their performances are not affected by the presence of the head. It is found that the performances of the antennas are maintained when operate in close proximity to the artificial head phantom.

Chapter 4 describes the development of the wearable prototypes by using an array of the antennas designed in Chapter 3. Based on a typical size of human head, the number of antenna elements in the array is restricted to twelve due to the antenna dimensions as well as to ensure sufficient separation between adjacent antennas to reduce the mutual coupling effect. To investigate the effectiveness of using twelve elements array for head imaging, extensive simulations are carried out to investigate the spatial power distribution inside a head model. It is observed that all areas of the head at the cross-section 40mm below the head crown, are covered by the antennas.

The first prototype is developed by using an array of twelve flexible sensing antennas and a flexible absorbing material backed with flexible conductive sheet to suppress the back lobe radiation of the monopole antennas. Additionally, the absorber also serves as a support structure to mount the antennas. Owing to the strong coupling between the sensing antenna and the head, it is found that a minimum distance of only 25mm is required between a reflector and the antenna compared to 50mm needed in free-space condition at 1.5GHz. Low measured mutual coupling is observed between adjacent antennas in the array. However, due to the limitation of the first prototype with its fixed size and slightly rigid structure, a strap-based configuration is developed as a second prototype. This prototype incorporates mainly textile materials to provide better flexibility and integration with clothing head garments in the future. The prototype can be fitted on different sizes of human head. However, a trade-off is made where the omission of the absorber could lead to unwanted radiations towards the sensing antennas.

In Chapter 5, design and development of RF switching circuits aimed for integration with the proposed wearable prototypes are described. One of the main challenges in realising a wearable device for head imaging is to build an integrated sensing system where a unification of sensing elements, a switching network and a transceiver is required. In order to progress towards this objective, an integration of the antenna arrays and a switching circuit is realised. By using off-the-shelf components, a compact and low-cost switching circuit is developed. The switching circuit is made from an Arduino Nano board, two RF switches and Blue-tooth module to provide switching mechanism for the proposed flexible array. Further improvement has been made to the switching circuit by fabricating the components on a single board. The fabricated switching board can be configured to measure the reflection and the transmission coefficients of the antennas.

The accuracy and sensitivity of microwave imaging systems mainly depend on the efficiency of their sensing antennas. To test the sensitivity of the proposed antenna, extensive experiments have been carried out on several types of head phantoms as described in Chapter 6. Initial experiment is conducted using a liquid based phantom that mimics the electrical properties of a human head. The sensitivity of the proposed

antenna is tested on various sizes of artificial blood target. It is found that the proposed antennas could detect a blood target as small as $25\text{mm} \times 25\text{mm} \times 25\text{mm}^3$. Based on the initial results, the full prototypes are then tested on two realistic shape head phantoms. The initial head phantom is developed using tap water, sugar, salt and agar whereas the second generation head phantom is realised using lamb brains. The use of actual animal brain is to mimic heterogeneous properties of an actual human head which could not be provided by the initial fabricated phantom. Measurements are carried out and the signal are acquired using a VNA.

The imaging process is explained in Chapter 7 using a modified confocal algorithm. One of the main problems of adopting confocal delay-and-sum algorithm is to determine the accurate dielectric constant value to be used in the algorithm. It is found that different values of permittivity assumed in the algorithm would lead to inaccurate estimation of the stroke or blood clot location inside the head. In addition, the employment of antenna array prevents the use of averaging during the calibration step as the variations of antenna responses could mask any detection of a blood clot. Hence to mitigate this issue, differential signal method is used in view of applying the proposed wearable device for head monitoring purposes. Moreover, since S_{11} signal conversion from the frequency domain to the time domain is required in order to apply the CDAS algorithm, a new interpolation technique is proposed based on the S_{11} signal strength variations with the stroke depths. Good estimation of the location of the blood clot inside the brain is achieved using the proposed technique.

Overall, it is concluded that wearable devices for head medical imaging applications can be achieved by using flexible antenna array and a compact RF switching circuit. Therefore, it is possible to integrate the proposed wearable device with different microwave imaging setups including static scanning tools in the hospital and a fully wearable health monitoring system integrated with a compact standalone transceiver device for home or real-time monitoring systems in the future.

8.2 Summary of Contributions

This section summarises the challenges in designing and implementing wearable sensing devices for microwave head imaging systems and the key contributions that have been proposed to address these challenges. Overall, the research areas in this thesis include antenna design, wearable array configuration, RF switching circuit, verification of the detection capability of the proposed device on realistic artificial head phantoms, and imaging process using confocal algorithm which are described as follows.

8.2.1 Compact and Flexible Antenna Design

The main contribution of this section is the use of flexible materials for the sensing antenna for microwave head imaging applications. Most of the existing radar-based microwave head imaging systems use rigid antenna substrate which restricts their use for wearable applications. To provide better testing or monitoring procedure for a patient, a flexible and wearable antenna design is required. Several flexible materials have been utilised to fabricate the sensing antennas namely thin and flexible FR-4, PET and textile. The antenna types proposed in this thesis are two variations of monopole antennas which are trapezoidal and elliptical monopoles which have been optimised to operate at frequency range of 1.5GHz to 3GHz in view of providing sufficient penetration depth inside the human head.

8.2.2 Prototypes of Wearable Antenna Array

To develop a wearable device using the flexible antennas, two array configurations have been developed. In the first prototype, an absorbing material with flexible conductive sheet is used to suppress the unwanted radiations coming from the surrounding to improve the performance of the sensing antenna array. A part from that, the absorber which has been shaped to fit an artificial head phantom also acts as the mounting base for the antennas. The final structure forms a wearable sensing device where it could be potentially used to replace the typical rigid antennas in the existing radar-based microwave imaging systems. Due to fixed size of the first prototype, the device needs to be custom built to fit for each individual head size. As an improvement on the first prototype, a strap-based configuration is proposed using a head band as the

supporting structure to hold the antennas. Although the suppression of the back lobe radiation of the antenna has to be compromised, this new prototype gives better flexibility to fit different sizes of human heads.

8.2.3 Low cost and Compact RF Switching Circuit for Microwave Head Imaging

This research also develops a low cost and compact switching circuit for integration with the proposed wearable sensing devices for head imaging systems. The implementation of the switching circuit is first accomplished using off-the-shelf components. With the proposed circuit, a switching mechanism can be established on the wearable device to select any antenna in the array. Moreover, the switching process can be done wirelessly via Bluetooth connection using an Android phone. Subsequently, a new prototype has been developed using the same components from the initial design on a single board using 6-layer PCB technology. A wideband Microstrip-to-Microstrip transition is introduced in the integrated circuit to route the RF signals from the input ports to the antennas' port. This new circuit configuration is able to reduce the overall size of the wearable device.

8.2.4 Performance Verification of the Wearable Prototypes on a Realistic Head Phantom

One of the challenges to validate the performance of microwave head imaging systems is to test the device on a realistic head phantom before going for clinical trials. In this thesis, two different realistic shaped head phantoms have been fabricated for testing. The first variation of the head phantom has been built using a mixture of tap water, sugar, salt and agar to represent the human brain. The homogenous characteristic of the fabricated artificial brain is not perfectly mimic the actual properties of human head. Owing to this limitation, a new phantom has been fabricated using an actual lamb's brains. It is expected that the heterogeneous feature of the lamb brain would better mimic an actual human brain for the validation of the detection capability of the proposed wearable antennas.

8.2.5 Development of a Modified Confocal Algorithm using Experimental Data

Typically, many research on radar based imaging systems for medical applications are conducted in frequency domain using a vector network analyser. To reconstruct an image of the body parts using a widely used confocal delay-and-sum algorithm, a conversion from the frequency domain to the time domain is required. This is mainly accomplished using inverse Fast Fourier Transform (IFFT). For monostatic approach where the same antenna acts as both the transmitter and the receiver, the time span of the signal after the conversion depends on the frequency step used during the measurement which could lead to uncertain time delay of the reconstructed pulse hence inaccurate estimation of a stroke or blood clot. To solve this issue, a new technique is proposed by utilising the magnitude of the reflected signal based on the variation of the collected S_{11} signal over the stroke's distance from the antenna. It is observed that the acquired S_{11} signal has higher difference in magnitude (compared to reference signal) across its operating frequency when the stroke location is closer to the antenna whereas deeper target produces low variation for the same target size. An interpolation technique is applied using this experimental data to estimate the location of the stroke. It is aimed that in the future, a database of this information taken from patients suffering from stroke or any other head injuries is established to assist the imaging algorithm.

8.3 Suggestions for Future Work

Although the conducted research has managed to successfully address several key problems and challenges involved in the implementation of a wearable head imaging system, there are other aspects that require further optimisations and improvements to further enhance its accuracy, efficiency and the practicality of the system. Some of the suggested work are summarized as follow:

8.3.1 Antenna Design

The future work on the antenna design is to increase the directivity of the antenna without the use of any external structure such as flexible dielectric absorber backed

with a reflector as suggested in this thesis. Several techniques can be explored such as the introduction of ground structure at the back of the antenna and the use of artificial magnetic conductor (AMC) that could increase its directionality. The challenge will be to maintain the flexible structure as proposed in this study in view of implementing wearable sensing antenna for head imaging systems. Another aspect that can be investigated is to use different materials for the construction of the antennas that can provide better flexibility and comfortability to the wearer such as PDMS and silicone gel. Additionally, the use of body coupled antenna may improve the sensitivity of the sensing antenna.

8.3.2 Antenna Array

In order to improve the accuracy and efficiency of the proposed wearable array, the number of antenna elements utilised in the array needs to be increased. One of the main issue with increasing the number of antennas is the space available considering that the antennas need to be positioned around the head which restricts the number of antennas that can be used. To mitigate this problem, the sensing antenna needs further miniaturisation without sacrificing its performance. In addition, future integration of the textile-based array with clothing is required.

8.3.3 RF Switching System

One of the novel aspect of this thesis is the integration of the antenna array with a compact RF switching circuit. The impedance matching of the fabricated integrated switching circuit can be improved particularly above 2.2GHz where the matching performance increases to -6dB compared to the initial prototype. The effects of bends on the RF transmission line require further investigations and solutions. Moreover, to improve the wearability of the proposed device, a flexible switching circuit can be designed and built using a flexible PCB technology. The next step also involves the integration of the wearable sensing device with a compact transceiver systems to replace the VNA used in this thesis where the overall system can be made fully wearable. This compact standalone transceiver will be the major challenge in realising a truly wearable system for real-time monitoring applications.

8.3.4 Imaging and Sensing Algorithms

One of the limitations of the confocal algorithm is that it cannot differentiate types of brain injuries such as to determine stroke types (ischemic or haemorrhage). This information is crucial to help doctors to provide the right treatment to patients. In addition, the proposed interpolation technique does not take into account the effect of various sizes of blood target towards the measured S_{11} signal. Hence, further optimisation on the algorithm must be done to consider both the distance and size of the blood clot. In addition, more advanced imaging techniques than the confocal algorithm are required. One of the techniques that could be implemented with the proposed wearable system is machine learning algorithms. However, intensive research, more experiments and clinical trials are needed to optimise the imaging and sensing aspects of the systems.

8.4 Final Comments

Wideband microwave imaging offers many advantages compared to the conventional methods of using MRI, ultrasound and CT scan such as low-cost, non-invasive and non-ionisation. Although the main aim of microwave imaging is not to replace these techniques, it is expected that this technology will be able to complement the existing imaging systems to provide more access for people that require an imaging tool for their medical check-up. Recently, radar-based head imaging system has gained a lot of attention from the research community due to its effectiveness in detecting brain diseases such as stroke, traumatic brain injuries and intracranial hematoma. However, there are very few research that have been conducted to implement the system for wearable applications. One of the main advantages of a flexible sensing device is that it is able to provide more comfort to the wearer which makes the patient more relax and comfortable when undergoing a test. Moreover, with the rapid progress in electronics, a wearable health monitoring systems are much needed in the progressing community. The realisation of wearable and wireless head monitoring systems will allow the monitoring of patients or personnel of intermediate risks at home or at work.

REFERENCE

- [1] S. C. Hagness, A. Taflove, and J. E. Bridges, “Two-Dimensional FDTD Analysis of a Pulsed Microwave Confocal System for Breast Cancer Detection: Fixed-Focus and Antenna-Array Sensors,” *IEEE Trans. Antennas Propag.*, vol. 47, no. 12, pp. 783–791, 1999.
- [2] E. C. Fear and M. A. Stuchly, “Microwave System for Breast Tumor Detection,” *IEEE Microw. Guid. Wave Lett.*, vol. 9, no. 11, pp. 470–472, 1999.
- [3] E. C. Fear, J. Sill, and M. A. Stuchly, “Experimental feasibility study of confocal microwave imaging for breast tumor detection,” *IEEE Trans. Microw. Theory Tech.*, vol. 51, no. 3, pp. 887–892, 2003.
- [4] E. Porter, S. Member, E. Kirshin, S. Member, A. Santorelli, S. Member, M. Coates, and S. Member, “Time-Domain Multistatic Radar System for Microwave Breast Screening,” vol. 12, pp. 229–232, 2013.
- [5] A. W. Preece, I. Craddock, M. Shere, L. Jones, and H. L. Winton, “MARIA M4: clinical evaluation of a prototype ultrawideband radar scanner for breast cancer detection,” *J. Med. Imaging*, vol. 3, no. 3, p. 33502, 2016.
- [6] S. Y. Semenov and D. R. Corfield, “Microwave Tomography for Brain Imaging: Feasibility Assessment for Stroke Detection,” *Int. J. Antennas Propag.*, pp. 1–8, 2008.
- [7] S. Semenov, B. Seiser, E. Stoegmann, E. Auff, and E. Gmbh, “Electromagnetic Tomography for Brain Imaging: from virtual to human brain,” in *IEEE Conference on Antenna Measurements & Applications (CAMA)*, 2014, pp. 1–4.
- [8] S. Semenov, R. Planas, M. Hopfer, A. Hamidipour, A. Vasilenko, E. Stoegmann, and E. Auff, “Electromagnetic tomography for brain imaging: Initial assessment for stroke detection,” *2015 IEEE Biomed. Circuits Syst. Conf.*, pp. 1–4, 2015.
- [9] M. Persson, A. Fhager, H. Dobsicek Trefna, Y. Yu, T. Mckelvey, G. Pegenius, J.-E. Karlsson, and M. Elam, “Microwave-based stroke diagnosis making global prehospital thrombolytic treatment possible,” *IEEE Trans. Biomed. Eng.*,

- vol. 61, no. 11, pp. 2806–2817, 2014.
- [10] M. Jalilvand, T. Zwick, W. Wiesbeck, and E. Pancera, “UWB synthetic aperture-based radar system for hemorrhagic head-stroke detection,” *2011 IEEE RadarCon*, pp. 956–959, 2011.
 - [11] B. J. Mohammed, A. M. Abbosh, S. Mustafa, and D. Ireland, “Microwave system for head imaging,” *IEEE Trans. Instrum. Meas.*, vol. 63, no. 1, pp. 117–123, 2014.
 - [12] A. T. Mobashsher and A. M. Abbosh, “On-site Rapid Diagnosis of Intracranial Hematoma using Portable Multi-slice Microwave Imaging System,” *Sci. Rep.*, vol. 6, no. 1, p. 37620, 2016.
 - [13] S. Salman, Z. Wang, E. Colebeck, A. Kiourti, E. Topsakal, and J. L. Volakis, “Pulmonary edema monitoring sensor with integrated body-area network for remote medical sensing,” *IEEE Trans. Antennas Propag.*, vol. 62, no. 5, pp. 2787–2794, 2014.
 - [14] B. Allen, M. Dohler, E. Okon, and W. Malik, *Ultra-wideband Antennas and Propagation for Communications, Radar and Imaging*. John Wiley & Sons, Inc., 2006.
 - [15] A. T. Mobashsher and A. M. Abbosh, “Compact 3-D Slot-Loaded Folded Dipole Antenna with Unidirectional Radiation and Low Impulse Distortion for Head Imaging Applications,” *IEEE Trans. Antennas Propag.*, vol. 64, no. 7, pp. 3245–3250, 2016.
 - [16] H. Bahramiabarghouei, E. Porter, B. Gosselin, M. Popovi, and L. A. Rusch, “Flexible 16 antenna array for microwave breast cancer detection,” *IEEE Trans. Biomed. Eng.*, vol. 62, no. 10, pp. 2516–2525, 2015.
 - [17] R. Yahya, M. R. Kamarudin, and N. Seman, “New Wideband Textile Antenna for SAR Investigation in Head Microwave Imaging,” in *RF and Wireless Technologies for Biomedical and Healthcare Applications (IMWS-Bio)*, 2014, pp. 1–3.
 - [18] K. P. Ray, “Design Aspects of Printed Monopole Antennas for Ultra-Wide Band Applications,” *Int. J. Antennas Propag.*, pp. 1–8, 2008.

- [19] “Atmel 8-BIT Microcontroller with 4/8/16/32Kbytes in-System Programmable Flash, ATmega48A/PA/88A/PA/168A/PA/328/P.” [Online]. Available: <https://www.farnell.com/datasheets/1693866.pdf>. [Accessed: 30-Dec-2016].
- [20] “GaAs MMIC SP4T non-reflective positive control switch.” [Online]. Available: <http://www.analog.com/media/en/technical-documentation/datasheets/hmc241alp3e.pdf>.
- [21] “GaAs MMIC SP8T Non-reflective positive control switch.” [Online]. Available: <http://www.analog.com/media/en/technical-documentation/datasheets/hmc321.pdf>.
- [22] “FT232R USB UART IC Datasheet.” [Online]. Available: http://www.ftdichip.com/Support/Documents/DataSheets/ICs/DS_FT232R.pdf. [Accessed: 30-Dec-2017].
- [23] “HC-06 Bluetooth Module.” [Online]. Available: www.wavesen.com. [Accessed: 30-Dec-2017].
- [24] C. Susskind, “Possible Use of Microwaves in the Management of Lung Disease,” in *Proceedings of the IEEE*, 1967, pp. 673–674.
- [25] P. C. Pedersen, C. C. Johnson, C. H. Durney, and D. G. Bragg, “Microwave Reflection and Transmission Measurements for Pulmonary Diagnosis and Monitoring,” *IEEE Trans. Biomed. Eng.*, vol. BME-25, no. 1, pp. 40–48, 1978.
- [26] E. C. Fear, X. Li, S. C. Hagness, and M. A. Stuchly, “Confocal microwave imaging for breast cancer detection: Localization of tumors in three dimensions,” *IEEE Trans. Biomed. Eng.*, vol. 49, no. 8, pp. 812–822, 2002.
- [27] J. M. Sill and E. C. Fear, “Tissue sensing adaptive radar for breast cancer detection-experimental investigation of simple tumor models,” *IEEE Trans. Microw. Theory Tech.*, vol. 53, no. 11, pp. 3312–3319, 2005.
- [28] A. T. Mobashsher, A. M. Abbosh, and Y. Wang, “Microwave System to Detect Traumatic Brain Injuries Using Compact Unidirectional Antenna and Wideband Transceiver with Verification on Realistic Head Phantom,” *IEEE Trans. Microw. Theory Tech.*, vol. 62, no. 9, pp. 1826–1836, 2014.
- [29] S. Candefjord, J. Winges, A. A. Malik, Y. Yu, T. Rylander, T. McKelvey, A.

- Fhager, M. Elam, and M. Persson, "Microwave Technology for Detecting Traumatic Intracranial Bleedings: Tests on Phantom of Subdural Hematoma and Numerical Simulations," *Med. Biol. Eng. Comput.*, pp. 1–12, 2016.
- [30] J. C. Ljungqvist, S. Candefjord, M. Persson, L. Jönsson, T. S. Skoglund, and M. Elam, "Clinical Evaluation of a Microwave-Based Device for Detection of Traumatic Intracranial Hemorrhage," *J. Neurotrauma*, vol. 7, p. neu.2016.4869, 2017.
- [31] S. A. Rezaeieh, A. Zamani, K. S. Bialkowski, and A. M. Abbosh, "Foam Embedded Wideband Antenna Array for Early Congestive Heart Failure Detection with Tests Using Artificial Phantom with Animal Organs," *IEEE Trans. Antennas Propag.*, vol. 63, no. 11, pp. 5138–5143, 2015.
- [32] S. Ahdi Rezaeieh, A. Zamani, and A. M. Abbosh, "Three Dimensional Wideband Antenna for Head Imaging System with Performance Verification in Brain Tumor Detection," *IEEE Antennas Wirel. Propag. Lett.*, vol. 14, pp. 910–914, 2015.
- [33] S. Ahdi Rezaeieh, A. Zamani, K. S. Bialkowski, and A. M. Abbosh, "Novel Microwave Torso Scanner for Thoracic Fluid Accumulation Diagnosis and Monitoring," *Sci. Rep.*, vol. 7, no. 1, p. 304, 2017.
- [34] J. L. Schepps and K. R. Foster, "The UHF and Microwave Dielectric Properties of Normal and Tumour Tissues: Variation in Dielectric Properties with Tissue Water Content," *Phys. Med. Biol.*, vol. 25, no. 6, p. 1149, 1980.
- [35] D. S. Yoo, "The Dielectric Properties of Cancerous Tissues in a Nude Mouse Xenograft Model," *Bioelectromagnetics*, vol. 25, no. April 2003, pp. 492–497, 2004.
- [36] "State of the nation," 2017. [Online]. Available: https://www.stroke.org.uk/sites/default/files/state_of_the_nation_2017_final_1.pdf. [Accessed: 26-Dec-2017].
- [37] D. Ireland and M. Bialkowski, "Feasibility Study on Microwave Stroke Detection using a Realistic Phantom and the FDTD Method," in *Microwave Conference Proceedings (APMC), 2010 Asia-Pacific*, 2010, pp. 1360–1363.

- [38] D. Ireland and M. E. Bialkowski, "Microwave Head Imaging for Stroke Detection," *Prog. Electromagn. Res. M*, vol. 21, pp. 163–175, 2011.
- [39] Qing Huo Liu, Zhong Qing Zhang, T. T. Wang, J. A. Bryan, G. A. Ybarra, L. W. Nolte, and W. T. Joines, "Active microwave imaging. I. 2-D forward and inverse scattering methods," *IEEE Trans. Microw. Theory Tech.*, vol. 50, no. 1, pp. 123–133, 2002.
- [40] A. Fhager and M. Persson, "A Microwave Measurement System for Stroke Detection," *Loughbrgh. Antennas Propag. Conf.*, no. November, pp. 14–15, 2011.
- [41] B. J. Mohammed, A. M. Abbosh, and D. Ireland, "Stroke Detection Based on Variations in Reflection Coefficients of Wideband Antennas," in *IEEE Antennas and Propagation Society International Symposium (APSURSI)*, 2012, pp. 1–2.
- [42] A. T. Mobashsher, B. J. Mohammed, S. Mustafa, and A. Abbosh, "Ultra Wideband Antenna for Portable Brain Stroke Diagnostic System," in *IEEE MTT-S International Microwave Workshop Series on RF and Wireless Technologies for Biomedical and Healthcare Applications, IMWS-BIO 2013 - Proceedings*, 2013, pp. 2–4.
- [43] A. T. Mobashsher and A. M. Abbosh, "On-site Rapid Diagnosis of Intracranial Hematoma using Portable Multi-slice Microwave Imaging System," *Sci. Rep.*, vol. 6, no. 1, p. 37620, 2016.
- [44] R. Paradiso, G. Loriga, and N. Taccini, "A Wearable Health Care System Based on Knitted Integrated Sensors," *IEEE Trans. Inf. Technol. Biomed.*, vol. 9, no. 3, pp. 337–344, 2005.
- [45] C. Gabriel, "Compilation of the Dielectric Properties of Body Tissues at RF and Microwave Frequencies," *Armstrong Lab. Brooks Air Force Base, Tech. Rep.*, no. AL/OE-TR-1996–0037, 1996.
- [46] M. Klemm, J. A. Leendertz, D. Gibbins, I. J. Craddock, A. Preece, and R. Benjamin, "Microwave Radar-Based Differential Breast Cancer Imaging: Imaging in Homogeneous Breast phantoms and Low Contrast Scenarios," *IEEE Trans. Antennas Propag.*, vol. 58, no. 7, pp. 2337–2344, 2010.

- [47] S. C. Hagness, A. Taflove, and J. E. Bridges, "Three-Dimensional FDTD Analysis of a Pulsed Microwave Confocal System for Breast Cancer Detection: Design of an Antenna-Array Element," *IEEE Trans. Antennas Propag.*, vol. 47, no. 5, pp. 783–791, 1999.
- [48] S. S. Chaudhary, R. K. Mishra, A. Swarup, and J. M. Thomas, "Dielectric Properties of Normal and Malignant Human Breast Tissues at Radiowave and Microwave Frequencies," *Indian J. Biochem. Biophys.*, vol. 21, pp. 76–79, 1984.
- [49] E. Porter, A. Santorelli, S. Winkler, M. Coates, and M. Popovic, "Time-Domain Microwave Cancer Screening: Optimized Pulse Shaping Applied to Realistically Shaped Breast Phantoms," *IEEE MTT-S Int. Microw. Symp. Dig.*, pp. 4–6, 2012.
- [50] E. Porter, A. Santorelli, M. Coates, and M. Popovic, "An Experimental System for Time-Domain Microwave Breast Imaging," *Proc. 5th Eur. Conf. Antennas Propag.*, pp. 2906–2910, 2011.
- [51] D. Gibbins, M. Klemm, I. J. Craddock, J. A. Leendertz, A. Preece, and R. Benjamin, "A Comparison of a Wide-Slot and a Stacked Patch Antenna for the Purpose of Breast Cancer Detection," *IEEE Trans. Antennas Propag.*, vol. 58, no. 3, pp. 665–674, 2010.
- [52] D. Gibbins, M. Klemm, I. Craddock, A. Preece, J. Leendertz, and R. Benjamin, "Design of a UWB Wide-Slot Antenna and a Hemispherical Array for Breast Imaging," *2009 3rd Eur. Conf. Antennas Propag.*, pp. 2967–2970, 2009.
- [53] M. Klemm, I. J. Craddock, J. A. Leendertz, A. Preece, and R. Benjamin, "Radar-Based Breast Cancer Detection using a Hemispherical Antenna Array — Experimental Results," *IEEE Trans. Antennas Propag.*, vol. 57, no. 6, pp. 1692–1704, 2009.
- [54] R. Nilavalan, A. Gbedemah, I. J. Craddock, X. Li, and S. C. Hagness, "Numerical Investigation of Breast Tumour Detection using Multi-Static Radar," *Electron. Lett.*, vol. 39, no. 25, pp. 1787–1789, 2008.
- [55] M. Klemm, I. J. Craddock, J. A. Leendertz, A. Preece, and R. Benjamin, "Improved Delay-and-Sum Beamforming Algorithm for Breast Cancer

- Detection,” *Int. J. Antennas Propag.*, vol. 2008, pp. 1–9, 2008.
- [56] M. E. Bialkowski, “Ultra Wideband Microwave System with Novel Image Reconstruction Strategies for Breast Cancer Detection,” *Proc. 40th Eur. Microw. Conf.*, no. September, pp. 537–540, 2010.
- [57] S. M. Salvador and G. Vecchi, “Experimental tests of microwave breast cancer detection on phantoms,” *IEEE Trans. Antennas Propag.*, vol. 57, no. 6, pp. 1705–1712, 2009.
- [58] H. Kanj and M. Popovic, “a Novel Ultra-Compact Broadband Antenna for Microwave Breast Tumor Detection,” *Prog. Electromagn. Res.*, vol. 86, pp. 169–198, 2008.
- [59] M. Bassi, M. Caruso, M. S. Khan, A. Bevilacqua, A. D. Capobianco, and A. Neviani, “An Integrated Microwave Imaging Radar with Planar Antennas for Breast Cancer Detection,” *IEEE Trans. Microw. Theory Tech.*, vol. 61, no. 5, pp. 2108–2118, 2013.
- [60] H. Zhang, T. Arslan, and B. Flynn, “A Single Antenna Based Microwave System for Breast Cancer Detection: Experimental Results,” *2013 Loughbrgh. Antennas Propag. Conf. LAPC 2013*, no. November, pp. 477–481, 2013.
- [61] H. B. Lim, N. Thi, T. Nhung, E. Li, and N. D. Thang, “Confocal Microwave Imaging for Breast Cancer Detection : Delay-Multiply-and-Sum Image,” *IEEE Trans. Biomed. Eng.*, vol. 55, no. 6, pp. 1697–1704, 2008.
- [62] B. Smith and M. H. Carpentier, *The Microwave Engineering Handbook*. Chapman & Hall, 1993.
- [63] A. G. Lalkhen and A. McCluskey, “Clinical tests: Sensitivity and specificity,” *Contin. Educ. Anaesthesia, Crit. Care Pain*, vol. 8, no. 6, pp. 221–223, 2008.
- [64] H. Zhang, B. Flynn, A. T. Erdogan, and T. Arslan, “Microwave Imaging for Brain Tumour Detection using an UWB Vivaldi Antenna Array,” in *Loughborough Antennas & Propagation Conference*, 2012, pp. 1–4.
- [65] A. Abbosh and A. T. Mobashsher, “Development of Compact Directional Antenna utilising Plane of Symmetry for Wideband Brain Stroke Detection Systems,” *Electron. Lett.*, vol. 50, no. 12, pp. 850–851, 2014.

- [66] A. T. Mobashsher, S. Member, A. M. Abbosh, and S. Member, "Three-Dimensional Human Head Phantom With Realistic Electrical Properties and Anatomy," *IEEE Trans. Antennas Propag. Lett.*, vol. 13, pp. 1401–1404, 2014.
- [67] Y. L. Zheng, X. R. Ding, C. C. Y. Poon, B. P. L. Lo, H. Zhang, X. L. Zhou, G. Z. Yang, N. Zhao, and Y. T. Zhang, "Unobtrusive Sensing and Wearable Devices for Health Informatics," *IEEE Trans. Biomed. Eng.*, vol. 61, no. 5, pp. 1538–1554, 2014.
- [68] A. Kiourti and J. L. Volakis, "Wearable Antennas using Electronic Textiles for RF Communications and Medical Monitoring," in *2016 10th European Conference on Antennas and Propagation, EuCAP 2016*, 2016, pp. 1–2.
- [69] P. J. Soh, G. A. E. VVandenbosch, M. Mercuri, and D. M. M.-P. Schreurs, "Wearable Wireless Health Monitoring," *IEEE Microw. Mag.*, vol. 16, no. 4, pp. 55–70, 2015.
- [70] J. M. Fontana, M. Farooq, and E. Sazonov, "Automatic Ingestion Monitor: A Novel Wearable Device for Monitoring of Ingestive Behavior," *IEEE Trans. Biomed. Eng.*, vol. 61, no. 6, pp. 1772–1779, 2014.
- [71] S. Kim, "Design of Infant Health Condition Check Solution based on a Wearable Device with Attitude Heading Reference System," in *8th International Conference on Bio-Science and Bio-Technology Design*, 2015, pp. 1–3.
- [72] A. Cyrous, B. O'Neal, and W. D. Freeman, "New Approaches to Bedside Monitoring in Stroke," *Expert Rev. Neurother.*, vol. 12, no. 8, pp. 915–928, Aug. 2012.
- [73] N. H. M. Rais, P. J. Soh, F. Malek, S. Ahmad, N. B. M. Hashim, and P. S. Hall, "A Review of Wearable Antenna," in *Loughborough Antennas and Propagation Conference (LAPC)*, 2009, no. 12, pp. 225–228.
- [74] P. J. Soh, G. A. E. Vandenbosch, S. L. Ooi, and N. H. M. Rais, "Design of a Broadband All-Textile Slotted PIFA," *IEEE Trans. Antennas Propag.*, vol. 60, no. 1, pp. 379–384, 2012.
- [75] P. J. Soh, B. Van Den Bergh, H. Xu, H. Aliakbarian, S. Farsi, P. Samal, G. A.

- E. Vandenbosch, D. M. M. P. Schreurs, and B. K. J. C. Nauwelaers, "A Smart Wearable Textile Array System for Biomedical Telemetry Applications," *IEEE Trans. Microw. Theory Tech.*, vol. 61, no. 5, pp. 2253–2261, 2013.
- [76] M. N. Ramli, P. J. Soh, H. A. Rahim, M. F. Jamlos, and F. N. Giman, "SAR for Wearable Antennas with AMC Made using PDMS and Textiles 2 . Materials and Antenna Design," in *32nd International Union of Radio Science General Assemble & Scientific Symposium*, 2017, pp. 1–3.
- [77] P. B. Samal, P. J. Soh, and G. A. E. Vandenbosch, "UWB All-Textile Antenna with Full Ground Plane for Off-Body WBAN Communications," *IEEE Trans. Antennas Propag.*, vol. 62, no. 1, pp. 102–108, 2014.
- [78] G. A. Casula, G. Montisci, and G. Mazzarella, "A Wideband PET Inkjet-Printed Antenna for UHF RFID," *IEEE Antennas Wirel. Propag. Lett.*, vol. 12, pp. 1400–1403, 2013.
- [79] S. Ahmed, F. A. Tahir, A. Shamim, and H. M. Cheema, "A Compact Kapton-Based Inkjet-Printed Multiband Antenna for Flexible Wireless Devices," *IEEE Antennas Wirel. Propag. Lett.*, vol. 14, pp. 1802–1805, 2015.
- [80] R. Yahya, M. R. Kamarudin, and N. Seman, "Wideband Antenna for Microwave Imaging," in *Progress In Electromagnetics Research Symposium Proceedings*, 2014, pp. 1983–1985.
- [81] M. Koohestani, M. N. Moghadasi, and B. S. Virdee, "Miniature Microstrip-Fed Ultra-Wideband Printed Monopole Antenna with a Partial Ground Plane Structure," *IET Microwaves, Antennas Propag.*, vol. 5, no. 14, p. 1683, 2011.
- [82] A. Rahman and Y. Hao, "A Novel Tapered Slot CPW-fed Antenna for Ultra-Wideband Applications and its On/Off-Body Performance," in *IEEE International Workshop on Antenna Technology: Small and Smart Antennas Metamaterials and Applications, iWAT 2007*, 2007, pp. 503–506.
- [83] S. W. Su, K. L. Wong, and C. L. Tang, "Ultra-Wideband Square Planar Monopole Antenna for IEEE 802.16a Operation in the 2-11-GHz Band," *Microw. Opt. Technol. Lett.*, vol. 42, no. 6, pp. 463–466, 2004.
- [84] A.-C. Tarot, F. Las-Heras, M. Mantash, and M. E. de Cos, "Dual-Band Coplanar

- Waveguide-Fed Smiling Monopole Antenna for WiFi and 4G Long-Term Evolution Applications,” *IET Microwaves, Antennas Propag.*, vol. 7, no. 9, pp. 777–782, 2013.
- [85] M. Tømmer and K. G. Kjelg, “Body Coupled Wideband Monopole Antenna,” in *Loughborough Antennas & Propagation Conference (LAPC)*, 2016, pp. 1–5.
- [86] A. Rahman, M. T. Islam, M. J. Singh, S. Kibria, and M. Akhtaruzzaman, “Electromagnetic Performances Analysis of an Ultra-wideband and Flexible Material Antenna in Microwave Breast Imaging: To Implement A Wearable Medical Bra,” *Sci. Rep.*, vol. 6, no. 1, p. 38906, 2016.
- [87] G. Ghione and C. Naldi, “Analytical Formulas for Coplanar Lines in Hybrid and Monolithic MICs,” *Electron. Lett.*, vol. 20, no. 4, p. 179, 1984.
- [88] G. S. Reddy, S. Kharche, and J. Mukherjee, “Ultra Wideband Printed Monopole Antenna with Curve Shaped Extended Asymmetric CPW Ground Plane for Stable Unidirectional Radiation Pattern,” *IEEE Antennas Propag. Soc. AP-S Int. Symp.*, pp. 1823–1824, 2014.
- [89] J. Liu, S. Zhong, and K. P. Esselle, “A Printed Elliptical Monopole Antenna with Modified Feeding Structure for Bandwidth Enhancement,” *IEEE Trans. Antennas Propag.*, vol. 59, no. 2, pp. 667–670, 2011.
- [90] G. Pan, Y. Li, Z. Zhang, and Z. Feng, “A Compact Wideband Slot-Loop Hybrid Antenna with a Monopole Feed,” *IEEE Trans. Antennas Propag.*, vol. 62, no. 7, pp. 3864–3868, 2014.
- [91] W. L. Stutzman and G. A. Thiele, *Antenna Theory and Design*, 3rd ed. NJ: John Wiley & Sons, Inc., 2013.
- [92] T. M. Nguyen and J. Chung, “RF Conductivity Measurement of Conductive Zell Fabric,” *J. Electromagn. Eng. Sci.*, vol. 16, no. 1, pp. 24–28, 2016.
- [93] E. Porter, H. Bahrami, A. Santorelli, B. Gosselin, L. A. Rusch, and M. Popovic, “A Wearable Microwave Antenna Array for Time-Domain Breast Tumor Screening,” *IEEE Trans. Med. Imaging*, vol. 35, no. 6, pp. 1501–1509, 2016.
- [94] A. T. Mobashsher, “Wideband Microwave Imaging System for Brain Injury Diagnosis,” The University of Queensland, Queensland, Australia, 2016.

- [95] N. Rahman, A. Sharma, M. Afsar, S. Palreddy, and R. Cheung, "Design and Analysis of An Optimized Cavity-Backed Zigzag Archimedean Spiral Antenna," in *4th European Conference on Antennas and Propagation (EuCAP)*, 2010, pp. 1–4.
- [96] H. Bahrami, S. A. Mirbozorgi, R. Ameli, L. A. Rusch, and B. Gosselin, "Flexible, Polarization-Diverse UWB Antennas for Implantable Neural Recording Systems," *IEEE Trans. Biomed. Circuits Syst.*, vol. 10, no. 1, pp. 38–48, 2016.
- [97] A. Danideh and R. A. Sadeghzadeh, "A Planar Ultrawideband Elliptical Monopole Antenna with Reflector for Breast Microwave Imaging," *Microw. Opt. Technol. Lett.*, vol. 6, no. 1, pp. 3872–3875, 2013.
- [98] "Increasing Directivity in Parabolic Antennas." [Online]. Available: http://www.eccosorb.eu/sites/default/files/files/increasing_directivity_in_parabolic_antennas.pdf. [Accessed: 02-Feb-2018].
- [99] Eccosorb, "ECCOSORB® AN - Emerson & Cuming Microwave Products." [Online]. Available: <http://www.eccosorb.com/products-eccosorb-an.htm>.
- [100] W. Zhou and T. Arslan, "A Bidirectional Planar Monopole Antenna Array for WiFi / Bluetooth and LTE Mobile Applications," in *Loughborough Antennas & Propagation Conference (LAPC)*, 2013, vol. 1, no. November, pp. 190–193.
- [101] N. H. Noordin, V. Zuniga, A. O. El-Rayis, N. Haridas, A. T. Erdogan, and T. Arslan, "Uniform Circular Arrays for Phased ArrayAntenna," in *LAPC 2011 - 2011 Loughborough Antennas and Propagation Conference*, 2011, no. November, pp. 1–4.
- [102] J. C. Lin, "A New IEEE Standard For Safety Levels with respect to Human Exposure to Radio-Frequency Radiation," *IEEE Antennas Propag. Mag.*, vol. 48, no. 1, pp. 157–159, 2006.
- [103] B. Rajagopal and L. Rajasekaran, "SAR Assessment on Three Layered Spherical Human Head Model Irradiated by Mobile Phone Antenna," pp. 1–11, 2014.

- [104] P. Bernardi, M. Cavagnaro, and S. Pisa, "Evaluation of the SAR distribution in the human head for cellular phones used in a partially closed environment," *IEEE Trans. Electromagn. Compat.*, vol. 38, no. 3, pp. 357–366, 1996.
- [105] S. Khalatbari, D. Sardari, A. A. Mirzaee, and H. A. Sadafi, "Calculating SAR in two Models of the Human Head Exposed to Mobile Phones Radiations at 900 and 1800 MHz," *PIERS Online*, vol. 2, no. 1, pp. 104–109, 2006.
- [106] Y.-H. Hao, L. Zhao, and R.-Y. Peng, "Effects of microwave radiation on brain energy metabolism and related mechanisms," *Mil. Med. Res.*, vol. 2, no. 1, p. 4, 2015.
- [107] R. Varghese, A. Majumdar, G. Kumar, and A. Shukla, "Rats exposed to 2.45 GHz of non-ionizing radiation exhibit behavioral changes with increased brain expression of apoptotic caspase 3," *Pathophysiology*, vol. 25, no. 1, pp. 19–30, 2018.
- [108] S. Hussein, A. A. El-Saba, and M. K. Galal, "Biochemical and histological studies on adverse effects of mobile phone radiation on rat's brain," *J. Chem. Neuroanat.*, vol. 78, pp. 10–19, 2016.
- [109] P. a Valberg, "Ratio Frequency Radiation (RFR):the Nature of Exposure and Carcinogenic Potential," *Cancer Causes Control*, vol. 8, pp. 323–332, 1997.
- [110] "PCB Manufacturer - Multi Circuit Boards." [Online]. Available: <https://www.multi-circuit-boards.eu/en/index.html>. [Accessed: 21-Feb-2018].
- [111] Y. Hong, J. Tak, J. Baek, B. Myeong, and J. Choi, "Design of a Multiband Antenna for LTE/GSM/UMTS band Operation," *Int. J. Antennas Propag.*, 2014.
- [112] A. Peyman, S. Holden, and C. Gabriel, "Dielectric properties of tissues at microwave frequencies," 2000.
- [113] L. Di Donato, "A feasibility Study on Microwave Imaging for Brain Stroke Monitoring," *Prog. Electromagn. Res. B*, vol. 40, no. February, pp. 305–324, 2012.
- [114] R. Scapaticci, O. M. Bucci, and L. Crocco, "Robust microwave imaging for brain stroke monitoring," in *Engineering Science and Technology, an*

International Journal, 2013, pp. 75–78.

- [115] E. Bilgin, A. Aygun, A. Yapar, and I. Akduman, “Analysis of Matching Media Effect on Microwave Brain Stroke Imaging via a Spherically Symmetrical Head Model,” in *Progress in Electromagnetics Research Symposium*, 2015, pp. 452–456.
- [116] J. Broderick, T. Brott, J. Duldner, T. Tomsick, and G. Huster, “Volume of Intracerebral Hemorrhage A Powerful and Easy-to-Use Predictor of 30-Day Mortality,” *Stroke.*, vol. 24, no. 7, pp. 987–93, 1993.
- [117] B. Mohammed, A. Abbosh, B. Henin, and P. Sharpe, “Head Phantom for Testing Microwave Systems for Head Imaging,” in *Cairo International Biomedical Engineering Conference (CIBEC)*, 2012, pp. 191–193.
- [118] J. Lee, J. Bang, and J. Choi, “Realistic Head Phantom for Evaluation of Brain Stroke Localization Methods Using 3D Printer,” *J. Electromagn. Eng. Sci.*, vol. 16, no. 4, pp. 254–258, 2016.
- [119] L. Guo, “Processing and Imaging Techniques for Microwave-Based Head Imaging,” The University of Queensland, 2016.
- [120] S. Mustafa, B. Mohammed, and A. Abbosh, “Novel Preprocessing Techniques for Accurate Microwave Imaging of Human Brain,” *IEEE Antennas Wirel. Propag. Lett.*, vol. 12, pp. 460–463, 2013.
- [121] R. U. Kothari, T. Brott, J. P. Broderick, W. G. Barsan, L. R. Sauerbeck, M. Zuccarello, and J. Khoury, “The ABCs of Measuring Intracerebral Hemorrhage Volumes,” *Stroke*, vol. 27, no. 8, p. 1304 LP-1305, Aug. 1996.
- [122] B. J. Mohammed, K. S. Bialkowski, and A. M. Abbosh, “Radar-based time-domain head imaging using database of effective dielectric constant,” *Electron. Lett.*, vol. 51, no. 20, pp. 1574–1576, 2015.
- [123] J. Ljungqvist, “Diagnostic Methods in Traumatic Brain Injury,” University of Gothenburgh, 2017.